UNIVERSITY SAAD DAHLAB OF BLIDA 1

Faculty of Technology

Department of Electro-technic & automatic

DOCTORAL THESIS (LMD)

In Automatic

Specialization: Automatics

Application of Metaheuristic-Based Approach for the Diagnosis of Electrical Machines

By

Amat Ellah Noussaiba LAZAR

In front of the jury composed of:

Kamel KARA	Professor., U. Blida1	President
Abdelaziz FERDJOUNI	Professor., U. Blida1	Thesis Supervisor
Hamoud SAARI	Professor., National Higher Maritime School Bousmail	Examiner
Alghalia BOUDISSA	M.C.A., U. Blida1	Examiner
Khadidja ELMERRAOUI	M.C.B., U. BLIDA1	A guest

Blida, juily 2024

Abstract

Fault diagnosis is critical in control theory for improving safety, performance, and reliability in controlled processes. Detecting system errors, component faults, and abnormal operations promptly is essential for diagnosing the source and severity of malfunctions. Various solutions have been proposed for fault diagnosis and residual generation. The widely used squirrel cage three-phase induction motor in industrial applications demands reliable operation due to its robustness, low cost, and standardization. Induction motor failures, particularly inter-turn short circuits in stator windings, can lead to significant downtimes and adverse effects on both people and installations. Additionally, unbalanced supply voltage, which is a common and significant phenomenon, may hinder our ability to differentiate it from the detection of inter-turn short circuits.

In this thesis, we have contributed to the field by presenting a comprehensive solution for the detection, classification, and severity estimation of faults in induction machines using artificial intelligence tools. My work includes developing a mathematical model that incorporates Stator Inter Turn Short-Circuit faults across three phases of an induction motor. I implemented a Feed Forward Neural Network (FFNN) approach for fault detection and phase-specific classification, followed by a Multi-Layer Perceptron (MLP) Neural Network approach for detecting and classifying both Stator Inter Turn Short-Circuit and Unbalanced Supply Voltage faults, as well as estimating the severity of short-circuits. I explored various types of Artificial Neural Networks (ANNs) to improve fault detection, classification accuracy, and severity estimation. My thesis is organized into four chapters: an introduction covering induction motor faults and diagnostic techniques, development and validation of induction motor models using MATLAB/Simulink, implementation of FFNN and MLP processes for fault detection and severity estimation, and a comprehensive Fault Identification process utilizing multiple ANNs in a cascaded manner. My skills include mathematical modeling, MATLAB/Simulink proficiency, and expertise in Neural Network development for fault diagnosis and optimization in industrial applications

ملخص

تشخيص الأعطال أمر حيوي في نظرية التحكم لتحسين السلامة والأداء والموثوقية في العمليات المُسيطر عليها. إن اكتشاف أخطاء النظام وعيوب المكونات والعمليات الغير طبيعية بسرعة أمر أساسي لتشخيص مصدر وشدة الأعطال. تم اقتراح حلول متنوعة لتشخيص الأعطال وتوليد المتبقيات. المحرك الحثي ذو الثلاث مراحل بحوية قفص السنجاب المستخدم على نطاق واسع في التطبيقات الصناعية يتطلب عملية موثوقة بسبب قوته وتكلفته المنخفضة وتوحيد تصنيعه. فشل محرك الحث، خصوصاً الدوائر القصيرة بين التفافات الجزء الثابت، قد يؤدي إلى فترات توقف طويلة وتأثيرات سلبية على الأشخاص والتركيبات. بالإضافة إلى ذلك، الجهد المتغير للتغذية الكهربائية غير المتوازن، الذي هو ظاهرة شائعة ومهمة، قد يعيق قدرتنا على التمييز بينه وبين اكتشاف الدوائر القصيرة بين التفافات.

في هذه الاطروحة، قدمنا مساهمة في المجال من خلال تقديم حلاً شاملاً للكشف والتصنيف وتقدير شدة الأخطاء في آلات التوليد بالحث باستخدام أدوات الذكاء الاصطناعي. يتضمن عملي تطوير نموذج رياضي يدمج أخطاء القصر بين اللفات في المحركات للكشف عن الأخطاء والتصنيف (FFNN) الحثية عبر ثلاث مراحل من محرك الحث. نفذت نهج شبكة عصبونية تغذية إلى الأمام لكشف وتصنيف كل من أخطاء القصر بين (MLP) الخاص بكل مرحلة، تليها نهج شبكة عصبونية بالمعرفة المتعددة الطبقات اللفات في الستاتور وأخطاء توازن الجهد التوريد غير المتوازن، بالإضافة إلى تقدير شدة القصر. استكشفت أنواع مختلفة من لتحسين كشف الأخطاء ودقة التصنيف وتقدير الشدة. تنظم رسالتي إلى أربعة فصول: (ANNs) الشبكات العصبية الاصطناعية MATLAB / مقدمة تغطي أخطاء المحركات الحثية وتقنيات التشخيص، وتطوير وتحقق نماذج المحركات الحثية باستخدام لكشف الأخطاء وتقدير الشدة، وعملية شاملة لتحديد الأخطاء باستخدام العديد من MLP و FFNN ، وتنفيذ عملياتSimulink والخبرة في تطوير شبكات الأعصاب MATLAB / Simulink بطريقة متتالية. تشمل مهاراتي النمذجة الرياضية وإتقان ANNs لتشخيص الأخطاء والتحسين في التطبيقات الصناعية.

Résumé

Le diagnostic de défaut est crucial en théorie de contrôle pour améliorer la sécurité, les performances et la fiabilité des processus contrôlés. Détecter rapidement les erreurs système, les défauts de composants et les opérations anormales est essentiel pour diagnostiquer l'origine et la gravité des dysfonctionnements. Diverses solutions ont été proposées pour le diagnostic de défaut et la génération de résidus. Le moteur à induction triphasé à cage d'écureuil largement utilisé dans les applications industrielles exige un fonctionnement fiable en raison de sa robustesse, de son faible coût et de sa standardisation. Les défaillances des moteurs à induction, en particulier les court-circuites inter-spires dans les enroulements de stator, peuvent entraîner des temps d'arrêt importants et des effets néfastes sur les personnes et les installations. De plus, la tension d'alimentation déséquilibrée, phénomène courant et significatif, peut entraver notre capacité à la différencier de la détection de court-circuit inter-spires.

Dans cette thèse, nous avons contribué au domaine en présentant une solution complète pour la détection, la classification et l'estimation de la gravité des défauts dans les machines à induction en utilisant des outils d'intelligence artificielle. Mon travail inclut le développement d'un modèle mathématique qui intègre les défauts de court-circuit entre spires du stator sur trois phases d'un moteur à induction. J'ai mis en œuvre une approche de Réseau de Neurones à propagation avant (FFNN) pour la détection des défauts et la classification spécifique à chaque phase, suivie d'une approche par Réseau de Neurones à Perceptron Multi-Couche (MLP) pour détecter et classifier à la fois les défauts de court-circuit entre spires du stator et les défauts de tension d'alimentation déséquilibrée, ainsi que pour estimer la gravité des court-circuits. J'ai exploré différents types de Réseaux de Neurones Artificiels (ANNs) pour améliorer la détection des défauts, la précision de la classification et l'estimation de la gravité. Ma thèse est organisée en quatre chapitres : une

introduction traitant des défauts des moteurs à induction et des techniques de diagnostic, le développement et la validation de modèles de moteurs à induction à l'aide de MATLAB/Simulink, la mise en œuvre des processus FFNN et MLP pour la détection des défauts et l'estimation de la gravité, et un processus complet d'identification des défauts utilisant plusieurs ANNs de manière cascadienne. Mes compétences incluent la modélisation mathématique, la maîtrise de MATLAB/Simulink et l'expertise dans le développement de Réseaux de Neurones pour le diagnostic des défauts et l'optimisation dans les applications industrielles.

Dedicate

I dedicate this thesis to my beloved family and friends, whose unwavering love, support, and understanding have been my source of strength throughout this journey. To my husband Abdesalam CHERRATI, whose endless encouragement and sacrifices made it possible for me to pursue my academic endeavors. To my dear children Lyna and Amir, your patience and understanding during my moments of absence were truly remarkable. To my father Abdelhakim , and my mother Djamila , and my brothers Essedik, khieredin, moussa, omar, rabah and Abdelkader, thank you for believing in me and for always standing by my side. This achievement is as much yours as it is mine. I am eternally grateful for your love, guidance, and unwavering faith in me.

Thanks

This work was carried out within the Laboratory of Electrical Systems and Telecommunications (LABSET) of the Department of Electro-technics and automatics, at Saad Dahleb University of Blida1 (USDB1), under the joint supervision of Mr. Kamal KARA, Associate Professor and director of LABSET. I would like to express my deep gratitude to Mr. Kamel KARA. I also thank him for honors me by chairing the jury.

I extend my heartfelt thanks to Mr. SAARI Hamoud, Professor at National Higher Maritime School Bousmail, for his efforts and availability, as well as for accepting, despite their numerous commitments, to examine this work. I am particularly grateful to Mms. Alia BOUDISSA, Associate M.C.A at USDB1, for their participation in the jury. I particularly thank s Mms. Khadidja Elmerraoui, associate M.C.B at USDB1, for her availability.

My thanks also go to all colleagues in the Department of Electro-technics and automatics and USDB1, especially the members of LABSET.

I would like to express my sincere gratitude to all those who have contributed to the completion of this thesis. Special thanks to my thesis supervisor, Mr. Abdelaziz FERDJOUNI, Associate Professor at USDB1, for their guidance, support, and valuable feedback throughout this journey also for collaborating on this work and being present in every aspect of it. Additionally, I extend my appreciation to my family and friends for their encouragement and understanding. This work would not have been possible without their support.

Many people have contributed in various ways to this work. They are all thanked.

CONTENT TABLE

LIST OF SYMBOLS AND ABBREVIATIONS

Symbols	Designation
IM	Induction motor
BRB	Broken rotor bar
MCSA	Motor current signature analysis
FFT	Fast fourrier transform
PV	Park's vector
RMS	Root mean square
EMT	Electromagnetic torque
MMF	Magnetomotive force
SITSC	Stator inter turn short circuit
USV	Unbalance supply voltage
MCC	Multiple coupled circuit
MEC	Magnetic equivalent circuit
FEM	Finite element method
EKF	Extended kalman filter
AI	Artificial intelligent
K-NN	K nearest neighbor
HHT	Hilbert huang transform
NB	Naïve bias
SVM	Support vector machine
DT	Decision tree
FLT	Fuzzy logic technique
ANN	Artificial neural network
MLP	Multi-layer perceptron

FFNN	Feed forward neural network
RBNN	Radial basis neural network
RBENN	Radial basis extended neural network
GRNN	Generalized regression neural network
ML	Machine learning
DL	Deep learning
CNN	Convolutional neural network
RNN	Recurrent neural network
FI	Fault identification
FDC	Fault detection and classification
FSE	Fault severity estimation
IP	Instantaneous power [Watt]
PS	Phase shift [degree]
NSV	Negative sequence voltage [V]
ZT	Zero time
ZCT	Zero crossing time
ANN	Artificial neural network
MANNs	Multi Artificial neural networks
v	voltage [V]
i	Current [A]
θ	Angle of park transformation between stator and rotor
ω	Mechanical pulsation [rad/s]
ω_r	Rotor pulsation [rd/s]
ω_s	Stator pulsation [rd/s]
Φ	Magnetic Flux [Wb]
f_s	Stator frequency [Hz]
C_e	Electromagnetic torque [Nm]
C_r	Resistive Torque (of load) [Nm]
i^f	Short circuit fault current [A]
r_f	Fault resistance [Ω]
δ_i	Current factor
δ_v	Voltage factor

Figures and graphs List

Tables List

Introduction

Rotating electrical machines play a crucial role in various industrial sectors. Three-phase squirrel cage induction motors are the most commonly used due to their robustness, simple construction, and low cost. However, during their lifespan, these machines may be subject to various external or internal stresses that can lead to failures. The industrial requirements for reliability, maintainability, availability, and equipment safety are also very stringent. This is why the industrial sector is highly interested in a set of techniques to determine if they are in healthy condition or not.

In the literature, three types support the task of Induction Motors (IMs) fault diagnosis: model-free methods [6-22], model-based methods [23-32], and artificial intelligence (AI)-based methods [34-62].

Model-free methods rely on analyzing acquisition signals, offering the advantage of independence from internal system fluctuations. Thus, the information within the signals remains unaffected by possible modeling errors. Various signal processing techniques have been employed to analyze the spectral content of different signals from electrical machines, including currents, electromagnetic torque, vibrations, instantaneous powers …etc. One of the commonly used model-free methods is MCSA (motor current signature analysis); this last uses motor current signals [7]. It consists of assigning a spectral signature to each fault characterizing it. Moreover, the severity of the fault is a function of the amplitude of the harmonic frequency components [8]. Another method is based on d-q vector analysis. This technique transforms three-phase stator currents into two rotating components (d and q) by the Park's vector [9-10]; it simplifies analysis and reveals valuable insights into the motor condition. By creating a circular reference pattern between the d and q RMS (root mean square), any deviation from this circle in the Park's vector reveals a fault [12]. The detection through vibration [13, 17, 18], magnetic flux [13,19, 20], and instantaneous power [21, 22] require the addition of a supplementary sensor, facilitating the utilization of both frequency and time domain analyses for fault diagnosis. Magnetic flux and vibration signals were used for detecting and diagnosing electrical faults in the stator winding of three-phase induction motors [13]; those last are obtained via corresponding sensors. A correlation was established between major electrical faults (such

as inter-turn short circuits and unbalanced voltage supplies) and the signals of magnetic flux and vibration, enabling the identification of characteristic frequencies associated with these faults. The partial and total instantaneous powers were used to enhance diagnostic tools for electromechanical fault detection in electrical machines by identifying the most suitable diagnostic procedure based on measured power of motor and fault characteristics [21]. To assess the sensitivity of the electrical diagnostic tools, a severity factor is defined as the increase in amplitude of the fault characteristic frequency compared to the healthy condition. This factor facilitates the examination of diagnostic tool performance. Additionally, it demonstrates that the total instantaneous power diagnostic procedure exhibits the highest detection criterion values for mechanical faults, whereas for electrical faults, the most reliable diagnostic procedure correlates closely with the motor power factor angle and the motor-load inertia.

Model-based methods involve developing a mathematical model that describes the dynamic behavior of the induction motor under normal and faulty operating conditions. These models typically encompass equations representing the electrical, magnetic, and mechanical dynamics of the motor. Diagnosis occurs by comparing predicted values obtained by the model to measured values acquired by sensors related to the motor, such as current, voltage, speed, and electromagnetic torque. Any disparities between the measured and predicted values may indicate the presence of a fault. Further analysis is then performed to diagnose the fault. One of the familiar models is multiple coupled circuits also known as permeance network; it consists of multiple interconnected circuits. In this approach, each circuit is represented individually, and their interactions are characterized through coupling elements such as mutual inductance, capacitance, or resistance [24]. Another model called magnetic coupled circuit model, it is a theoretical framework used to analyze the behavior of magnetic circuits consisting of interconnected magnetic components such as inductances. It represents the flow of magnetic flux and the interaction between different elements in the circuit [23].

The dq model is a mathematical representation that describes the dynamic behavior of the motor in a rotating reference frame. In this model, the motor's electrical variables such as voltage, current, and flux are transformed from the stationary *abc* reference frame to the rotating *dq* reference frame. The dq reference frame rotates synchronously with the rotor flux, simplifying the analysis of the motor's dynamic behavior, including torque production, speed regulation, and response to various operating conditions and control

strategies. An observer model is a mathematical framework used to estimate the internal states of an induction motor based on its external measurements (stator currents). It operates similarly to a software sensor, continuously monitoring the motor's behavior and predicting its internal conditions, such as rotor flux, speed, and torque, without directly measuring them.

AI-based methods have garnered significant attention from researchers and exhibit promise in fault diagnosis applications for electrical IM. However, directly recognizing fault patterns proves challenging due to the variability and richness of response signals. Therefore, a typical fault diagnosis system comprises two key steps: data processing (feature extraction) and fault detection. Most AI-based fault diagnosis systems utilize preprocessing by feature extraction to transform high-dimensional input patterns into low-dimensional feature vectors for easier match and comparison.

Fault diagnosis is accomplished using machine learning methods such as k-nearest neighbor (k-NN), it operates by identifying the k- nearest data points in the training set to a given query point, and then assigns the query point a label or value based on the most common label among its neighbors (for classification) or the average value of its neighbors (for regression). Bayesian classifier is a probabilistic algorithm that utilizes Bayes' theorem to classify data points into predefined categories or classes based on their features and the probability of occurrence for each class. Support vector machine works by finding the optimal hyper-plane that best separates the data points into different classes or groups. The most commonly used Artificial neural networks in the field of fault diagnosis is artificial neural networks, it is a computational model inspired by the biological neural networks of the human brain, consisting of interconnected nodes (neurons) organized in layers. It is capable of learning complex patterns and relationships in data, making it a versatile tool for fault detection of induction motors. Additionally; deep learning approaches is the most recently used AI methods. It employs neural networks with multiple layers to learn complex patterns from vast amounts of data, enabling it to perform complex problems. They have begun to be applied in the field of fault diagnosis of IM in the few last years.

Our contribution consists of presenting a solution to the problem of detection, classification, and severity estimation of faults in the induction machine using artificial intelligence tools. The considered faults are Stator Inter Turn Short-Circuit and Unbalanced Supply Voltage. Initially, we develop a mathematical model of the induction

motor where the short-circuit fault is presented on all the three phases; it assumes that each phase has two coils in series, presenting a healthy portion and a short-circuited portion. This selection leads to present the fault as a ratio between the number of short-circuited turns and the number of total turns, this last is considered in order to facility the modeling of the IM.

Then, a Feed Forward Neural Network based approach is developed to detect and classify the Stator Inter Turn Short-Circuit fault according to the affected phase. The approach uses the three phase instantaneous power average as the features, where the highest value of average goes back to the damaged phase. Afterwards, a Multi-Layer Perceptron Neural Network based approach is used for the detection and classification of Stator Inter Turn Short-Circuit and Unbalanced Supply Voltage; also for the estimation of the percentage of short-circuits. This approach uses the total instantaneous power (maximum, minimum and average values), the phase shift between line current and phase voltage (in the three phases) and the negative sequence voltage as the best features of faults. Finally, several types of Artificial neural networks (which are typically Artificial Neural Networks) are explored for the detection, classification and severity estimation of both established faults. The proposed method uses three machine learning blocs in a cascaded manner, where the first machine learning bloc is used to detect and classify the upcoming fault. Afterward; the output of the first machine learning bloc activates the second and third machine learning blocs, where those last supposed to give the estimating percentages of Stator Inter Turn Short-Circuit and Unbalanced Supply Voltage.

The thesis is organized into four chapters.

The first chapter introduces a state of the art. In first, we discuss the different faults that could interrupt induction motor during their operation. Next, we talk about the various techniques that are used by researchers to diagnosis this fault. Those techniques are divided to classical and intelligent ones. Details are given throughout the chapter.

The second chapter presents the development of two models of induction motor. Using the stator-linked reference-frame, the first model is dedicated to an asymmetrical squirrel cage induction motor. The model calculation is detailed throughout the chapter. The second model is dedicated to a squirrel cage induction motor with stator inter turn short-circuit faults, assuming that each stator phase has two windings in series, presenting a healthy portion and a short-circuited portion. Next; using the Matlab/Simulink software,

the validation of both models of the induction motor is discussed with results obtained through simulation. The experimental study of the asymmetrical asynchronous machine is conducted, and the experimental results are compared to those obtained through simulation.

The third chapter introduces two processes dedicated to the detection, classification, and severity estimation of established faults. The first process is designed for identifying and categorizing stator inter-turn short circuit faults. Typically; the process is based on feed forward neural network. It categorizes the fault according to the specific phase in which it occurs. It uses current and voltage signals to evaluate the instantaneous power signal. Where this last is not used completely, but only the average of the signal is used. After a testing/error treatment the neural network is optimized to the perfect architecture, which is a neural network of an input layer that contain three neurons, a hidden layer that has five neurons and an output layer that has three neurons.

The second process is dedicated to the detection and classification of short circuits and unbalanced supply voltage. Furthermore, the severity estimation of stator inter-turn short circuits is calculated by providing the estimated percentage of the shorted circuits. Typically; the process is based on multi-layer perceptron neural network. It categorizes the fault into two type of faults, a stator or a supply voltage one. It uses current and voltage signals to evaluate the instantaneous power, the phases shift and negative sequence voltage signals. Where those last are not used completely, but a feature extraction procedure is implemented to extract the best features of faults. After a testing/error treatment the neural network is optimized to its perfect architecture, which is a neural network of an input layer that contain seven neurons, a hidden layer that has nine neurons and an output layer that has two neurons.

The fourth chapter presents multiple types of IM diagnosis, including:

- Fault detection and classification of stator inter-turn short circuit.
- Fault detection and classification of unbalanced supply voltage.
- Fault Severity Estimation of stator inter-turn short circuit.
- Fault Severity Estimation of unbalanced supply voltage.

The proposed Fault Identification process is carried out in a cascaded manner. In the first stage, the FI enables the detection of the fault category, whether it is a stator inter-

turn short circuit or an unbalanced supply voltage. Once the FI process recognizes the type of fault, the second stage is automatically activated. This stage allows the estimation of fault severity by providing the approximate percentage of the established faults.

Four types of Artificial neural networks were investigated to implement the proposed Fault Identification, including Feed Forward Neural Network, Radial Basis Neural Network, Radial Basis Extended Neural Network, and Generalized Regression Neural Network.

A general conclusion and further works concludes this thesis.

Chapter (1)
State of The Art

1.1. Introduction

This chapter offers an overview of faults in electrical machines, focusing particularly on Induction Motors (IMs) and fault detection. It is emphasized that these techniques can be readily extended to other types of electrical machines. The monitoring of electrical machines for diagnosis and fault prediction has garnered significant attention in recent years, given its substantial impact on the operational continuity of various industrial processes.

Effective diagnosis and early detection of faults play a crucial role in minimizing downtime and maintenance duration for the respective processes. Additionally, they contribute to averting harmful, and at times catastrophic, consequences of faults, leading to reduced financial losses. An effective detection procedure should employ minimal measures from the relevant process and extract a diagnosis that provides a clear indication of failure modes through data analysis in the least amount of time.

The primary objective of this chapter is to present faults and diagnostic methods applied to IMs. These methods are categorized into three groups: those using a mathematical model of the system, those involving the analysis of measured signals (referred to as model-free methods), and those employing artificial intelligent tools.

1.2. Generality about induction motor

IMs consist of a fixed stator and a rotating rotor. The stator has a magnetic circuit and windings that create a rotating magnetic field. The rotor has windings that carry induced currents from the rotating magnetic field. The torque generated by the motor is exerted on the conductors of the induced currents, causing the rotor to start and rotate in the same direction as the rotating magnetic field. [1]

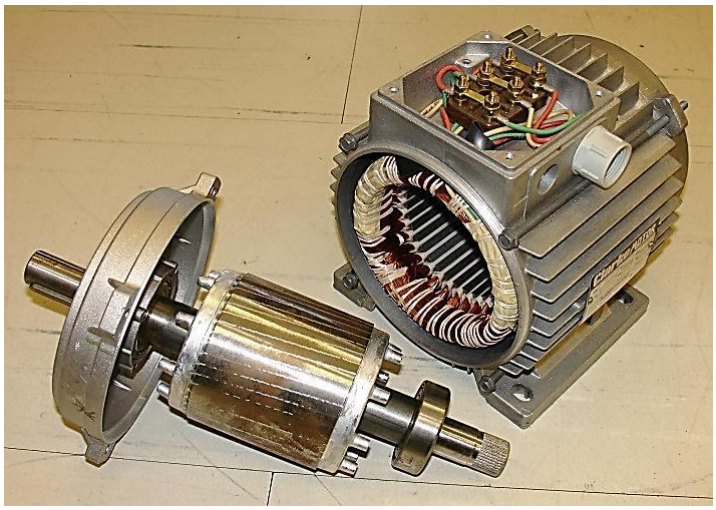

Figure 1.1 : Induction motor construction.

1.2.1. Induction motor construction

We propose, in this section, to briefly recall the constitution of the IMs. This description will allow us to better understand the faults of this machine, in their physical dimension. IMs can be broken down, from a mechanical point of view, into three parts distinct:

- The stator, fixed part of the machine where the electrical supply is connected;
- The rotor, rotating part which allows the mechanical load to rotate;
- The bearings, the mechanical part which allows the motor shaft to rotate.

1.2.1.1 Stator

The stator of an IM is made up of ferromagnetic sheets in which the stator windings are placed. For small machines, these sheets are cut in one piece, while they are cut into sections for larger power machines. These sheets are usually coated with varnish to limit the effect of eddy currents; they are assembled together using rivets or welds to form the stator magnetic circuit. The stator windings are placed in the slots provided for this purpose. These windings can be inserted in an interlocking, wavy, or even concentric manner. The insulation between the electrical windings and the steel sheets is done using insulating materials which can be of different types depending on the use of the IM. The stator of an IM is also provided with a terminal box to which the power supply is connected. Figure 1.2 presents the different parts that form the stator of an IM [3].

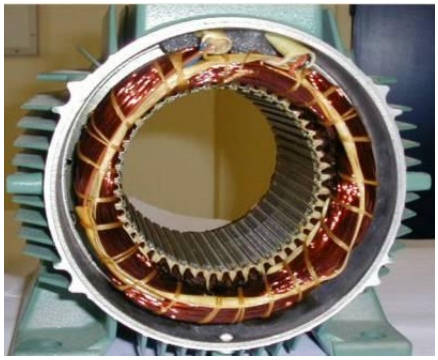

Figure 1.2 : Stator

1.2.1.2. Rotor

The rotor magnetic circuit is made of ferromagnetic sheets that are generally of the same origin as those used to build the stator. The rotors of IMs can be of two types: wound or squirrel-cage. Wound rotors are constructed in the same way as the stator winding. The rotor phases are then available thanks to a system of slip rings and brushes positioned on the shaft of the machine. Regarding squirrel-cage rotors, the windings are made of copper bars for large-power motors or aluminum for lower-power motors. These bars are short-circuited at each end by two short-circuit rings, made of copper or aluminum. Figure 1.3 shows the different elements that forms a squirrel-cage rotor. In the case of squirrel-cage rotors, the conductors are made by casting an aluminum alloy or by pre-formed copper bars that are fretted into the rotor sheets. Generally, there is no insulation between the rotor bars and the magnetic circuit. However, the resistivity of the alloy used to build the cage is low enough so that the currents do not flow through the magnetic sheets, except when the rotor cage has a broken rotor bar (BRB) [2].

Figure 1.3 : Rotor

1.2.1.3 Bearings

The heart of a bearing lies in its three key components: inner and outer races, rolling elements, and a (sometimes optional) cage. The races, like smooth tracks, guide the movement of the rolling elements, typically tiny balls or rollers. These elements act as tireless intermediaries, rolling instead of sliding to drastically reduce friction and wear. The cage, when present, plays a crucial role in keeping these rolling elements evenly spaced, preventing them from touching and causing further friction or damage. This harmonious interplay of parts allows bearings to carry impressive loads while maintaining smooth, efficient operation [2].

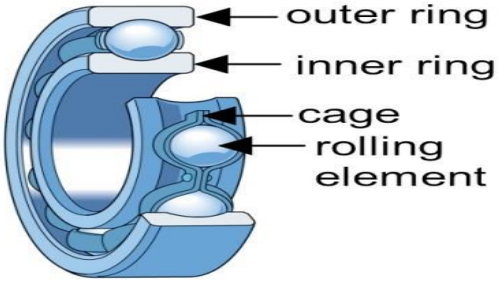

Figure 1.4 : Bearings

1.2.2. Induction motor main faults

Although IMs are known to be robust, they can sometimes present different types of faults which can be either originated by electrical or mechanical source. These faults can escalate into failures, which may either be predictable or, unfortunately, stem from a wide range of causes. Indeed, a minor problem at the manufacturing stage may be causing a fault, as well as improper use of the machine. A statistical study carried out by [3] on IMs operated in the field of the petrochemical industry reveals that certain faults are more frequent than others, as shown by the diagram (figure 1.5) by presenting the percentage of faults likely to affect these high-power machines. This distribution shows that the faults of high-power machines come from mainly bearings and stator; this is due to mechanical constraints more important in the case of these machines [4].

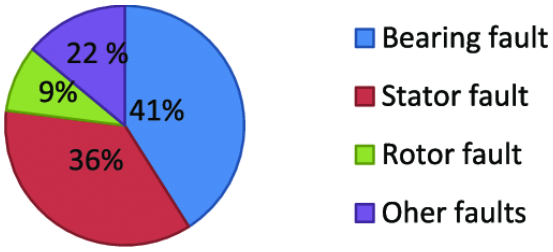

Figure 1.5 : Statistical studies [3]

1.2.2.1 Mechanical faults

More than 40% of IMs faults are mechanical faults. These faults may be bearing faults, eccentricity faults, etc...

1.2.2.1.1 Bearings faults

The main reason for machine failures is ball bearing faults which have many causes such as lubricant contamination, excessive load or even electrical causes such as the circulation of leakage currents induced by PWM inverters [4]. Bearing faults generally cause several mechanical effects in the machines such as an increase in noise level and the appearance of vibrations.

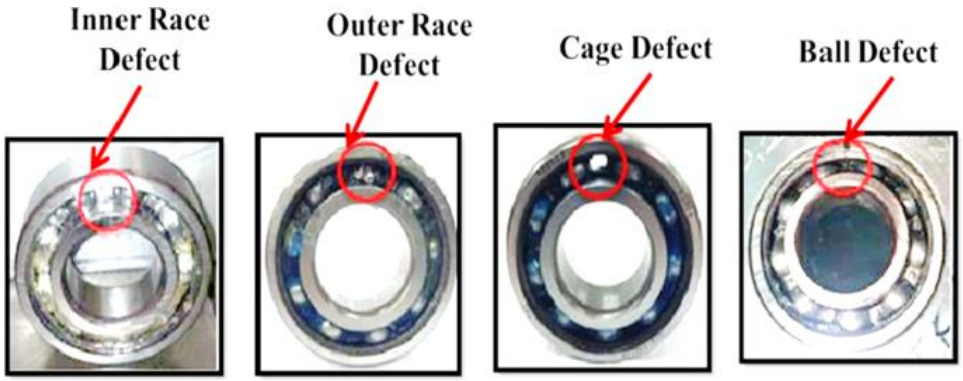

Figure 1.6 : Bearing faults

1.2.2.1.2 Eccentricity faults

The consequences of mechanical faults generally appear at the air gap: by static, dynamic or mixed eccentricity [5], as shown in (figure 1.7):

- The static eccentricity is generally due to a misalignment of the axis of rotation of the rotor relatively to the stator center.

- The dynamic eccentricity can be caused by a deformation of the rotor cylinder, or damage to ball bearings.
- Mixed eccentricity, the most common, is the combination of static and dynamic eccentricity.

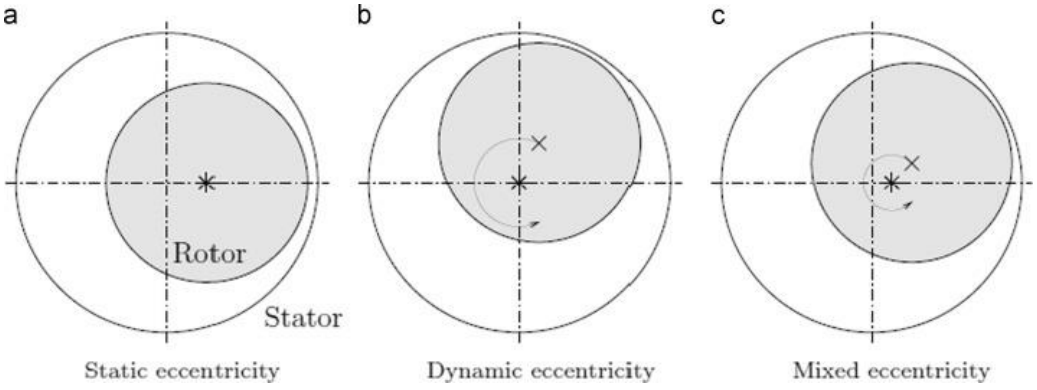

Figure 1.7 : Eccentricity faults

1.2.2.2 Electrical faults

Electrical failures at the stator level or at the rotor level can have several forms and several causes. They are clarified in next.

1.2.2.2.1 Stator faults

Stator faults can manifest themselves in the form of an inter-turn short circuit, a short circuit between two phases, or a short circuit between one phase and the ground [5] (figure 1.8). It is schematized by the direct connection between two points of the winding. The short circuit between phases appears preferentially in the heads of coils. The short circuit between turns of the same phase can appear either at the level of the heads of coils or in the slots, which results in a decrease in the number of effective turns of the winding. A short circuit between phases would cause a sharp stop of the machine. However, a short circuit between one phase and the neutral (via the grounding) or between turns of the same phase. It leads to a phase imbalance, which has a direct impact on the electromagnetic torque [4].

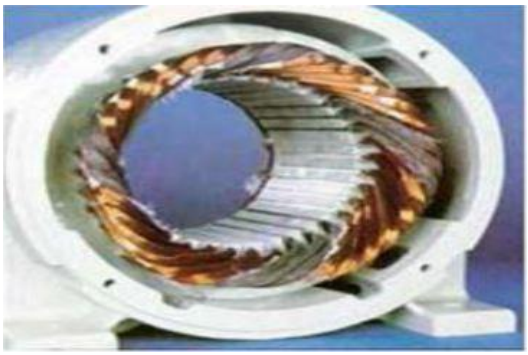

Short circuit of a phase

Short circuit between phases

Short circuit in the slots

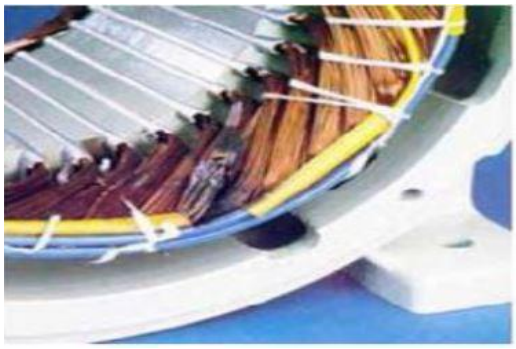

Degradation caused by overvoltage

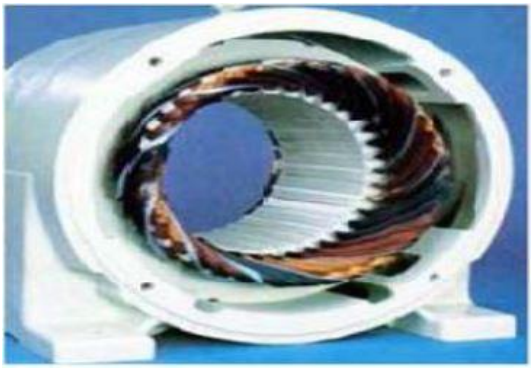

Unbalance of supply voltage

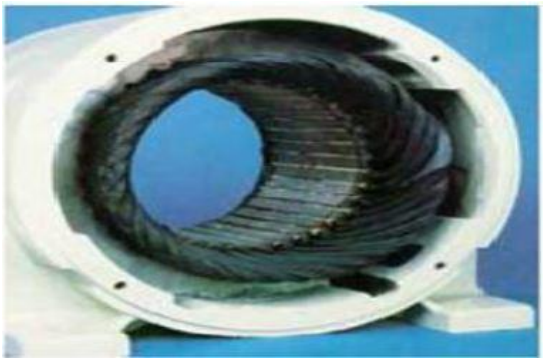

Damage due to overload

Figure 1.8 : Stator faults [5]

1.2.2.2.2 Rotor faults

Similar to its stator counterpart, a wound rotor can encounter comparable electrical issues. However, for the robust cage rotor, faults may originate from BRBs or rings (see Figure 1.9). These fractures are often the result of stresses induced by frequent starts or overheating, and can also stem from manufacturing faults such as air bubbles or shoddy welds [4]. When a break occurs, it disrupts the current flow causing disturbances in both torque and current signals which become more pronounced in systems with high inertia. Interestingly in systems with lower inertia; the disturbances manifest as wobbling in mechanical speed and stator current amplitude. Ring portion breakage is equally

problematic, occurring as frequently as bar fractures. These cracks typically result from manufacturing faults such as bubbles or thermal mismatches between bars and rings, with rings generally carrying heavier currents. Improper ring sizing, harsh operating conditions, or torque overloads can all contribute to their failure.

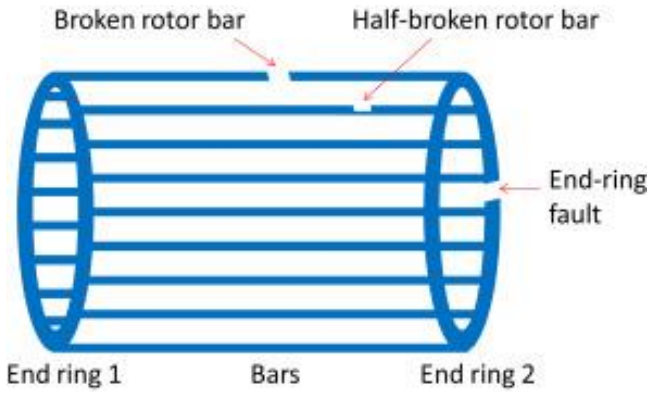

Figure 1.9 : rotor faults

A bar breakage fault does not cause the machine to stop; due to the fact that the current which crossed the BRBs is re-distributed over the adjacent bars. These bars are then overloaded, which can lead to their rupture, and so on until the rupture of a sufficiently large number of bars to cause the machine to stop.

Given the array of potential faults and their associated consequences, the implementation of monitoring techniques has become imperative for users of electrical machines. Moreover, designers are increasingly showing interest in developing these monitoring methodologies that can be used for the detection of multiple faults. In the next section, we discuss the different types of methods that support the IM diagnostic task.

1.3 Induction motor diagnosis methods

1.3.1. Model-free methods

Those Methods are based on the analysis of measured signals; they have the advantage of being independent of internal fluctuations of the IM. Thus, the information contained in the signals is not affected by a possible modeling error. Several signal processing techniques have long been used to analyze the spectral content of different signals from electrical machines such as: currents, electromagnetic torque, vibrations, magnetic flux, instantaneous powers, speed, etc… [6]

1.3.1.1 Diagnosis by stator current analysis

The analysis of the stator currents occupies a privileged place in the diagnosis of IMs without models. Stator currents are easily accessible and carry information about the fault in their spectral contain. This technique is known under the abbreviation MCSA (Motor Current Signature Analysis). It was the subject of several research works; it consists of assigning a spectral signature to each fault characterizing it. In the same context, it was demonstrated that the severity of the fault is a function of the amplitude of the harmonic frequency components that it generates, in particular who's already present in the healthy IM. Panadero et al. [7] present an online/offline MCSA with advanced signal and data processing algorithms, based on the Hilbert transform. In particular, it is very difficult to detect BRBs when the motor is operating at low slip or under no load. Therefore, Panadero proposed advanced signal and data processing algorithms. for achieving MCSA efficiently. They consist of a sample selection algorithm, a Hilbert transformation algorithm of the stator-sampled current and a spectral analysis via FFT of the modulus of the resultant Hilbert transformation vector. Rangel-Magdaleno et al. [8] use MCSA to detect BRB on IMs under different mechanical load condition. The proposed algorithm first identifies the motor load and then the motor condition. The proposed method has been implemented in a field programmable gate array, to be used in real-time online applications; it reached a 95% accuracy of failure detection.

1.3.1.2. Diagnosis by dq vector analysis

Induction motor fault diagnosis gets a boost with d-q vector analysis. This advanced technique transforms three-phase stator currents into two rotating components (d and q) by the Park's vector (PV); this technique simplifies analysis and reveals valuable insights into the motor's health. Its sensitivity makes it particularly effective for detecting and characterizing common faults like BRB, stator windings issues, and bearing faults. Yihan and Acosta [9-10] explore the PV trajectory. It is a circle that shows the ratio between the maximum and minimum RMS (root mean square) of the DQ components; its eccentricity is near to zero under healthy condition. This eccentricity shows difference when different fault types occur, the value of the ratio is larger when phase-phase short circuit occurs compared with inter-turn and phase-ground short circuit faults; the eccentricity of Park's Vector trajectory would increase with the fault degree severity.

Cardoso et al. [11] describe the use of an extended PV (EPV) approach for diagnosing the occurrence of stator winding faults in real time operating IM. Experimental results, obtained in the laboratory, corroborate that these faults can be detected in the EPV approach, by the identification of a spectral component at twice the fundamental supply frequency.

While detecting motor faults with Park's vector is simple. The Multiple Park's Vector (MPV) approach tackles this challenge by extracting distinct characteristics for different faults like stator windings, rotor windings, unbalanced voltage, and bearings [12]. These characteristics exist even under healthy conditions, but are slightly unbalanced due to the motor's natural asymmetry. Tushar G. et al [12] assume that the MPV cleverly balances these patterns, creating a circular reference pattern. Any deviation from this circle in the Park's vector reveals a fault like shown in (figure 1.10), with the specific shape and size indicating the type and severity. Tested on experimental motor and validated by simulations, MPV promises accurate and robust fault classification for motor operation.

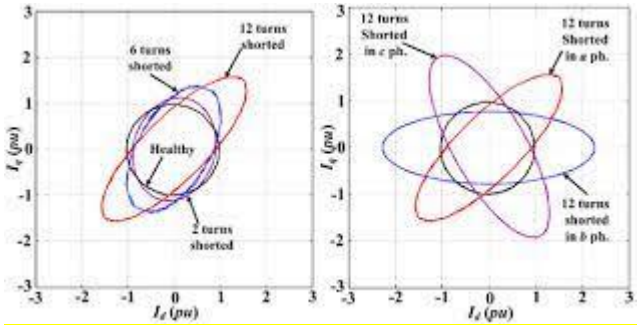

Figure 1.10: Short circuit detection using park's vector approach [12]

1.3.1.3. Diagnosis by measuring electromagnetic torque

The electromagnetic torque (EMT) developed in the machine comes from the interaction between the stator field and rotor field. Consequently, any fault either at the stator or at the rotor, directly affects EMT. The spectral analysis of this signal, gives relevant information on the state of the motor. However, the need for fairly expensive equipment to acquire this EMT represents the major drawback of this method. [14-16] have used the EMT to detect rotor faults like BRBs and misalignment.

1.3.1.4. Diagnosis by measuring vibrations

Diagnosis by vibration analysis is one of the mechanical techniques which are used to detect faults in electrical machines. A vibration is often accompanied by an audible

noise which can be high even for low vibration amplitudes. Fault diagnosis using vibration analysis is the best-known method in practice [6]. The radial forces created by the air gap field, cause vibrations in the IM. These forces are proportional to the square of the magnetic induction [6]. Machine vibrations can be captured by accelerometers placed on the bearings in the axial, vertical and radial directions. The spectra of the vibration signals from the faulty motor are compared with those of references recorded when the motor was in healthy condition. This method allows the detection of both electrical and mechanical faults since the distribution of the magnetic induction in the air gap is the product of the magnetomotive force (MMF) and the permeance. The MMF contains the effects of the asymmetries of the stator or the rotor and the permeance depends on the variation of the air gap (because of the openings of the stator, rotor slots and the eccentricity). However, the cost of vibration sensors which is relatively high, as well as the difficulties encountered in connecting these sensors (accessibility problem) represents the limits and disadvantages of this method [6]. [13] Lamim Filho et al focuse on detecting and diagnosing electrical faults in the stator winding of three-phase induction motors through magnetic flux and vibration signals. Those last are obtained via corresponding sensors. A correlation was established between major electrical faults (such as inter-turn short circuits and unbalanced voltage supplies) and the signals of magnetic flux and vibration, enabling the identification of characteristic frequencies associated with these faults. Experimental results demonstrated the effectiveness of combining these techniques for detection, diagnosis, and monitoring purposes. Betta et al. [17] use vibration signals, those last are on-line acquired and processed to obtain a continuous monitoring of the machine status. In case of a fault, the system is capable of isolating the fault with a high reliability. Jafar zarei et al. [18] use an intelligent filter to cut-off the non-necessary component in a vibration signal in order to detect bearings faults such as inner and outer race.

1.3.1.5 Diagnosis by measuring the leakage axial magnetic flux

The electromechanical conversion of energy is located in the air gap. This conversion is therefore affected by any magnetic, mechanical, electrical or electromagnetic fault in the rotor or in the stator. The air gap flux is by the same token the induction magnetic in this air gap, the flux embraced in the stator windings, or again the leakage flux in the axis of the rotor are parameters which, because of their sensitivity to any imbalance of the machine, merit to be analyzed. The axial flux is the result of the effect of currents on the ends of the machine (heads of coils, short-circuit rings), it is always present in

electrical machines because of asymmetries inherent to their manufacture. The study of flux variations can therefore be a solution to detect and locate a fault through the use of search coils placed at outside the machine, perpendicular to the rotor axis. Manés F. Cabanas et al. [19] report a new diagnostic method, based on the measurement of the magnetic flux linked by one stator coil, which allows perfect simple discrimination between the actual presence of rotor asymmetries and the spurious effects caused by the oscillations in the load torque of the driven IM. Humberto henao et al. [20] has proved that a simple external stray flux sensor is more efficient than the classical MCSA to detect stator inter-turn short-circuits (SITSC) in three-phase IM. The new result is that, even in the presence of power supply harmonics, it is possible to easily detect the stator winding faults in the low-frequency range of the flux spectrum with low-frequency resolution.

1.3.1.6. Diagnosis by frequency analysis of measured instantaneous power

Using instantaneous power for fault detection in IMs, has been the objective of numerous works such as [21] and [22]. The instantaneous power is the product of the supply voltage and the current absorbed by the IMs. Therefore, the amount of information provided by this quantity is greater than that brought by the current alone; the spectrum of the instantaneous power contains an additional component located at the fault frequency. Liu et al. [22] leverages the spectral analysis of instantaneous power to diagnose both BRB and eccentricity faults in squirrel-cage induction motors. Their theoretical analysis demonstrates that the instantaneous power spectrum lacks components at the fundamental supply frequency, facilitating the isolation of fault signatures due to the aforementioned faults. This enables effective separation of mixed faults and fault severity quantification.

1.3.2. Model-based methods

Models of motor operation under healthy and faulty conditions are useful for investigating the operational characteristics of faulty motors without destructive testing. The modeling of an induction machine can be broken down into four broad categories as illustrated in Figure. 1.11 [23].

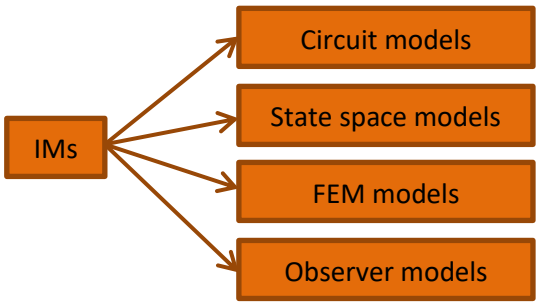

Figure.1.11: Model based categories [23]

1.3.2.1 Multiple Coupled Circuit model

In the multiple coupled circuit (MCC) equation modeling approach, the stator and/or rotor windings are represented by an equivalent electrical circuit consisting of an inductance in series with a resistance [24].

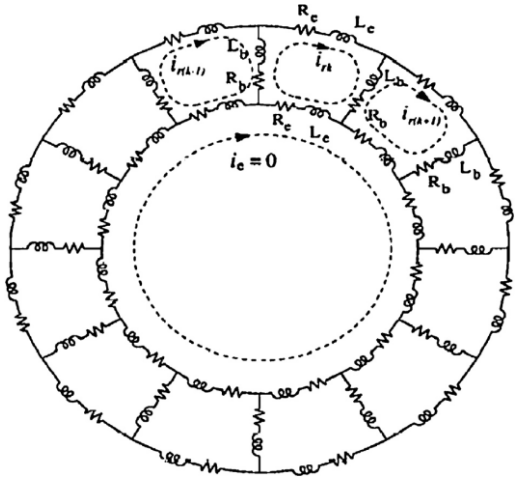

Figure 1.12: MCC topology [23]

The self and mutual inductances between the stator and rotor of the machine play an important role in this modeling method because they contain the signature of the different phenomena that can occur in the IMs. These inductors can be calculated using either winding functions theory [6], which requires precise knowledge of the shape of the machine's windings, or by decomposing the air gap induction into a Fourier series. This type of modeling can therefore take into account spatial harmonics. Time harmonics generated by a three-phase AC power supply or by a static converter have been

incorporated into the modeling of the IM's power supply. The assumptions of this approach are:

- The magnetic circuit is linear (the relative permeability of iron is much greater than 1). The skin effect is neglected.
- The rotor bars are insulated from each other, which eliminates inter-bar currents and their effects within the rotor cage.
- The machine's iron losses, capacitive effects, and thermal effects are neglected.

1.3.2.2. Magnetic Equivalent Circuit model

Magnetic Equivalent Circuit (MEC) model, also known as permeance network model or flux tube models, it is based on detailed magnetic modeling of the machine. The magnetic field distribution within the motor is used to evaluate its performance since it contains complete information on the stator, rotor and mechanical parts of the motor. The magnetic equivalent circuit (MEC) method is based on decomposing the magnetic circuit of the machine into elementary flux tubes [23]. A MEC representing the geometry of the machine is created, with each MEC calculated from a flow tube. This circuit can be compared to a regular electrical circuit, except that fluxes and magnetic potential differences are used instead of currents and electrical potential differences. This approach allows the characteristics of the iron used in the construction of the IM to be taken into account. In fact, the calculation of different MECs can only be done by setting a precise value for the relative permeability of iron. The rotational movement of the machine is taken into account through variable air gap MECs that depend on the angular position of the rotor. The MEC method is less precise than the finite element method, but more precise than analytical modeling. The advantage of this method is that it allows for rapid numerical resolution.

1.3.2.3 Finite Element Model

The finite element model (FEM) is a numerical method used to solve electromagnetic field problems. It is used in IM diagnosis to understand and quantify the local consequences of faults on different parts of the IM. The FEM works by dividing the

machine's magnetic circuit into small elements, each of which is considered to be linear. This allows the FEM to take into account the geometry of the machine, the saturation of magnetic materials, and the skin effect in the rotor bars. In the field of IM diagnosis, the FEM is used to study the local effects of faults such as BRB and SITSC in the phases. For example, the FEM can be used to study the local heating and electro-dynamic stress on the bars neighboring BRBs. The FEM can also be used to study the local magnetic and thermal impacts of SITSC. Considering the local electromagnetic behavior allows for a more accurate model of the motor. The FEM also takes into account the electrical equations of the machine, which reduces the simplifications made in classical models. This results in a model that is closer to the real electrical machine. Vaseghi et al [25] have developed a time stepping two- dimensional FEM for modeling and analyzing of IM with SITSC fault. FEM analysis is used for magnetic field calculation and the magnetic flux density and vector potential of machine is obtained for healthy and faulty cases. By comparing the magnetic flux distribution of healthy and faulty machines, the detection of SITSC fault is evident. Delforge et al. [26] have developed two model based on MEC and FEM. Simulation results on an induction machine are presented and compared showing a good agreement between the two models and the motor.

1.3.2.4. Modified DQ-model

The traditional dq transient model of induction machines operates under the assumption of sinusoidal distribution for stator and rotor windings, as well as the MMF. However, the rotor cage of an IM is non-sinusoidally distributed. Despite this, it can be replaced by an equivalent distributed winding. This DQ model of induction motors has been used to study some phenomena such as voltage drops and oscillatory torque that may occur during start-up and other severe motor operations. DQ models are based on the Park transformation, which converts current and voltage signals from the *abc* reference frame to the dq reference frame. Modified dq models have been used mostly to study rotor bar faults [27-28], although they have also been applied to the study of SITSC in one or more phases [29] and eccentricity [30]. However, this model requires a modification in model structure for each fault mode. Despite this, it is widely used for the detection of multiple stator faults.

1.3.2.5. Observer model

Observer-based fault diagnosis method for induction motors is another powerful approach for detecting and identifying IMs problems. Observer-based techniques focus on reconstructing the internal state of the motor using readily available measurements like stator currents and voltages. In fact; these models observe the motor's behavior based on external measurements. They provide estimates of internal states like rotor currents, speed, and flux linkages, which are typically difficult to measure directly. Thus; these models compare the estimated internal states of motor with a healthy motor model where deviations can be identified. These deviations can then be analyzed to locate specific faults within the motor, such as bearing fault, BRBs, or SITSCs. Different fault signatures in the estimated states can be mapped to specific fault types, enabling isolation and diagnosis. Observer model has very important advantages due to the simple implementation of them; where they require only readily available external measurements, making it cost-effective and easy to implement in real-world applications. Their robustness where it guaranties a less susceptible to sensor noise and uncertainties compared to some other methods. It can also be used for online fault detection and monitoring for preventive maintenance. Observer-based diagnosis method has a limitation points. These last manifests in model dependency, relies on accurate motor models, which can be challenging to develop for complex motors or under transient conditions. Sensitivity to sensor faults: Faulty sensors can lead to inaccurate state estimates and incorrect fault diagnosis. One of the powerful observers in IM fault diagnosis is the Kalman filter. This approach leverages the Kalman filter's state estimation capabilities to predict the internal state of an induction motor and detect potential faults. By dynamically updating its estimates based on noisy measurements and a motor model, the Kalman filter accurately tracks crucial parameters like rotor speed and fluxes, even when direct measurement is infeasible. Jian-Da et al. [31] have presented an application of adaptive order tracking fault diagnosis technique based on recursive Kalman filtering algorithm. A high-resolution order tracking method with adaptive Kalman filter is used to diagnose the fault in a gear set and damaged machine turbocharger wheel blades. Elmeraoui et al. [32] propose an observer-based fault detection of a delta connected IM model that takes the SITSC into account. It allows the generation of residual using Extended Kalman filter (EKF). To overcome the problem of the EKF initialization, the cyclic optimization method is applied to determine its tuning parameters. The proposed approach is done in real-time in order to quickly detect fault and estimate its severity.

1.4. AI- based methods

Artificial intelligence (AI) has attracted great attention from many researchers and shows promise in rotating machinery fault recognition applications. However, due to the variability and richness of the response signals, it is almost impossible to recognize fault patterns directly. Therefore, a common fault diagnosis system often consists of two key steps: data processing (feature extraction) and fault recognition. Most intelligent fault diagnosis systems are built based on preprocessing by feature extraction algorithms to transform the input patterns into low-dimensional feature vectors for easier match and comparison. The feature vectors are then used as the input of AI techniques for fault recognition. This step amounts to mapping the information obtained in the feature space to machine faults in the fault space. Numerous AI tools and techniques have been used in fault diagnosis of rotating machinery, including convex optimization, mathematical optimization, and classification-, statistical learning-, and probability-based methods. Specifically, machine learning methods they have been widely used, such as k-nearest neighbor (k-NN) algorithms, Bayesian classifiers, support vector machines (SVMs), and artificial neural networks (ANNs). There are also other AI methods which are deep learning approaches, they are the most recently used ones and they largely have begun to be applied in the field of fault diagnosis. [33]

1.4.1. Machine learning methods (ML)

1.4.1.1 K-nearest neighbor

The k-nearest neighbors (KNN) algorithm is a simple and intuitive supervised classification algorithm that classifies target points (unknown class) based on their distances to points in a training set (whose classes are known). KNN works by first finding the k most similar points in the training set to the target point (figure 1.13). The class of the target point is then assigned based on the majority class of the k most similar points. KNN can be used with both quantitative and qualitative data. For quantitative data, the distance between two points is typically measured using a Euclidean distance metric. For qualitative data, the distance between two points is typically measured using a Hamming distance metric. KNN is a useful algorithm that can be utilized for a variety of classification tasks. It is particularly well-suited for tasks where the training data is limited or where the data is noisy [34].

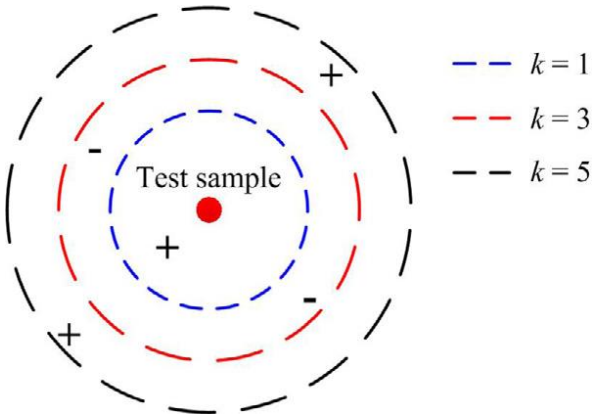

Figure 1.13 : the diagram of K-NN [33]

In literature, k-NN has been proved to work well and applied widely in fault diagnosis. As an instance-based algorithm, k-NN can be used both for classification and regression. Jung and Koh [35] exploit the multi-scale energy analysis of discrete wavelet transformation to obtain a low-dimensional feature subset of data. The reduced subset of data is used as the input of k-NN for bearing fault classification. In [36], Pandya et al. present a bearing fault diagnosis method, which uses the acoustic signal to extract features by a Hilbert-Huang Transform (HHT). Those features are used as the input of k-NN classifiers. This paper also compares the performance of various AI methods.

1.4.1.2. Naïve Bayes

A Naive Bayes (NB) classifier is a simple and powerful probabilistic machine learning algorithm used for classification tasks. There are different types of Naive Bayes such as Gaussian Naive Bayes, Multinomial Naive Bayes and Bernoulli Naive Bayes. It uses Bayes' theorem with the strong assumption of independence between features to calculate the probability of a data point belonging to a specific class. Its functioning principle involves calculating the probabilities of each class given the input features and then selecting the class with the highest probability as the output prediction. Naive Bayes classifiers serve as a viable option for initial fault detection in IMs. Because, it requires minimal training data and is computationally inexpensive, making it suitable for real-time fault detection in IMs. Besides, it is useful when dealing with scarce or expensive sensor data, providing reliable diagnoses even with limited information. It provides straightforward logic behind fault classifications, aiding in easier comprehension of diagnosis outcomes and aligns well with the categorical nature of many fault diagnosis features in IMs. However, caution is necessary. Its assumption of feature independence might not hold in complex IM systems, leading to potential inaccuracies when features

interact. Its limitations in handling complex fault scenarios struggles to capture intricate relationships among features in scenarios involving multiple or complex faults, impacting its ability to isolate specific faults accurately [34].

Naive Bayes is a generative model with high learning and predicting efficiency. For SITSC fault diagnosis of IMs; [37] Seshadrinath et al. compare the induction machines diagnosis results from other AI algorithms to a NB, based on features extracted by the dual tree complex wavelet transform, results show the good accuracy of NB. Duan et al. [38] present a segmented infrared image analysis for rotating machinery fault diagnosis, which applies an image segmentation approach to enhance the feature extraction to infrared image analysis. Then, a feature fusion method is applied to obtain features from selected regions for fault diagnosis by NB classifier.

1.4.1.3. Support Vector Machine

A Support Vector Machine (SVM) is a supervised machine learning algorithm used for classification and regression tasks. It is particularly effective for classification problems and has been applied to fault identification of IMs due to its strengths. In fact, an SVM model analyzes data for classification purposes. It works by finding the optimal hyper-plane that best separates different classes in the input feature space. This hyper-plane aims to maximize the margin between classes, thus improving generalization and classification accuracy. Figure 1.14 show the optimal hyper-plane for a binary classification by an SVM classifier. SVMs are efficient even in high-dimensional spaces, making them suitable for fault identification in IMs with multiple features and complex datasets. SVMs use kernel functions to map input data into higher-dimensional spaces, enabling the classification of non-linear data. This capability is valuable when dealing with diverse fault patterns in IMs. SVMs tend to generalize well and are less prone to over-fitting problems, ensuring reliable fault identification by avoiding learning noise in the data [34].

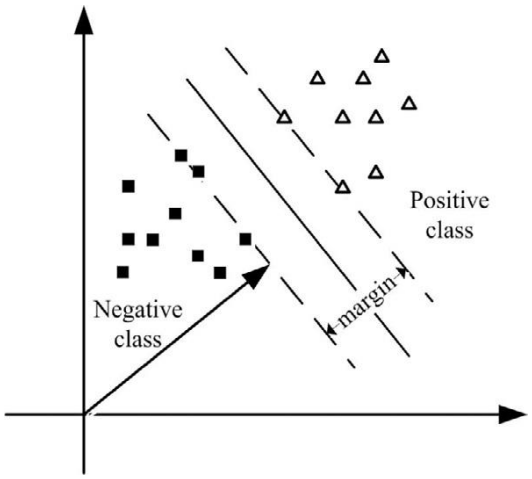

Figure 1.14: The optimal hyper plane for a binary classification by SVM [33].

[39] Soualhi et al. developed a way to diagnose bearing problems, they use the HHT Huang Transformation to extract health indicators from vibration signals to tack the degradation of critical components in bearings. Then the degradation states are detected by SVM. Unlike Li et al. [40], Instead of using vibration signals in traditional methods, they used SVM to analyze the acoustic emission signals for the diagnosis and prediction of different rotor fissures depth. Banerjee and Das [41] uses sensor data fusion to investigate a hybrid method for fault signal classification by using an SVM classifier and STFT technique.

1.4.1.4. Decision Tree

A Decision Tree (DT) algorithm is a supervised machine learning technique used for both classification and regression tasks. It is a flowchart-like tree structure where each internal node represents a feature, each branch represents a decision rule, and each leaf node represents an outcome (class label or numerical value) (figure 1.15). In fact, DTs organize data into a tree-like structure where each node denotes a decision based on a particular attribute, leading to branches that represent possible outcomes or further decisions. [34]

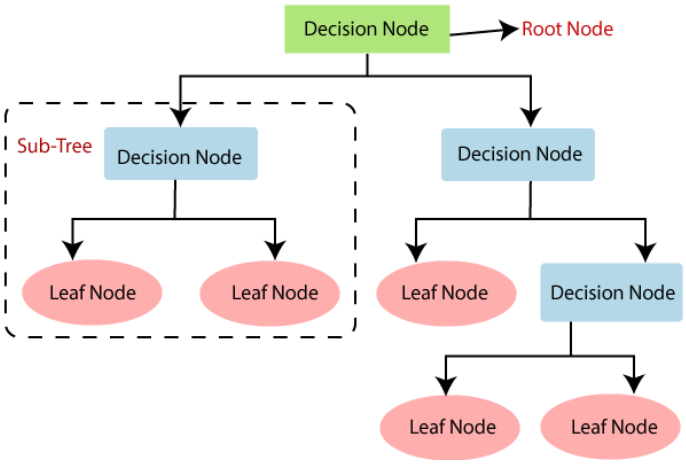

Figure 1.15 Decision Tree process.

Like illustrate in figure 1.15; Starting from the root node, each internal node tests a specific attribute, and the outcome determines which branch to follow. This process continues until a leaf node, which holds the final decision or prediction. DTs have been utilized effectively in fault diagnosis for induction motors (IMs) due to their ability to handle complex decision-making processes and their interpretability. Saimurugan et al. [42] employ vibration signals to extract the features to identify the status of a machine. DT algorithm was used to select the prominent features. These features were given as inputs for training and testing two SVM models of classification, both of the models demonstrate good accuracies. Aydin et al. [43] propose a new approach that requires the measurement of only one phase current signal in order to construct the phase space representation. Then each phase space is converted into an image, and the boundary of each image is extracted by a DT boundary algorithm. Therefore, an AI detection algorithm has been designed to detect BRBs fault. The results indicate the high recognition rate of the proposed approach compared to other ones.

1.4.1.5. Fuzzy Logic Technique

A fuzzy logic technique (FLT) refers to the utilization of fuzzy logic principles and methodologies to handle uncertainty and imprecision in decision-making, control systems, pattern recognition, and various other applications. It involves employing fuzzy sets, membership functions, fuzzy rules, and fuzzy inference to model human-like reasoning and deal with ambiguous or vague data (figure 1.16). Fuzzy sets which allow elements to have degrees of membership within a set, representing the gradual transition between membership and non-membership. Membership functions which assign membership

values to elements based on their degree of belongingness to a fuzzy set. Fuzzy rules which use if-then rules to relate input variables and their associated fuzzy sets. Fuzzy Inference processes the fuzzy rules and membership functions to derive crisp output values from fuzzy inputs. [34]

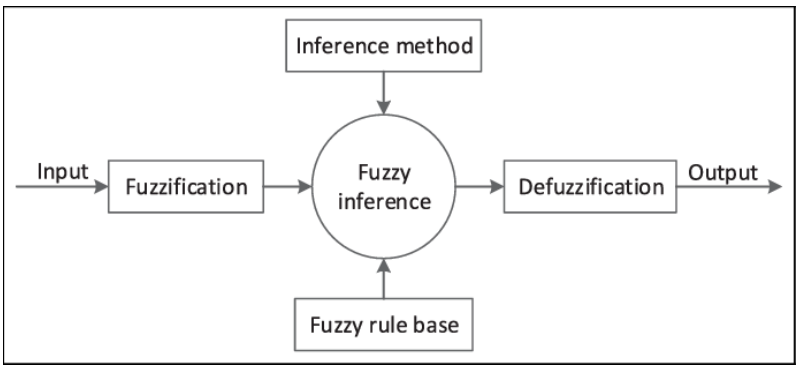

Figure 1.16: Fuzzy logic inference

Fuzzy logic is extensively used in control systems, decision making and pattern recognition. As well in fault diagnosis of induction motors, that is due to their excel in handling imprecise and uncertain information, providing a more flexible way to model human-like reasoning. They can handle noisy data and variations more robustly compared to other methods. Lakrout et al. [44] present a method for detecting stator winding faults based on stator current analysis. A fuzzy logic approach is used to make decisions about the state of the stator winding (good, damaged or seriously damaged). Load Torque variations is one of the parameters that can disturb the SITSC fault detection, [45] Lashkari opt for fuzzy approach to detect and diagnose the severity of SITSC fault with the taking into account of the load variations.

1.4.1.6. Artificial neural network

Artificial Neural Networks (ANNs) are computational models inspired by the human brain's neural structure and task (figure 1.17). They consist of interconnected nodes arranged in layers, allowing for complex data processing and pattern recognition problems.

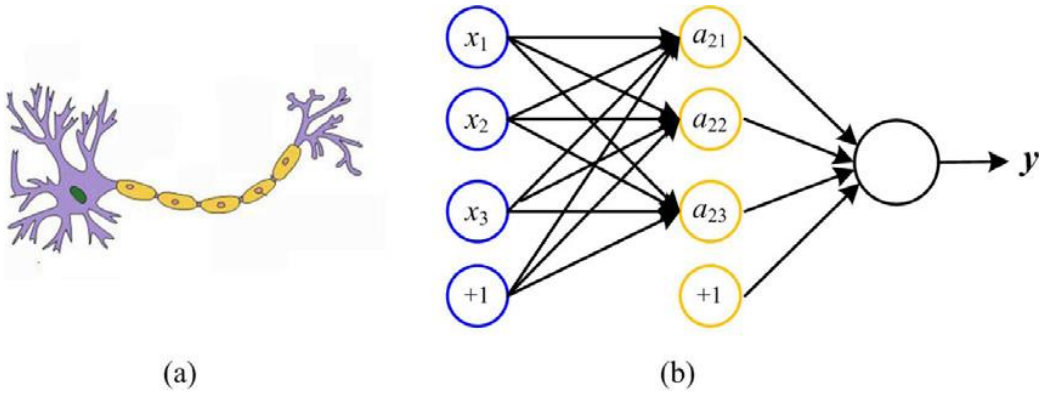

Figure 1.17: (a) Human simple neural network; (b) ANN with one hidden layer [33]

ANNs are principally composed of neurons, layers, weights, connections and activation function. Neurons are the basic units of an ANN, alike to the neurons in the human brain. Each neuron receives input, performs a calculation, and produces an output. Layers are divided to three types; input layer, this one receives input data and transmits it to the network. Hidden layers also called Intermediate layers, they connect the input and output layers, and they are responsible for processing data through complex transformations. Output layer, which provides the final output based on the processed information from the hidden layers. Thus; these layers are related to each other by connections. Those last are between neurons and assigned weights, which represent the strength of the connection. These weights are adjusted during the learning process, impacting the network's behavior. Activation function are used to introduce nonlinearities into the system, enabling the network to learn complex patterns and relationships in data, there are multiple activation function that are used in ANN such as linear transfer function (purelin), sigmoid, hyperbolic tangent (tanh), and rectified linear unit (ReLU) etc… The area of ANNs is diverse and fascinating, offering a variety of tools for tackling different problems. [46]. Here is a slight opening into some popular types:

1.4.1.6.1 Multi Layer Perceptron

A MLP is a type of neural network with one or more hidden layers between the input and output layers. MLPs are also referred to as fully connected networks because each neuron in a layer is connected to every neuron in the subsequent layer. The architecture of an MLP is characterized by its ability to learn complex, nonlinear relationships in data (figure 1.18) [46].

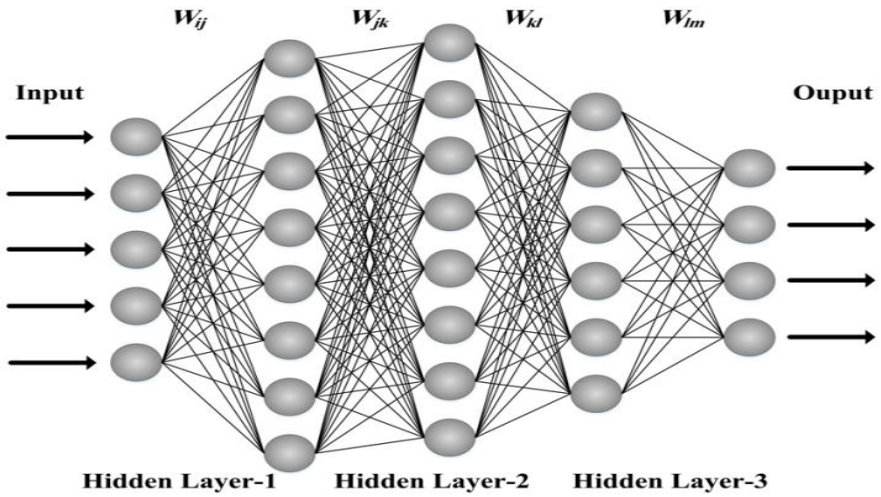

Figure 1.18: MLP architecture

1.4.1.6.2. Feed Forward Neural Network

A feed forward neural network (FFNN) is a type of ANNs that processes information in a forward direction, from the input layer to the output layer, without any feedback connections (figure 1.19). It follows a straightforward architecture where the outputs from one layer serve as inputs to the next layer. FFNNs are also known as MLPs when they have multiple hidden layers [46]. Activation functions are mathematical functions applied to the outputs of neurons in neural networks. They introduce nonlinearity into the network, enabling it to learn complex patterns in the data. Commonly used activation functions in FFNNs include the sigmoid function, tanh function, purelin, and rectified linear unit (ReLU) function. These functions transform the input values to a desired range, facilitating effective learning and prediction within the network. The general equations of a FFNN are:

- Hidden layer equations:

$$\begin{cases} k = \sum w_i x_i + b_i \\ p_j(k) = \frac{1}{1+e^{-k}} \end{cases} \quad (1.1)$$

- Output layer equations

$$\begin{cases} y = \sum w'_j p_j + b' \\ p_y(y) = Y \end{cases} \quad (1.2)$$

Where: w is the weight, b is the bias.

.

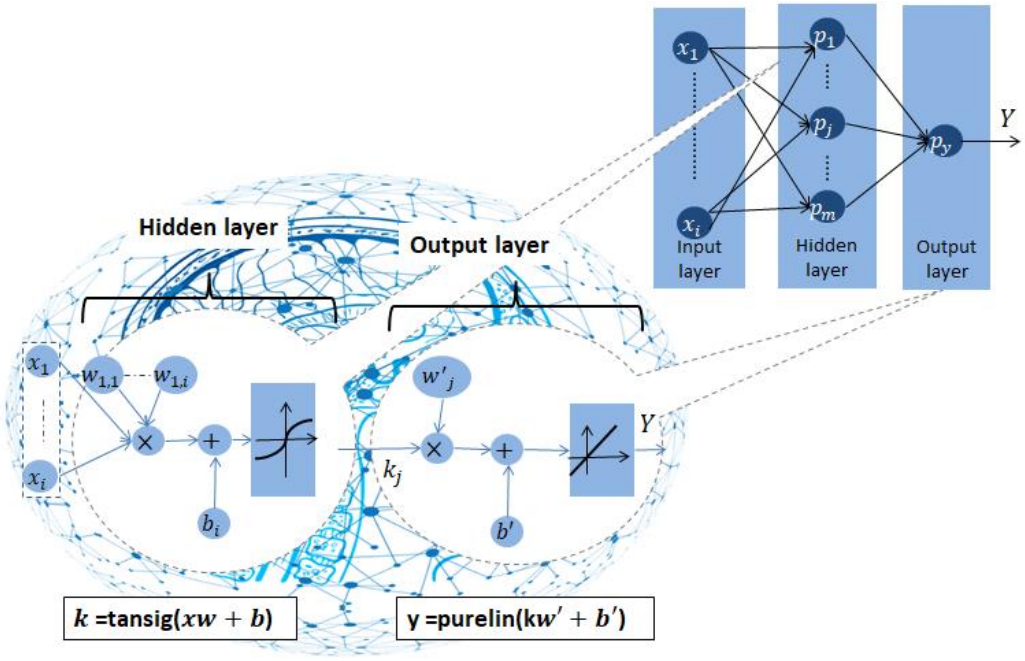

Figure 1.19: FFNN configuration for one hidden layer.

1.4.1.6.3. Radial Basis Neural Network

Radial Basis Neural Network (RBNN) is a type of ANNs that uses radial basis functions as activation functions. Unlike traditional FFNNs with sigmoid or hyperbolic tangent activation functions, RBNNs have a unique architecture and are often employed for specific types of tasks offering advantages in classification of nonlinear data due to its simple structure and swift convergence. Similar to classical neural networks, the RBF network comprises three layers; an input layer, a hidden layer with radial basis functions, and an output layer each layer serving a distinct function. Figure 1.20 illustrates the current neural network configuration according to its respective functions. In greater detail, the first layer represents the input layer, where the number of nodes corresponds to the dimensions of the input data. The third layer constitutes the output layer, with the number of nodes matching the size of the output data. Notably, this layer maps nonlinearity through a linear combiner within a novel space. Situated between them, the intermediate layer, known as the hidden layer, introduces nonlinearity. Each node in this layer is purposefully identified and characterized through a radial basis function. The most commonly used radial basis function is the Gaussian function. [46].

The radial basis function process involves estimating each data point within the input vectors. The training data, collected from the current network, are compared to the input values to generate similar data. Each similarity value is then multiplied by weights in

the hidden layer, and the resulting summation is displayed in the output layer. For any new input data, the network can be easily calculated by measuring the Euclidean distance between the input and training data. In such cases, it's crucial to determine the center and the spread σ of nodes originating from the intermediate layer, along with the weight matrix positioned between the hidden layer and the output layer. To determine the center of node in hidden layer, cluster method is the best to ensure the procedure. This method to be done in sequence manner in order to divide data points into diverse categories. The activation function is typically represented as a Gaussian function (Equation 3).

$$\varphi_j(x) = e^{-\frac{\|x-c_j\|}{{\sigma_j}^2}} \tag{1.3}$$

Where x represents the input parameters; c_j and σ_j are center and spread of the ith RBF node, respectively. The spread can be calculated by Equation 4 as:

$$\sigma_j = \frac{d_{max}}{\sqrt{2n}} \tag{1.4}$$

Where n is the number of the node in the intermediate layer, d_{max} is the maximum distance between the cluster centers selected.

Finally, the outputs of the non-linear activation function $\varphi_j(x)$ are integrated linearly with the weight vector ω_j of the output layer to produce the output network class as presented in equation follows:

$$class\ m = \sum_{j=0}^{n} \varphi_j \omega_j \tag{1.5}$$

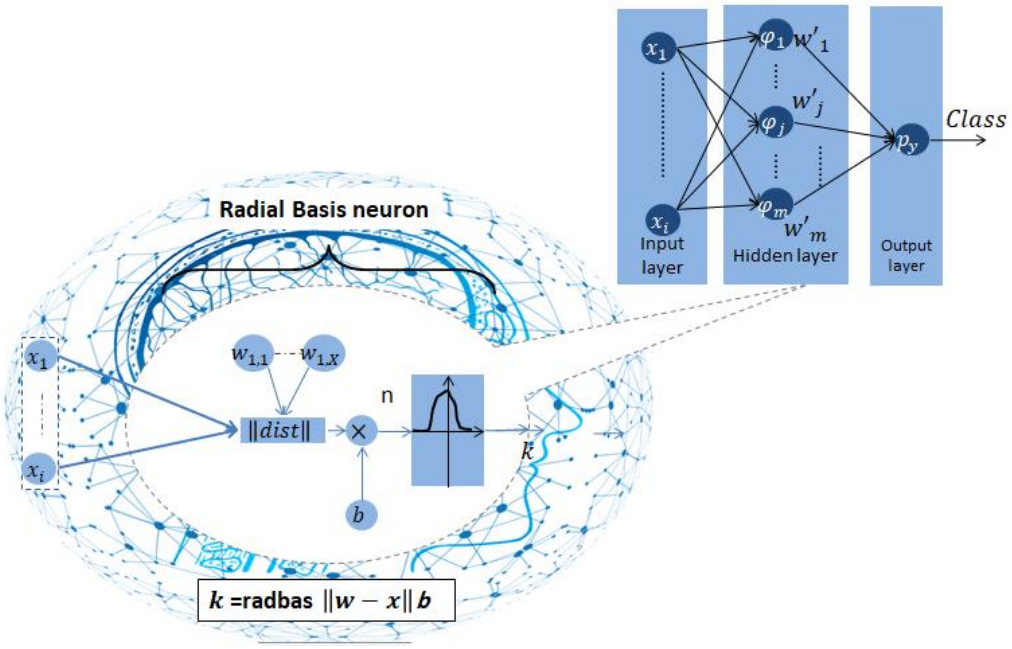

Figure 1.20: RBNN configuration

Two types of radial basis function neural network are used in this study, and they are presented below:

- ✓ The basic Radial Basis neural network

This type of neural network is implemented by the "*newrb*" function. It iteratively constructs a radial basis network, adding one neuron at a time. The spread parameter determines the width of the Gaussian function associated with each neuron. [47].

- A larger spread results in a smoother function approximation.
- However, if the spread is too large, it may require many neurons to fit a fast-changing function.
- Conversely, if the spread is too small, it may require numerous neurons to fit a smooth function, and the network may struggle to generalize well.

Therefore, calling "*newrb*" with different spreads is necessary to find the optimal value for a given problem, balancing between smoothness and complexity for effective function approximation. [47].

- ✓ Radial basis extended neural network (RBENN)

This type of neural network is implemented by the "*newrbe*" function. It rapidly constructs a radial basis function network that achieves zero error on the training vector.

It's important to note that the spread parameter should not be too large, as this would cause each neuron to effectively respond in the same, broad area of the input space [47].

1.4.1.6.4. Generalized Regression Neural Network

Generalized regression neural network (GRNN) contain four layers, input layer, pattern layer, summation layer and output layer [46]. Figure 1.21 illustrates the architecture of a GRNN. The role of the input layer is just like any other ANN, responsible to receive data; the pattern layer equation is given by:

$$F_k(x,y) = \frac{1}{(2\pi\sigma^2)^{M/2}} \frac{1}{n} \sum_{j=1}^{n} e^{-dx/2\sigma^2} . e^{-dy/2\sigma^2} \quad (1.6)$$

Where $d_x = (x_j - x)^T (x_j - x)$, $d_y = (y_j - y)$.

n is the number of simple observations; M is the size of the variable x_j ; σ is the smoothing parameter; x is the independent data in the input layer; x_i is the observed input; y is the output coming from a specific input vector x; y_i is the desired output coming from the observed input x_i.

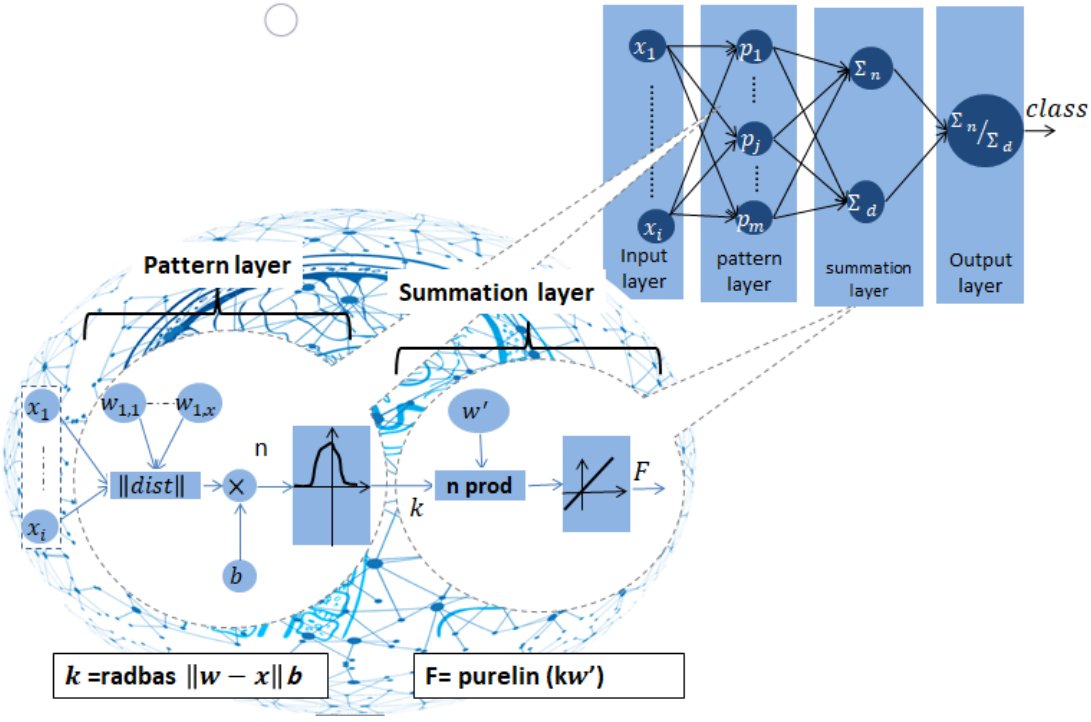

Figure 1.21: GRNN configuration.

The regression given by GRNN is the most possible y provided from a specific input vector x. Thus; the summation layer has two type of processing neuron, numerator

neuron (N) and denominator neuron (D). There equations are defined by equations (7) and (8) successively. In the end, the neuron of the output layer is defined as the division of the numerator by the denominator (equation 9) and it represents the output.

$$N = \sum_{j=1}^{n} y_j e^{-dx/2\sigma^2} \tag{1.7}$$

$$D = \sum_{j=1}^{n} e^{-dx/2\sigma^2} \tag{1.8}$$

$$\hat{C} = N/D \tag{1.9}$$

1.4.1.6.5. Artificial neural network in fault diagnosis of induction motors

ANNs exceled in wide areas such as image and speech recognition, natural language processing, financial forecasting, healthcare diagnostics, and predictive maintenance. As well as in IM fault detection and identification by given classification of the fault introduced and estimating its severity. Lazar et al. [48] propose A FF-MLP-NN trained by back propagation algorithm for fault detection and localization of SITSC fault in the three phases. The detection process is based on monitoring the three-phase instantaneous power average using the stator currents and voltages, the experimental investigation demonstrate the effectiveness of the proposed method. As well as lashkari et al. [49], a FF-MLP-NN was used to locate SITSC fault. The fault indicator used in this approach was the three-phase shift between line current and phase voltage of induction motors. Notably, the method also considered unbalanced supply voltage to distinguish whether the unbalance in the three currents was due to an SITSC fault or a supply voltage fault. The experimental results demonstrated a superior accuracy of the proposed method. Maraaba et al. [50] proposed the use of a MLP-NN to estimate SITSC faults by determining the percentage of shorted turns. The fault indicator selected for this purpose was electro-mechanical torque. Statistical and frequency-related features such as mean, variance, max, min, and the occurrence of frequency at 2F (F is the supply frequency) were identified as highly distinctive, enabling the correlation of captured electromechanical torque with the corresponding percentage of shorted turns. The MLP-NN was trained using data from five different motors, and its efficiency was tested on two new, previously unseen motors. The results revealed a high level of accuracy in the range of 88–99%. Unlike lazar et al. [51], who proposed the use of a MLP-NN to determine the percentage of SITSC and detect USV occurrences. Researchers utilized current and voltage signals as fault indicators. The distinct features identified for this purpose included the maximum and minimum values of total instantaneous power, the phase shift between current and voltage,

and the negative sequence voltage. The training phase involved a mathematical model of the IM, while the testing phase employed an experimental test IM. The results demonstrated a high accuracy level within the range of 95–99%. Moosavi et al. [52] proposed the utilization of a FFNN for the diagnosis and classification of various levels of SITSCs. They employed a Finite Element Method (FEM)-based approach to develop a mathematical model of the motor, aiming to identify the most effective indicators. Signal processing, specifically FFT analysis, was applied to reveal the optimal patterns. The results were validated using experimental IM, and the ANN was trained and tested using experimental data. The proposed approach demonstrated a high level of accuracy in the diagnosis process. Nayenteh et al. [53] presented information on the localization of SITSC fault and the estimation of fault severity by determining the number of short-circuited turns during the fault. They employed a cluster of Focused Time-Lagged Neural Networks (FTLNNs) trained using the Particle Swarm Optimization (PSO) algorithm. The zero-sequence current was identified as a significant feature, and the neural network cluster demonstrated satisfactory diagnostic capabilities. Asfani et al. [54] investigated SWSC fault occurrences, utilizing the Wavelet Transform (WT) for processing motor current signals. The energy level of the high-frequency signal from the wavelet transform served as the input variable for a neural network functioning as a detection system. Three types of neural networks, namely FFNN, Elman-NN, and RBFNN, were developed and assessed. The results indicated that ELMNN was the simplest and most accurate system capable of recognizing all unseen test data. Rajamani and Nabunita [55-56] established the per-unit change in negative sequence current with positive sequence current as the primary fault indicator, integrated into the architecture of a Feed forward Neural Network (FFNN). The output of the FFNN effectively classified the SWSC fault level.

1.4.2. Deep learning methods

Deep learning (DL), a subset of machine learning, employs artificial neural networks with multiple layers, commonly known as deep neural networks (DNNs), to address intricate tasks. The term "deep" reflects the utilization of multiple hidden layers within these networks. DNNs undergo training using an optimization technique known as backpropagation. Throughout the training process, the network refines its internal parameters, including weights and biases, based on the disparity between predicted and actual outcomes. This iterative adjustment enhances the network's proficiency in making accurate predictions. Non-linear activation functions, such as ReLU (Rectified Linear Unit)

and sigmoid play a crucial role in DNNs. The domain of deep learning is diverse and captivating, offering a spectrum of tools to tackle various problems [57]. Here, we highlight two of the most popular types:

1.4.2.1. Convolutional Neural Networks

Convolutional neural networks (CNNs) are specialized deep neural networks designed for processing grid-like data. They are characterized by two types of layers: convolutional layers and pooling layers. The convolutional layers utilize filters to extract local patterns and spatial hierarchies, allowing the network to recognize complex visual structures. The pooling layers down-sample the spatial dimensions, reducing computational complexity, and providing translation invariance. In addition, the fully connected layers and the softmax layer are usually added as the top layers to make predictions. To give a clear illustration, the framework for a one-layer CNN is displayed in (figure 1.22). CNNs have demonstrated remarkable success in image recognition, object detection, and various computer vision tasks, leveraging their capacity to capture local patterns and spatial relationships in visual data. Moreover, they have proven (effective) effectiveness in fault diagnosis of induction motors [57].

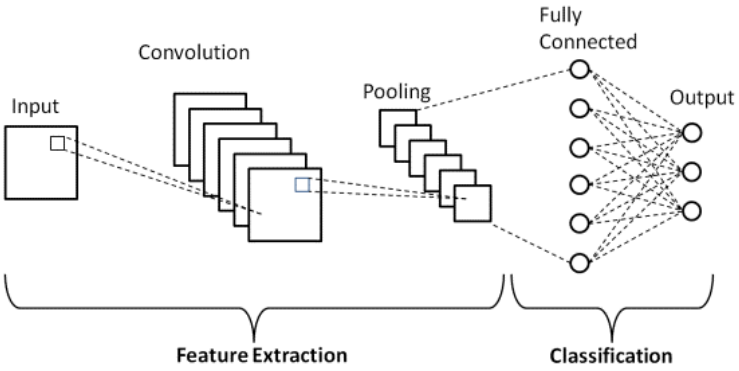

Figure 1.22: Illustrations for one-layer CNN that contains one convolutional layer, one pooling layer, one fully connected layer and a softmax layer. [58]

Janssens et al. [59] employed a 2D-CNN model to recognize four categories of rotating machinery conditions. The model's input consisted of Discrete Fourier Transform (DFT) results derived from two accelerometer signals collected by two sensors positioned perpendicular to each other. Consequently, the input height corresponds to the number of sensors. The CNN architecture used comprised one convolutional layer and one fully connected layer. Classification was performed using the top softmax layer. Liu et al.

introduced a Dislocated Time Series (DTS) CNN for the fault diagnosis of IM's rotor faults [60]. In their approach, a dislocated time series layer was incorporated to shift the 1D input mechanical signal into an output matrix. The Dislocated Time Series (DTS) operation involved arranging several intercepted signals from the original signal to form this matrix. Subsequently, a conventional deep CNN model was applied for further analysis.

1.4.2.2. Recurrent Neural Networks

Recurrent neural networks (RNNs) are specifically designed for handling sequential data, rendering them suitable for tasks involving time series analysis. In contrast to traditional FFNN, RNNs feature cyclic connections, allowing information to persist and circulate through the network in a loop (figure 1.23). The inherent ability of RNNs to capture temporal dependencies in data makes them well-suited for tasks where the order of inputs is essential. This characteristic enables RNNs to learn and remember information over extended sequences, addressing challenges associated with long-term dependencies. RNNs find applications in diverse fields, including speech recognition, language modeling, and notably fault recognition in IMs [57].

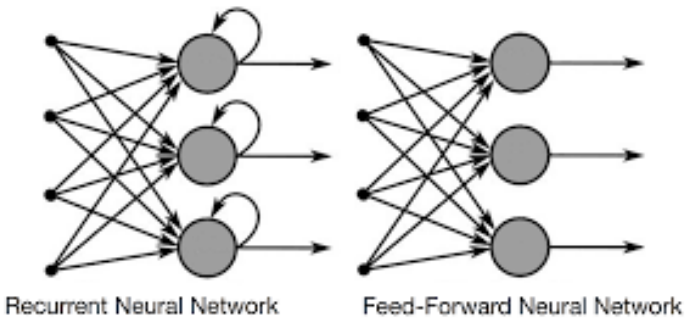

Figure 1.23: Recurrent neural network and Feed forward neural network architectures [58].

Zhao et al. introduced a hybrid approach that integrates handcrafted feature design with automatic feature learning for machine health monitoring [61]. Features were extracted from input time series and inputted into an enhanced bidirectional RNN, which comprises two modules: bidirectional and weighted feature averaging. The efficacy of their proposed model was demonstrated in three machine health monitoring tasks—tool wear prediction, gearbox fault diagnosis, and incipient bearing fault detection. The hybrid

approach show effectiveness in recognizing faults in IMs. In [62], Malhotra proposed an intriguing structure for bearing prediction. They devised an RNN-based encoder-decoder architecture, where the RNN encoder transformed a multivariate input sequence into a fixed-length vector. Subsequently, the decoder utilized these vectors to generate the target sequence. For prediction, they assumed that the model could initially be trained on raw signals corresponding to normal behavior in an unsupervised manner. The reconstruction error was then employed to compute a health index, subsequently used for estimating the remaining useful life of the bearing. It's noteworthy that a larger reconstruction error intuitively corresponds to an unhealthy machine condition.

1.5. Conclusion

The condition monitoring of motors plays a critical role in ensuring the uninterrupted functioning of machines. The meticulous selection of protective devices not only enhances the detection of anomalies but also expedites the restart process.

Consequently, diagnosing electrical machines has been, and continues to be, a profoundly significant research focus spanning several decades, as discussed in this chapter. The introduction of monitoring has brought about a revolutionary shift in the maintenance of systems reliant on electrical machines. Essentially, this term denotes the systematic monitoring of a system to diagnose the condition of an alternating current motor, discerning various faults and assessing their severity under normal operating conditions.

Throughout this chapter, our objective has been to compile comprehensive information regarding the symptoms that an IM may exhibit. Furthermore, we provide extensive details on diagnostic methods to facilitate a thorough understanding of the diagnostic processes.

Chapter (2)
Modeling of Induction Motors with SITSC fault

2.1 Introduction

In this chapter, we will take on the first part the modeling of the asymmetric induction machine. In this modeling, we assume that the number of turns for each stator phase is different. This assumption does not change the fact that the machine is healthy, but the choice of the number of turns in the construction of the machine is different.

Then, we will revisit the modeling of the IM but in the case of SITC fault. This takes into account short-circuit faults on the three stator phases. In practice, this fault can be due to damaged insulation (varnish or enamel) on the copper wires. We represent such a situation with an additional circuit connecting a part of the faulty phase to the neutral point.

Finally, we will address the simulation of the two models of the machine. The simulation is performed in the Matlab/Simulink environment, which provides the opportunity to analyze the machine's behavior under various conditions of asymmetry and faults.

2.2. Park's Transform

Park's transform involves transforming the original IM phase windings *a, b, c* into windings arranged along two axes called *d* and *q*, presenting electrical and magnetic equivalence. This transformation facilitates the transference from the *abc* reference frame to the *αβ* reference frame, which remains fixed relative to the *abc* frame, or to the *dq* frame, which is movable. A transformation matrix is established for currents, voltages, and flux.

$$P_a = \sqrt{\frac{2}{3}}\begin{bmatrix} \cos(\theta_a) & \cos(\theta_a - \frac{2\pi}{3}) & \cos(\theta_a + \frac{2\pi}{3}) \\ -\sin(\theta_a) & -\sin(\theta_a - \frac{2\pi}{3}) & -\sin(\theta_a + \frac{2\pi}{3}) \\ 1/\sqrt{2} & 1/\sqrt{2} & 1/\sqrt{2} \end{bmatrix} \quad (2.1)$$

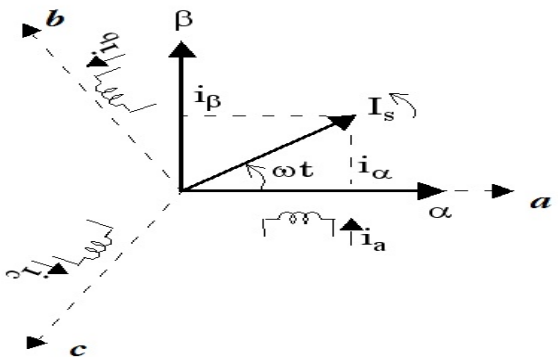

Figure 2.1: From *abc* reference frame to *αβ* reference frame.

Thus, the coefficient $\sqrt{\frac{2}{3}}$ is related to the change of basis, and the power is conserved during this transformation. The change of variables concerning currents, voltages, and flux is defined in the two-phase system by the direct Park transformation as follows:

$$X_{dq0} = P_a X_{abc} \tag{2.2}$$

$$X_{abc} = {P_a}^{-1} X_{dq0} \tag{2.3}$$

The inverse transformation matrix ${P_a}^{-1}$ is given by:

$$ {P_a}^{-1} = P_a^T \tag{2.4}$$

- Note: «a» can represent a statoric quantity «s» or a rotoric quantity «r»

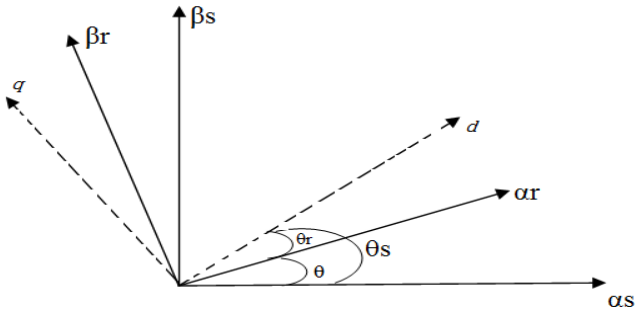

Figure 2.2: The representation of IM's axes in *dq* reference frame

2.2.1. Reference frame choice (*d*,*q*)

What makes the Park transformation appealing is that the orientation of the *dq* frame can be arbitrary. There are three important choices; the *dq* frame can be fixed to the stator, to the rotor, or to the rotating field, depending on the application's objective [27].

- *d,q* axes frame linked to the stator or stationary frame (θ_s= 0). Electrical quantities evolve in a steady-state electrical regime at the stator pulsation ω_s. This choice is often adopted in observer studies [27].
- *d,q* axes frame linked to the rotor (θ_r= 0). Electrical quantities evolve in a steady-state electrical regime at the rotor current pulsation ω_r. They have a low frequency (slip frequency) [27].
- *d,q* axes frame linked to one of the machine's fluxes. The model is simplified by using simpler equations. In a steady-state electrical regime, the model quantities are continuous. This method is frequently employed in control studies [27].

2.2.2. Stator-linked reference frame (Stationary Frame α β)

This transformation is also called the Clarke transformation, which is, in fact, a specific case of the Park transformation. It is obtained when the d,q frame coincides with the $\alpha\beta$ frame, i.e., by setting (θ_s= 0). This choice is often made for the diagnosis of electrical machines and also for the simplicity of calculations.

The Park matrices for a stator-linked reference frame (θ_s= 0) are as follows:

$$P_s = \sqrt{\frac{2}{3}}\begin{bmatrix} 1 & -1/2 & -1/2 \\ 0 & \sqrt{3}/2 & -\sqrt{3}/2 \\ 1/\sqrt{2} & 1/\sqrt{2} & 1/\sqrt{2} \end{bmatrix} \quad (2.5)$$

2.2.3. Simplifying assumptions

The modeling of the IM is based on a set of simplifying assumptions [2], which are:

- Magnetic circuits are asymmetrical.
- The distribution of induction in the air gap is sinusoidal.
- The air gap is constant.
- Phenomena of saturation are neglected, allowing the magnetic flux to be considered as a linear function of currents.
- The influence of skin effect and heating on characteristics is not taken into account.

Among the important consequences of these assumptions, we can mention:

- The flux is additive.
- Constancy of the proper inductances.
- Sinusoidal variation law of mutual inductances between stator and rotor windings based on the electrical angle between their magnetic axes.

2.3 Asymmetrical Induction Motor modeling

In the three-phase reference frame, the three vectors a_s, $b_s$and $c_s$are aligned with the axes of the three stator windings of the machine. The same applies to the rotor. The axis α_s is often taken as the reference, and the angle θ defines the rotor position relative to the stator. See Figure 2.2.

Considering f_a, f_b, and f_c as the ratios of the number of turns subtracted from the total number of turns with:

$$f_a = \frac{n_a}{N_s} \quad , \quad f_b = \frac{n_b}{N_s} \quad , \quad f_c = \frac{n_c}{N_s}$$

Such that: n_a,n_b and $n_c$are the numbers of turns subtracted for each phase.

2.3.1. Electric equations

Taking into account the assumptions mentioned earlier, the electrical equations for stator and rotor voltages can be written as follows:

$$\begin{cases} V_{abc}^s = R_{abc}^s i_{abc}^s + \dfrac{d}{dt}\Phi_{abc}^s \\ 0 = R_{abc}^r i_{abc}^r + \dfrac{d}{dt}\Phi_{abc}^r \end{cases} \tag{2.6}$$

The quantities V_{abc}^s, i_{abc}^s , Φ_{abc}^s are 3x1 dimension vectors defined as follows:

$$V_{abc}^s = \begin{bmatrix} V_a^s \\ V_b^s \\ V_c^s \end{bmatrix} \qquad i_{abc}^s = \begin{bmatrix} i_a^s \\ i_b^s \\ i_c^s \end{bmatrix} \qquad \Phi_{abc}^s = \begin{bmatrix} \Phi_a^s \\ \Phi_b^s \\ \Phi_c^s \end{bmatrix}$$

Those of the rotor are:

$$i_{abc}^r = \begin{bmatrix} i_a^r \\ i_b^r \\ i_c^r \end{bmatrix} \qquad \Phi_{abc}^r = \begin{bmatrix} \Phi_a^r \\ \Phi_b^r \\ \Phi_c^r \end{bmatrix}$$

The matrices of the resistances of the stator and rotor windings are defined as follows:

$R_{abc}^s = \begin{bmatrix} r_{as} & 0 & 0 \\ 0 & r_{bs} & 0 \\ 0 & 0 & r_{cs} \end{bmatrix}$: Matrix of resistances of the stator.

With:

$$\begin{cases} r_{as=r_s(1-f_a)} \\ r_{bs=r_s(1-f_b)} \\ r_{cs=r_s(1-f_c)} \end{cases} \tag{2.7}$$

For $r_{as} = r_{bs} = r_{cs} = r_s$ the IM becomes symmetric.

$R^r_{abc} = \begin{bmatrix} r_r & 0 & 0 \\ 0 & r_r & 0 \\ 0 & 0 & r_r \end{bmatrix}$: Matrix of resistances of the rotor

r_s: Resistance of one stator phase. r_r: Resistance of one rotor phase.

By applying the Park transformation to equation (2.6), we obtain:

a. For the stator

$$\mathrm{P_s V^s_{abc}} = \mathrm{P_s}(\mathrm{R^s_{abc} i^s_{abc}} + \frac{\mathrm{d}}{\mathrm{dt}}\Phi^s_{abc}) \tag{2.8}$$

$$P_s V^s_{abc} = P_s R^s_{abc} i^s_{abc} + P_s \frac{d}{dt}\Phi^s_{abc} \tag{2.9}$$

In a (dq)-frame linked to the stator, we have:

$$P_s \frac{d}{dt}\Phi^s_{abc} \quad = \frac{d}{dt}(P_s \Phi^s_{abc}) - \left(\frac{d}{dt}P_s\right)\Phi^s_{abc} \tag{2.10}$$

et $(\frac{d}{dt}P_s)\Phi^s_{abc} = 0$ (2.11)

The matrix of stator voltages becomes:

$$P_s V^s_{abc} = P_s R^s_{abc} P_s^{-1}(P_s i^s_{abc}) + \frac{d}{dt}(P_s \Phi^s_{abc}) \tag{2.12}$$

We will arrive at the equation for stator voltages in the Park frame.

$$V^s_{dq0} = P_s R^s_{abc} P_s^{-1} i^s_{dq0} + \frac{d}{dt}\Phi^s_{dq0} \tag{2.13}$$

Let's define $R^s_{dq0} = P_s R^s_{abc} P_s^{-1}$ (2.14)

$$V^s_{dq0} = R^s_{dq0} i^s_{qd0} + \frac{d}{dt}\Phi^s_{dq0} \tag{2.15}$$

Where:

$R^s_{dq0} = \begin{bmatrix} r^s_{11} & r^s_{12} & r^s_{13} \\ r^s_{21} & r^s_{22} & r^s_{23} \\ r^s_{31} & r^s_{32} & r^s_{33} \end{bmatrix}$.The elements of the stator resistance matrix are in appendix A.

Where R^s_{dq0} is the stator resistance matrix in the Park frame.

If the machine is symmetric: $R^s_{dq0} = r_s \begin{bmatrix} 1 & 0 & 0 \\ 0 & 1 & 0 \\ 0 & 0 & 1 \end{bmatrix}$.

b. For the rotor

$$P_r = \sqrt{\frac{2}{3}}\begin{bmatrix} \cos(\theta_r) & \cos(\theta_r - \frac{2\pi}{3}) & \cos(\theta_r + \frac{2\pi}{3}) \\ -\sin(\theta_r) & -\sin(\theta_r - \frac{2\pi}{3}) & -\sin(\theta_r + \frac{2\pi}{3}) \\ 1/\sqrt{2} & 1/\sqrt{2} & 1/\sqrt{2} \end{bmatrix} \quad (2.16)$$

$$0 = P_r(R^r_{abc} i^r_{abc} + \frac{d}{dt}\Phi^r_{abc}) \quad (2.17)$$

$$0 = P_r R^r_{abc} i^r_{abc} + P_r \frac{d}{dt}\Phi^r_{abc} \quad (2.18)$$

with

$$P_r \frac{d}{dt}\Phi^r_{abc} = \frac{d}{dt}(P_r \Phi^r_{abc}) - (\frac{d}{dt}P_r)\Phi^r_{abc} \quad (2.19)$$

$$0 = P_r R^r_{abc} P_r^{-1}(P_r i^r_{abc}) + \frac{d}{dt}(P_r \Phi^r_{abc}) - (\frac{d}{dt}P_r)P_r^{-1}(P_r \Phi^r_{abc}) \quad (2.20)$$

$$0 = P_r R^r_{abc} P_r^{-1} i^r_{dq0} + \frac{d}{dt}(\Phi^r_{qd0}) - (\frac{d}{dt}P_r)P_r^{-1}\Phi^r_{qd0} \quad (2.21)$$

with

$$\left(\frac{d}{dt}P_r\right)P_r^{-1} = \omega_r \begin{bmatrix} 0 & 1 & 0 \\ -1 & 0 & 0 \\ 0 & 0 & 0 \end{bmatrix} \quad (2.22)$$

Let's define : $R^r_{dq0} = P_r R^r_{abc} P_r^{-1}$

$$R^r_{dq0} = r_r \begin{bmatrix} 1 & 0 & 0 \\ 0 & 1 & 0 \\ 0 & 0 & 1 \end{bmatrix}.$$

The rotor is symmetric $r_{ar} = r_{br} = r_{cr} = r_r$.

Where $R^r_{qd0}$is the rotor resistance matrix in the Park frame.

We arrive at the equation for rotor voltages in the Park reference frame.

$$0 = R^r_{dq0} i^r_{dq0} - \omega_r \begin{bmatrix} 0 & 1 & 0 \\ -1 & 0 & 0 \\ 0 & 0 & 0 \end{bmatrix} \Phi^r_{dq0} + \frac{d}{dt}\Phi^r_{dq0} \quad (2.23)$$

Finally, we got:

$$\begin{cases} V^s_{dq0} = R^s_{dq0} i^s_{dq0} + \frac{d}{dt}\Phi^s_{dq0} \\ 0 = R^r_{dq0} i^r_{dq0} - \omega_r \begin{bmatrix} 0 & 1 & 0 \\ -1 & 0 & 0 \\ 0 & 0 & 0 \end{bmatrix} \Phi^r_{dq0} + \frac{d}{dt}\Phi^r_{dq0} \end{cases} \quad (2.24)$$

2.3.2. Magnetic equations

The simplifying assumptions mentioned earlier lead to linear relationships between the flux and currents of the IM. These relationships are expressed as follows:

$$\begin{cases} \Phi^{s}_{abc} = L^{ss}_{abc} i^{s}_{abc} + L^{sr}_{abc} i^{r}_{abc} \\ \Phi^{r}_{abc} = L^{rs}_{abc} i^{s}_{abc} + L^{rr}_{abc} i^{r}_{abc} \end{cases} \tag{2.25}$$

L^{ss}_{abc}: Matrix of proper and mutual inductances between stator phases.

L^{rr}_{abc}: Matrix of proper and mutual inductances between rotor phases.

L^{sr}_{abc}: Matrix of mutual inductances between stator and rotor phases.

L^{rs}_{abc}: Matrix of mutual inductances between rotor and stator phases.

L_{ls}: Stator leakage inductance.

L_{lr}: Rotor leakage inductance.

L_{ms}: Stator magnetizing inductance.

To define the elements of the inductances of an asymmetric machine, it is assume that the stator phases a_s, b_s and $c_s$have turn numbers given by N_a, N_b and N_c, respectively, and that the rotor phases a_r, b_r and $c_r$have turn numbers given by $N_{ar} = N_{br} = N_{cr} = N_r$.

The elements of the stator inductance matrix are:

$$L^{ss}_{abc=} \begin{bmatrix} L_{asas} & L_{asbs} & L_{ascs} \\ L_{bsas} & L_{bsbs} & L_{bscs} \\ L_{csas} & L_{csbs} & L_{cscs} \end{bmatrix}$$

$$L_{asas} = \frac{N_a^2}{N_s^2}\left(L_{ls} + \frac{2}{3}L_m\right) = N_a^2 L_{mls} \tag{2.26}$$

$$L_{bsbs} = N_b^2 L_{mls} \tag{2.27}$$

$$L_{cscs} = N_c^2 L_{mls} \tag{2.28}$$

With:

$$L_{mls} = \frac{1}{N_s^2}\left(L_{ls} + \frac{2}{3}L_m\right) \tag{2.29}$$

$$L_{ms} = \frac{2}{3}L_m \tag{2.30}$$

And

$$\begin{cases} N_{a=} N_s(1 - f_a), & f_a = \dfrac{n_a}{N_s} \\ N_{b=} N_s(1 - f_b), & f_b = \dfrac{n_b}{N_s} \\ N_{c=} N_s(1 - f_c), & f_c = \dfrac{n_c}{N_s} \end{cases} \tag{2.31}$$

The stator mutual inductances:

$$L_{asbs} = L_{bsas} = \left(-\frac{1}{2}N_aN_b\right)\left(\frac{2}{3}\frac{L_m}{N_s^2}\right) = -\frac{1}{3}\frac{N_aN_b}{N_s^2}L_m = N_aN_bL_{mss} \quad (2.32)$$

$$L_{ascs} = L_{csas} = \left(-\frac{1}{2}N_aN_c\right)\left(\frac{2}{3}\frac{L_m}{N_s^2}\right) = -\frac{1}{3}\frac{N_aN_c}{N_s^2}L_m = N_aN_cL_{mss} \quad (2.33)$$

$$L_{bscs} = L_{csbs} = N_bN_cL_{mss} \quad (2.34)$$

with $L_{mss} = -\frac{1}{3}\frac{L_m}{N_s^2}$ (2.35)

If the stator is symmetrical, the proper inductances of phases a_s , b_s and $c_s$are equal:

$$L_{asas} = L_{bsbs} = L_{cscs} = L_{ls} + \frac{2}{3}L_m = L_{ls} + L_{ms} \quad (2.36)$$

For the same reason, the mutual inductances of the stator are also equal.

$$L_{asbs} = L_{ascs} = L_{bsas} = L_{bscs} = L_{csas} = L_{csbs} = -\frac{1}{2}L_{ms} \quad (2.37)$$

Consequently, the matrices of inductances are expressed as:

$$L_{abc}^{ss} = \begin{bmatrix} f_a^2(L_{ls}+L_{ms}) & -\frac{L_{ms}}{2}f_af_b & -\frac{L_{ms}}{2}f_af_c \\ -\frac{L_{ms}}{2}f_af_b & f_b^2(L_{ls}+L_{ms}) & -\frac{L_{ms}}{2}f_bf_c \\ -\frac{L_{ms}}{2}f_af_c & -\frac{L_{ms}}{2}f_bf_c & f_c^2(L_{ls}+L_{ms}) \end{bmatrix}$$

And

$$L_{abc}^{sr} = L_{sr}\begin{bmatrix} cos(\theta) & cos\left(\theta+\frac{2\pi}{3}\right) & cos\left(\theta-\frac{2\pi}{3}\right) \\ cos\left(\theta-\frac{2\pi}{3}\right) & cos(\theta) & cos\left(\theta+\frac{2\pi}{3}\right) \\ cos\left(\theta+\frac{2\pi}{3}\right) & cos\left(\theta-\frac{2\pi}{3}\right) & cos(\theta) \end{bmatrix}$$

L_{sr} : Maximum of the mutual inductance between one stator phase and one rotor phase.

The rotor is assumed symmetrical, the proper inductances of phases a_r , b_r and $c_r$are equal.

$$L_{arar} = L_{brbr} = L_{crcr} = L_{lr} + \frac{2}{3}L_m = L_{lr} + L_{mr} \quad (2.38)$$

For the same reason, the mutual inductances of the rotor are equal.

$$L_{arbr} = L_{arcr} = L_{brar} = L_{brcr} = L_{crar} = L_{crbr} = -\frac{1}{2}L_{mr} \quad (2.39)$$

Avec $L_{mr} = \frac{2}{3}L_m$ (2.40)

The matrix of mutual inductances between stator and rotor phases depends on the angular position θ (stator-rotor). It is written as:

$$L_{abc}^{sr} = \begin{bmatrix} L_{asar}\cos\theta & L_{asbr}\cos(\theta + \frac{2\pi}{3}) & L_{ascr}\cos(\theta - \frac{2\pi}{3}) \\ L_{bsar}\cos(\theta - \frac{2\pi}{3}) & L_{bsbr}\cos\theta & L_{bscr}\cos(\theta + \frac{2\pi}{3}) \\ L_{csar}\cos(\theta + \frac{2\pi}{3}) & L_{csbr}\cos(\theta - \frac{2\pi}{3}) & L_{cscr}\cos\theta \end{bmatrix}$$

$$L_{abc}^{rs} = L_{abc}^{sr^T} \tag{2.41}$$

The coefficients L_{asar} ,L_{asbr}, L_{ascr}, L_{bsar},L_{bsbr},L_{bscr} ,L_{csar}, L_{csbr} and L_{cscr} are the peak values of the stator-rotor mutual inductances.

The elements of the matrix of mutual inductances between stator and rotor are [29]:

$$L_{asar} = L_{asbr} = L_{ascr} = \frac{N_a N_r}{N_s^2}\left(\frac{2}{3}L_m\right) = N_a L_{msr} \tag{2.42}$$

$$L_{bsar} = L_{bsbr} = L_{bscr} = \frac{N_b N_r}{N_s^2}(\frac{2}{3}L_m) = N_b L_{msr} \tag{2.43}$$

$$L_{csar} = L_{crbr} = L_{cscr} = \frac{N_c N_r}{N_s^2}\left(\frac{2}{3}L_m\right) = N_c L_{msr} \tag{2.44}$$

$$L_{msr} = \frac{2}{3}\frac{N_r}{N_s^2}L_m \tag{2.45}$$

The stator and rotor Park fluxes are obtained by applying the Park transformation to equation (2.25).

a. For the stator

$$P_s \Phi_{abc}^s = P_s(L_{abc}^{ss} i_{abc}^s + L_{abc}^{sr} i_{abc}^r) \tag{2.46}$$

$$\Phi_{dq0}^s = P_s L_{abc}^{ss} P_s^{-1}(P_s i_{abc}^s) + P_s L_{abc}^{sr} P_r^{-1}(P_r i_{abc}^r) \tag{2.47}$$

We arrive at the equation for stator fluxes in the Park reference frame.

$$\Phi_{dq0}^s = P_s L_{abc}^{ss} P_s^{-1} i_{dq0}^s + P_s L_{abc}^{sr} P_r^{-1} i_{dq0}^r \tag{2.48}$$

We define L_{dq0}^{ss} and L_{dq0}^{sr}as:

$$L_{dq0}^{ss} = P_s L_{abc}^{ss} P_s^{-1} \tag{2.49}$$

$$L_{dq0}^{sr} = P_s L_{abc}^{sr} P_r^{-1} \tag{2.50}$$

$$\Phi_{dq0}^s = L_{dq0}^{ss} i_{qd0}^s + L_{dq0}^{sr} i_{dq0}^r \tag{2.51}$$

$$L_{dq0}^{ss} = \begin{bmatrix} L_{11}^{ss} & L_{12}^{ss} & L_{13}^{ss} \\ L_{21}^{ss} & L_{22}^{ss} & L_{23}^{ss} \\ L_{31}^{ss} & L_{32}^{ss} & L_{33}^{ss} \end{bmatrix}$$

The elements of the matrix of proper and mutual inductances between stator phases in the Park frame are in appendix A.

If $N_a = N_b = N_c = N_s$

Thus: $L_{dq0}^{ss} = \begin{bmatrix} L_{ls} + \frac{3}{2}L_{ms} & 0 & 0 \\ 0 & L_{ls} + \frac{3}{2}L_{ms} & 0 \\ 0 & 0 & L_{ls} \end{bmatrix}$

L_{dq0}^{sr} : Matrix of mutual inductances between stator and rotor phases in the Park reference frame.

$$L_{dq0}^{sr} = \begin{bmatrix} L_{11}^{sr} & L_{12}^{sr} & 0 \\ L_{21}^{sr} & L_{22}^{sr} & 0 \\ L_{31}^{sr} & L_{32}^{sr} & 0 \end{bmatrix}$$

The elements of the matrix of mutual inductances between stator and rotor in the Park frame are in the appendix A.

b. For the rotor

$$P_r \Phi_{abc}^r = P_r (L_{abc}^{rs} i_{abc}^s + L_{abc}^{rr} i_{abc}^r) \quad (2.52)$$

$$\Phi_{dq0}^r = P_r L_{abc}^{rs} P_s^{-1} (P_s i_{abc}^s) + P_r L_{abc}^{rr} P_r^{-1} (P_r i_{abc}^r) \quad (2.53)$$

We arrive at the equation for rotor fluxes in the Park reference frame.

$$\Phi_{dq0}^r = P_r L_{abc}^{rs} P_s^{-1} i_{dq0}^s + P_r L_{abc}^{rr} P_r^{-1} i_{dq0}^r \quad (2.54)$$

We define L_{dq0}^{rs} and L_{dq0}^{rr} as:

$$L_{dq0}^{rs} = P_r L_{abc}^{rs} P_s^{-1} \quad (2.55)$$

$$L_{dq0}^{rr} = P_r L_{abc}^{rr} P_r^{-1} \quad (2.56)$$

$$\Phi_{dq0}^r = L_{dq0}^{rs} i_{dq0}^s + L_{dq0}^{rr} i_{dq0}^r \quad (2.57)$$

L_{dq0}^{rr}: Matrix of proper and mutual inductances between rotor phases in the Park reference frame.

$$L_{dq0}^{rr} = \begin{bmatrix} L_{lr} + \frac{3}{2}L_{mr} & 0 & 0 \\ 0 & L_{lr} + \frac{3}{2}L_{mr} & 0 \\ 0 & 0 & L_{lr} \end{bmatrix} \qquad L_{dq0}^{rs} = \begin{bmatrix} L_{11}^{sr} & L_{21}^{sr} & L_{31}^{sr} \\ L_{12}^{sr} & L_{22}^{sr} & L_{32}^{sr} \\ 0 & 0 & 0 \end{bmatrix}$$

The elements of the matrix of mutual inductances between rotor and stator in the Park frame are in the appendix A.

Finally, we obtain:

$$\begin{cases} \Phi^s_{dq0} = L^{ss}_{dq0} i^s_{dq0} + L^{sr}_{dq0} i^r_{dq0} \\ \Phi^r_{dq0} = L^{rs}_{dq0} i^s_{dq0} + L^{rr}_{dq0} i^r_{dq0} \end{cases} \quad (2.58)$$

2.3.3 Mechanic equations

The study of the dynamic characteristics of the IM introduces variations not only in electrical quantities (voltage, current, flux), but also in mechanical quantities (torque, speed).

$$J\frac{d}{dt}\Omega = C_e - C_r - f_v\Omega \quad (2.59)$$

With

$$\Omega = \frac{\omega}{P} \quad (2.60)$$

C_e: Electromagnetic torque.

C_r: Resisting torque imposed by the mechanical load.

f_v : Viscous friction torque.

Ω: Rotation speed.

J: Moment of inertia.

P: Number of pole pairs.

The electromechanical torque is represented in the following equation [29]:

$$Ce = P[i^s_{abc}]^T [\frac{d}{d\theta} L^{sr}_{abc}]\ [i^r_{abc}] \quad (2.61)$$

We have : $i^s_{abc} = {P_s}^{-1} i^s_{dq0}$ (2.62)

With $[i^s_{abc}]^T = [{P_s}^{-1} i^s_{dq0}]^T$ (2.63)

As a result, we obtain: $[i^s_{abc}]^T = [i^s_{dq0}]^T [{P_s}^{-1}]^T$; $[{P_s}^{-1}]^T = [P_s]$

$$[\ i^r_{abc}] = [{P_r}^{-1}][i^r_{dq0}] \quad (2.64)$$

By substituting equation (2.64) into equation (2.61), we got:

$$Ce = P[i^s_{dq0}]^T [P_s][\frac{d}{d\theta} L^{sr}_{abc}][{P_r}^{-1}][i^r_{dq0}] \quad (2.65)$$

2.3.4. State space model

The equations are rearranged to develop the state space model of the asymmetric IM.

a. For the stator:

Equation (1.15) can be written in developed form as:

$$\frac{d}{dt}\begin{bmatrix}\Phi_d^s\\ \Phi_q^s\\ \Phi_0^s\end{bmatrix}=\begin{bmatrix}V_d^s & 0 & 0\\ 0 & V_q^s & 0\\ 0 & 0 & V_{0s}\end{bmatrix}-\begin{bmatrix}r_{11}^s & r_{12}^s & r_{13}^s\\ r_{21}^s & r_{22}^s & r_{23}^s\\ r_{31}^s & r_{32}^s & r_{33}^s\end{bmatrix}\begin{bmatrix}i_d^s\\ i_q^s\\ i_0^s\end{bmatrix} \quad (2.66)$$

The voltages are balanced and equal, so $V_{0s}=0$.

Since the neutral is not connected, $i_0^s=0$.

- $\frac{d}{dt}\Phi_d^s=V_d^s-r_{11}i_d^s-r_{12}i_q^s$ (2.67)
- $\frac{d}{dt}\Phi_q^s=V_q^s-r_{21}i_d^s-r_{22}i_q^s$ (2.68)

b. For the rotor:

Equation (1.23) can be written in developed form as:

$$\frac{d}{dt}\begin{bmatrix}\Phi_d^r\\ \Phi_q^r\\ \Phi_0^r\end{bmatrix}=\omega_r\begin{bmatrix}0 & 1 & 0\\ -1 & 0 & 0\\ 0 & 0 & 0\end{bmatrix}\begin{bmatrix}\Phi_d^r\\ \Phi_q^r\\ \Phi_0^r\end{bmatrix}-r_r\begin{bmatrix}1 & 0 & 0\\ 0 & 1 & 0\\ 0 & 0 & 1\end{bmatrix}\begin{bmatrix}i_d^r\\ i_q^r\\ i_0^r\end{bmatrix} \quad (2.69)$$

Since the neutral is not connected, $i_0^r=0$.

- $\frac{d}{dt}\Phi_d^r=\omega_r\Phi_q^r-r_ri_d^r$ (2.70)
- $\frac{d}{dt}\Phi_d^r=-\omega_r\Phi_d^r-r_ri_q^r$ (2.71)

The expressions for the derivatives of stator and rotor fluxes are:

$$\begin{cases}\frac{d}{dt}\Phi_d^s=V_d^s-r_{11}i_d^s-r_{12}i_q^s\\ \frac{d}{dt}\Phi_q^s=V_q^s-r_{21}i_d^s-r_{22}i_q^s\\ \frac{d}{dt}\Phi_d^r=\omega_r\Phi_q^r-r_ri_d^r\\ \frac{d}{dt}\Phi_q^r=-\omega_r\Phi_d^r-r_ri_q^r\\ J\frac{d}{dt}\Omega=C_e-C_r-f_v\Omega\end{cases} \quad (2.72)$$

From equation (2.72), we develop the state space model in terms of the fluxes of an IM:

$$\begin{bmatrix}\dot{\Phi}_d^s\\ \dot{\Phi}_q^s\\ \dot{\Phi}_d^r\\ \dot{\Phi}_q^r\end{bmatrix}=\begin{bmatrix}V_d^s & 0 & 0 & 0\\ 0 & V_q^s & 0 & 0\\ 0 & 0 & 0 & 0\\ 0 & 0 & 0 & 0\end{bmatrix}+\omega_r\begin{bmatrix}0 & 0 & 0 & 0\\ 0 & 0 & 0 & 0\\ 0 & 0 & 0 & 1\\ 0 & 0 & -1 & 0\end{bmatrix}.\begin{bmatrix}\Phi_d^s\\ \Phi_q^s\\ \Phi_d^r\\ \Phi_q^r\end{bmatrix}-\begin{bmatrix}r_{11}^s & r_{12}^s & 0 & 0\\ r_{21}^s & r_{22}^s & 0 & 0\\ 0 & 0 & r_r & 0\\ 0 & 0 & 0 & r_r\end{bmatrix}.\begin{bmatrix}i_d^s\\ i_q^s\\ i_d^r\\ i_q^r\end{bmatrix} \quad (2.73)$$

The currents can be expressed in terms of fluxes as follows:

$$[i]=[l^{-1}].[\Phi] \quad (2.74)$$

In a condensed manner, we can write:

$$\left[\dot{\Phi}\right] = [B][V] + \omega_r[A].[\Phi] - [R].([l^{-1}].[\Phi]) \quad (2.75)$$

The state space model of the asymmetric IM can be defined by the following system of nonlinear equations:

$$\left[\dot{\Phi}\right] = (\omega_r[A] - [R].[l^{-1}])[\Phi] + [B][V] \quad (2.76)$$

With:

$$[R] = \begin{bmatrix} r_{11}^s & r_{12}^s & 0 & 0 \\ r_{21}^s & r_{22}^s & 0 & 0 \\ 0 & 0 & r_r & 0 \\ 0 & 0 & 0 & r_r \end{bmatrix} \quad [B] = \begin{bmatrix} 1 & 0 & 0 & 0 \\ 0 & 1 & 0 & 0 \\ 0 & 0 & 0 & 0 \\ 0 & 0 & 0 & 0 \end{bmatrix}$$

$$[A] = \begin{bmatrix} 0 & 0 & 0 & 0 \\ 0 & 0 & 0 & 0 \\ 0 & 0 & 0 & 1 \\ 0 & 0 & -1 & 0 \end{bmatrix} \quad [V] = \begin{bmatrix} V_d^s \\ V_q^s \\ 0 \\ 0 \end{bmatrix} \quad [l] = \begin{bmatrix} L_{11}^{ss} & L_{12}^{ss} & L_{11}^{sr} & L_{12}^{sr} \\ L_{21}^{ss} & L_{22}^{ss} & L_{21}^{sr} & L_{22}^{sr} \\ L_{11}^{sr} & L_{21}^{sr} & L_{11}^{rr} & 0 \\ L_{12}^{sr} & L_{22}^{r} & 0 & L_{22}^{rr} \end{bmatrix}$$

2.4. Induction motor modeling under stator inter turn short circuit

In this section, we consider that the presence of a SITSC on one or more phases causes a reduction in the number of turns of the affected phase; which involve the occurrence of an unbalance.

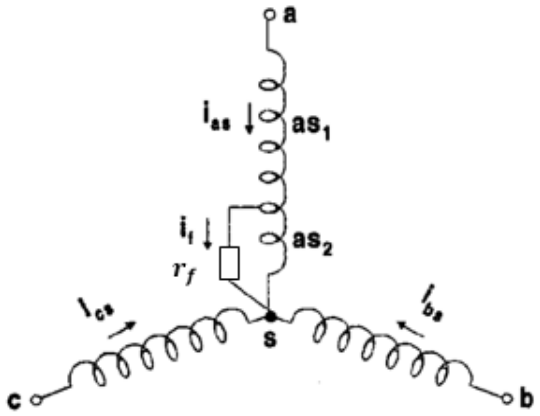

Figure 2.3: SITSC in phase a_s

This unbalance can be expressed as ratios between the number of shorted turns and the total number of turns in the each phase. These ratios are already expressed as:

$$f_a = \frac{n_a}{N_s} \quad , \quad f_b = \frac{n_b}{N_s} \quad , \quad f_c = \frac{n_c}{N_s}$$

Such that: n_a,n_b and $n_c$are the numbers of shorted turns for each phase, and N_s is the total number of turns in each phase.

2.4.1. Electric equations

The voltage equations for the three stator phases and the three rotor phases are:

$$\begin{cases} V'^{s}_{abc} = R'^{s}_{abc} i'^{s}_{abc} + \dfrac{d}{dt}\Phi'^{s}_{abc} \\ 0 = R^{r}_{abc} i^{r}_{abc} + \dfrac{d}{dt}\Phi^{r}_{abc} \end{cases} \tag{2.77}$$

The quantities V'^{s}_{abc}, i'^{s}_{abc}, Φ'^{s}_{abc} are defined as follows:

$$V'^{s}_{abc} = \begin{bmatrix} v^{s}_{a1} \\ v^{s}_{a2} \\ v^{s}_{b1} \\ v^{s}_{b1} \\ v^{s}_{c1} \\ v^{s}_{c2} \end{bmatrix} \qquad i'^{s}_{abc} = \begin{bmatrix} i^{s}_{a} \\ (i^{s}_{a} - i^{f}_{a}) \\ i^{s}_{b} \\ (i^{s}_{b} - i^{f}_{b}) \\ i^{s}_{c} \\ (i^{s}_{c} - i^{f}_{c}) \end{bmatrix} \qquad \Phi'^{s}_{abc} = \begin{bmatrix} \Phi^{s}_{a1} \\ \Phi^{s}_{a2} \\ \Phi^{s}_{b1} \\ \Phi^{s}_{b2} \\ \Phi^{s}_{c1} \\ \Phi^{s}_{c2} \end{bmatrix}$$

Those of rotor are:

$$i^{r}_{abc} = \begin{bmatrix} i^{r}_{a} \\ i^{r}_{b} \\ i^{r}_{c} \end{bmatrix} \qquad \Phi^{r}_{abc} = \begin{bmatrix} \Phi^{r}_{a} \\ \Phi^{r}_{b} \\ \Phi^{r}_{c} \end{bmatrix}$$

The matrices of resistances for stator and rotor windings are defined as follows:

$$R'^{s}_{abc} = R_s \begin{bmatrix} (1-\mathrm{f_a}) & 0 & 0 & 0 & 0 & 0 \\ 0 & \mathrm{f_a} & 0 & 0 & 0 & 0 \\ 0 & 0 & (1-\mathrm{f_b}) & 0 & 0 & 0 \\ 0 & 0 & 0 & \mathrm{f_b} & 0 & 0 \\ 0 & 0 & 0 & 0 & (1-\mathrm{f_c}) & 0 \\ 0 & 0 & 0 & 0 & 0 & \mathrm{f_c} \end{bmatrix} \qquad R^{r}_{abc} = \begin{bmatrix} r_r & 0 & 0 \\ 0 & r_r & 0 \\ 0 & 0 & r_r \end{bmatrix}$$

We rewrite the equations governing the operation of the machine and obtain:

$$\begin{cases} V^{s}_{abc} = R^{s}_{abc} i^{s}_{abc} + \dfrac{d}{dt}\Phi^{s}_{abc} - R^{s}_{abc} f_{abc} i^{f}_{abc} \\ 0 = R^{r}_{abc} i^{r}_{abc} + \dfrac{d}{dt}\Phi^{r}_{abc} \end{cases} \tag{2.78}$$

With:

$$V^{s}_{abc} = \begin{bmatrix} V^{s}_{a} \\ V^{s}_{b} \\ V^{s}_{c} \end{bmatrix} \qquad i^{s}_{abc} = \begin{bmatrix} i^{s}_{a} \\ i^{s}_{b} \\ i^{s}_{c} \end{bmatrix} \qquad \Phi^{s}_{abc} = \begin{bmatrix} \Phi^{s}_{a} \\ \Phi^{s}_{b} \\ \Phi^{s}_{c} \end{bmatrix}$$

$$R^s_{abc} = R_s \begin{bmatrix} 1 & 0 & 0 \\ 0 & 1 & 0 \\ 0 & 0 & 1 \end{bmatrix} \qquad i^f_{abc} = \begin{bmatrix} i^f_a \\ i^f_b \\ i^f_c \end{bmatrix} \qquad f_{abc} = \begin{bmatrix} f_a & 0 & 0 \\ 0 & f_b & 0 \\ 0 & 0 & f_c \end{bmatrix}$$

And:

$$V^s_{abc2}=R^s_{abc}f_{abc}i^s_{abc} +\frac{d}{dt}\Phi^s_{abc2}-R^s_{abc}f_{abc}i^f_{abc}=r_f i^f_{abc} \tag{2.79}$$

Moreover:

V^s_{abc2} : The voltage of fault.

r_f : The resistance matrix of fault.

$$r_f=\begin{bmatrix} r_{af} & 0 & 0 \\ 0 & r_{bf} & 0 \\ 0 & 0 & r_{cf} \end{bmatrix}$$

By applying the Park transformation to equation (2.78), we obtain:

For the stator:

$$P_s V^s_{abc} = P_s(R^s_{abc}i^s_{abc} + \frac{d}{dt}\Phi^s_{abc} - R^s_{abc}f_{abc}i^f_{abc}) \tag{2.80}$$

$$P_s V^s_{abc} = P_s R^s_{abc}i^s_{abc} + P_s\frac{d}{dt}\Phi^s_{abc} - P_s R^s_{abc}f_{abc}i^f_{abc} \tag{2.81}$$

In a (dq) frame linked to the stator, we have:

$$P_s\frac{d}{dt}\Phi^s_{abc} = \frac{d}{dt}(P_s\Phi^s_{abc}) - \left(\frac{d}{dt}P_s\right)\Phi^s_{abc} \tag{2.82}$$

$$(\frac{d}{dt}P_s)\Phi^s_{abc} = 0 \tag{2.83}$$

The equation for stator voltages becomes:

$$P_s V^s_{abc} = P_s R^s_{abc}P_s^{-1}(P_s i^s_{abc}) + \frac{d}{dt}(P_s\Phi^s_{abc}) - \mathrm{P_s}R^s_{abc}f_{abc}i^f_{abc} \tag{2.84}$$

We arrive at the equation for stator voltages in the Park frame.

$$V^s_{dq0} = P_s R^s_{abc}P_s^{-1}i^s_{dq0} + \frac{d}{dt}\Phi^s_{dq0} - P_s R^s_{abc}f_{abc}i^f_{abc} \tag{2.85}$$

Let's define : $R^s_{dq0\mathrm{f}} = \mathrm{P_s}R^s_{abc}f_{abc}$ (2.86)

$$V^s_{dq0} = R^s_{dq0}i^s_{qd0} + \frac{d}{dt}\Phi^s_{dq0} - R^s_{dq0\mathrm{f}}i^f_{abc} \tag{2.87}$$

With: $$R^s_{dq0f} = \begin{bmatrix} \sqrt{\frac{2}{3}}R_s f_a & -\sqrt{\frac{1}{6}}R_s f_b & -\sqrt{\frac{1}{6}}R_s f_c \\ 0 & \sqrt{\frac{1}{2}}R_s f_b & -\sqrt{\frac{1}{2}}R_s f_c \\ \sqrt{\frac{1}{3}}R_s f_a & \sqrt{\frac{1}{3}}R_s f_b & \sqrt{\frac{1}{3}}R_s f_c \end{bmatrix}$$

$$V^s_{abc2}=R^s_{abc}f_{abc}P_s^{-1}i^s_{dq0}+\frac{d}{dt}\Phi^s_{abc2}-R^s_{abc}f_{abc}i^f_{abc}=r_f i^f_{abc} \tag{2.88}$$

For the rotor:

$$0 = P_r(R^r_{abc}i^r_{abc} + \frac{d}{dt}\Phi^r_{abc}) \tag{2.89}$$

$$0 = P_r R^r_{abc}i^r_{abc} + P_r\frac{d}{dt}\Phi^r_{abc} \tag{2.90}$$

With

$$P_r\frac{d}{dt}\Phi^r_{abc} = \frac{d}{dt}(P_r\Phi^r_{abc}) - (\frac{d}{dt}P_r)\Phi^r_{abc} \tag{2.91}$$

$$0 = P_r R^r_{abc}P_r^{-1}(P_r i^r_{abc}) + \frac{d}{dt}(P_r\Phi^r_{abc}) - (\frac{d}{dt}P_r)P_r^{-1}(P_r\Phi^r_{abc}) \tag{2.92}$$

$$0 = P_r R^r_{abc}P_r^{-1}(P_r i^r_{abc}) + \frac{d}{dt}(P_r\Phi^r_{abc}) - (\frac{d}{dt}P_r)P_r^{-1}(P_r\Phi^r_{abc}) \tag{2.93}$$

with : $$\left(\frac{d}{dt}P_r\right)P_r^{-1} = \omega_r\begin{bmatrix} 0 & 1 & 0 \\ -1 & 0 & 0 \\ 0 & 0 & 0 \end{bmatrix} \tag{2.94}$$

We define: $$R^r_{dq0} = P_r R^r_{abc}P_r^{-1} \tag{2.95}$$

$$R^r_{dq0} = R_r\begin{bmatrix} 1 & 0 & 0 \\ 0 & 1 & 0 \\ 0 & 0 & 1 \end{bmatrix}$$

Where R^r_{dq0}, is the matrix of rotor resistances in the Park frame.

We arrive at the equation for rotor voltages in the Park frame.

$$0 = R^r_{dq0}i^r_{dq0} - \omega_r\begin{bmatrix} 0 & 1 & 0 \\ -1 & 0 & 0 \\ 0 & 0 & 0 \end{bmatrix}\Phi^r_{dq0} + \frac{d}{dt}\Phi^r_{dq0} \tag{2.96}$$

Finally, we obtain:

$$\begin{cases} v_{a2}^{s} = f_a R_s \left(\sqrt{\frac{2}{3}} i_d^s + \sqrt{\frac{1}{3}} i_0^s - i_f \right) + \frac{d}{dt} \Phi_{a2}^{s} = r_f i_f \\ V_{dq0}^{s} = R_{dq0}^{s} i_{qd0}^{s} + \frac{d}{dt} \Phi_{dq0}^{s} - R_{dq0\mathrm{f}}^{s} \, i_f \\ 0 = R_{dq0}^{r} i_{dq0}^{r} - \omega_r \begin{bmatrix} 0 & 1 & 0 \\ -1 & 0 & 0 \\ 0 & 0 & 0 \end{bmatrix} \Phi_{dq0}^{r} + \frac{d}{dt} \Phi_{dq0}^{r} \end{cases} \quad (2.97)$$

2.4.2. Magnetic equations

The total fluxes of the machine are related to the currents through the following equations:

$$\begin{cases} \Phi'^{s}_{abc} = L'^{ss}_{abc} i'^{s}_{abc} + L'^{sr}_{abc} i^{r}_{abc} \\ \Phi'^{r}_{abc} = L'^{rs}_{abc} i'^{s}_{abc} + L^{rr}_{abc} i^{r}_{abc} \end{cases} \quad (2.98)$$

To define the elements of the inductances of a faulty IM let's assume a short circuit at the stator phases a_s, $b_s$and c_s.

The coefficients f_a ,f_b and f_c are introduced into the various matrices.

The matrices of inductances are expressed as follows:

$$L'^{ss}_{abc} =$$

$$L_{ls} \begin{bmatrix} (1-\mathrm{f_a}) & 0 & 0 & 0 & 0 & 0 \\ 0 & \mathrm{f_a} & 0 & 0 & 0 & 0 \\ 0 & 0 & (1-\mathrm{f_b}) & 0 & 0 & 0 \\ 0 & 0 & 0 & \mathrm{f_b} & 0 & 0 \\ 0 & 0 & 0 & 0 & (1-\mathrm{f_c}) & 0 \\ 0 & 0 & 0 & 0 & 0 & \mathrm{f_c} \end{bmatrix} + L_{ms} \begin{bmatrix} \mathrm{f_{11}} & \mathrm{f_{12}} & \mathrm{f_{13}} & \mathrm{f_{14}} & \mathrm{f_{15}} & \mathrm{f_{16}} \\ \mathrm{f_{21}} & \mathrm{f_{22}} & \mathrm{f_{23}} & \mathrm{f_{24}} & \mathrm{f_{25}} & \mathrm{f_{26}} \\ \mathrm{f_{31}} & \mathrm{f_{32}} & \mathrm{f_{33}} & \mathrm{f_{34}} & \mathrm{f_{35}} & \mathrm{f_{36}} \\ \mathrm{f_{41}} & \mathrm{f_{42}} & \mathrm{f_{43}} & \mathrm{f_{44}} & \mathrm{f_{45}} & \mathrm{f_{46}} \\ \mathrm{f_{51}} & \mathrm{f_{52}} & \mathrm{f_{53}} & \mathrm{f_{54}} & \mathrm{f_{55}} & \mathrm{f_{56}} \\ \mathrm{f_{61}} & \mathrm{f_{62}} & \mathrm{f_{63}} & \mathrm{f_{64}} & \mathrm{f_{65}} & \mathrm{f_{66}} \end{bmatrix}$$

The elements of the stator magnetization inductance matrix are in the appendix B.

$$L_{abc}^{rr} = \begin{bmatrix} L_{lr} + L_{mr} & -\frac{L_{mr}}{2} & -\frac{L_{mr}}{2} \\ -\frac{L_{mr}}{2} & L_{lr} + L_{mr} & -\frac{L_{mr}}{2} \\ -\frac{L_{mr}}{2} & -\frac{L_{mr}}{2} & L_{lr} + L_{mr} \end{bmatrix}$$

$$L'^{sr}_{abc} = L_{sr}\begin{bmatrix} (1-\mathrm{f_a})\,cos(\theta) & (1-\mathrm{f_a})\,cos\left(\theta+\frac{2\pi}{3}\right) & (1-\mathrm{f_a})\,cos\left(\theta-\frac{2\pi}{3}\right) \\ \mathrm{f_a}\,cos(\theta) & \mathrm{f_a}\,cos\left(\theta+\frac{2\pi}{3}\right) & \mathrm{f_a}\,cos\left(\theta-\frac{2\pi}{3}\right) \\ (1-\mathrm{f_b})\,cos\left(\theta-\frac{2\pi}{3}\right) & (1-\mathrm{f_b})\,cos(\theta) & (1-\mathrm{f_b})\,cos\left(\theta+\frac{2\pi}{3}\right) \\ \mathrm{f_b}\,cos\left(\theta-\frac{2\pi}{3}\right) & \mathrm{f_b}\,cos(\theta) & \mathrm{f_b}\,cos\left(\theta+\frac{2\pi}{3}\right) \\ (1-\mathrm{f_c})\,cos\left(\theta+\frac{2\pi}{3}\right) & (1-\mathrm{f_c})\,cos\left(\theta-\frac{2\pi}{3}\right) & (1-\mathrm{f_c})\,cos(\theta) \\ \mathrm{f_c}\,cos\left(\theta+\frac{2\pi}{3}\right) & \mathrm{f_c}\,cos\left(\theta-\frac{2\pi}{3}\right) & \mathrm{f_c}\,cos(\theta) \end{bmatrix}$$

L_{sr} : Maximum mutual inductance between a stator phase and a rotor phase.

With the consideration of:

$$L_{sr} = \frac{2}{3}L_m \tag{2.99}$$

$$L'^{rs}_{abc} = L'^{sr\ T}_{abc} \tag{2.100}$$

We rewrite the equations governing the operation of the machine, and we obtain:

$$\begin{cases} \Phi^s_{abc2} = f_{abc}(L^{ss}_{abc}i^s_{abc} + L^{sr}_{abc}i^r_{abc} - L^f_{abc}i^f_{abc}) \\ \Phi^s_{abc} = L^{ss}_{abc}i^s_{abc} + L^{sr}_{abc}i^r_{abc} - L^{ss}_{abc}f_{abc}i^f_{abc} \\ \Phi^r_{abc} = L^{rr}_{abc}i^r_{abc} + L^{rs}_{abc}i^s_{abc} - L^{rs}_{abc}f_{abc}i^f_{abc} \end{cases} \tag{2.101}$$

With:

$$L^{ss}_{abc} = \begin{bmatrix} L_{ls}+L_{ms} & -\frac{L_{ms}}{2} & -\frac{L_{ms}}{2} \\ -\frac{L_{ms}}{2} & L_{ls}+L_{ms} & -\frac{L_{ms}}{2} \\ -\frac{L_{ms}}{2} & -\frac{L_{ms}}{2} & L_{ls}+L_{ms} \end{bmatrix}$$

$$L^{sr}_{abc} = L_{sr}\begin{bmatrix} cos(\theta) & cos\left(\theta+\frac{2\pi}{3}\right) & cos\left(\theta-\frac{2\pi}{3}\right) \\ cos\left(\theta-\frac{2\pi}{3}\right) & cos(\theta) & cos\left(\theta+\frac{2\pi}{3}\right) \\ cos\left(\theta+\frac{2\pi}{3}\right) & cos\left(\theta-\frac{2\pi}{3}\right) & cos(\theta) \end{bmatrix}$$

$$L^{rs}_{abc} = L^{sr\ T}_{abc} \tag{2.102}$$

$$L_{abc}^{f}=\begin{bmatrix} L_{ls}+f_aL_{ms} & -\frac{f_bL_{ms}}{2} & -\frac{f_cL_{ms}}{2} \\ -\frac{f_aL_{ms}}{2} & L_{ls}+f_bL_{ms} & -\frac{f_cL_{ms}}{2} \\ -\frac{f_aL_{ms}}{2} & -\frac{f_bL_{ms}}{2} & L_{ls}+f_cL_{ms} \end{bmatrix}$$

Noting that:

L_{abc}^{f}: Matrix of fault inductances.

Φ_{abc2}^{s}: Stator fault flux.

Applying the Park transformation to equation (2.101), we get:

a. For the stator:

$$P_s\Phi_{abc}^{s}=P_s(L_{abc}^{ss}i_{abc}^{s}+L_{abc}^{sr}i_{abc}^{r}-L_{abc}^{ss}f_{abc}i_{abc}^{f}) \quad (2.103)$$

$$\Phi_{dq0}^{s}=P_sL_{abc}^{ss}P_s^{-1}(P_si_{abc}^{s})+P_sL_{abc}^{sr}P_r^{-1}(P_ri_{abc}^{r})-P_sL_{abc}^{ss}f_{abc}i_{abc}^{f} \quad (2.104)$$

We arrive at the equation for stator fluxes in the Park frame.

$$\Phi_{dq0}^{s}=P_sL_{abc}^{ss}P_s^{-1}i_{dq0}^{s}+P_sL_{abc}^{sr}P_r^{-1}i_{dq0}^{r}-P_sL_{abc}^{ss}f_{abc}i_{abc}^{f} \quad (2.105)$$

We define: L_{dq0}^{ss},L_{dq0}^{sr} and $L_{dq0\mathrm{f}}^{ss}$ as:

$$L_{dq0}^{ss}=P_sL_{abc}^{ss}P_s^{-1} \quad (2.106)$$

$$L_{dq0}^{sr}=P_sL_{abc}^{sr}P_r^{-1} \quad (2.107)$$

$$L_{dq0\mathrm{f}}^{ss}=P_sL_{abc}^{ss}f_{abc} \quad (2.108)$$

With: $L_{dq0\mathrm{f}}^{ss}=\begin{bmatrix} f_b\sqrt{\frac{2}{3}}(L_{ls}+L_m) & -f_b\sqrt{\frac{1}{6}}(L_{ls}+L_m) & -f_c\sqrt{\frac{1}{6}}(L_{ls}+L_m) \\ 0 & f_b\sqrt{\frac{1}{2}}(L_{ls}+L_m) & -f_c\sqrt{\frac{1}{2}}(L_{ls}+L_m) \\ f_b\sqrt{\frac{1}{3}}(L_{ls}+L_m) & f_b\sqrt{\frac{1}{3}}(L_{ls}+L_m) & f_c\sqrt{\frac{1}{3}}(L_{ls}+L_m) \end{bmatrix}$

$$\Phi_{dq0}^{s}=L_{dq0}^{ss}i_{dq0}^{s}+L_{dq0}^{sr}i_{dq0}^{r}-L_{dq0\mathrm{f}}^{ss}i_{abc}^{f} \quad (2.109)$$

$$\Phi_{abc2}^{s}=f_{abc}\left(L_{abc}^{ss}P_s^{-1}i_{dq0}^{s}+L_{dq0}^{sr}P_r^{-1}i_{dq0}^{r}-L_{abc}^{f}i_{abc}^{f}\right) \quad (2.110)$$

b. For the rotor:

$$P_r\Phi_{abc}^{r}=P_r(L_{abc}^{rr}i_{abc}^{r}+L_{abc}^{rs}i_{abc}^{s}-L_{abc}^{rs}f_{abc}i_{abc}^{f}) \quad (2.111)$$

$$\Phi_{dq0}^{r}=P_rL_{abc}^{rs}P_s^{-1}(P_si_{abc}^{s})+P_rL_{abc}^{rr}P_r^{-1}(P_ri_{abc}^{r})-P_rL_{abc}^{rs}f_{abc}i_{abc}^{f} \quad (2.112)$$

We arrive at the equation for rotor fluxes in the Park frame.

$$\Phi^r_{dq0} = P_r L^{rs}_{abc} P_s^{-1} i^s_{dq0} + P_r L^{rr}_{abc} P_r^{-1} i^r_{dq0} \; -P_r L^{rs}_{abc} f_{abc} i^f_{abc} \tag{2.113}$$

We define: L^{rs}_{dq0}, L^{rr}_{dq0} and L^{rs}_{dq0f} as:

$$L^{rs}_{dq0} = P_r L^{rs}_{abc} P_s^{-1} \tag{2.114}$$

$$L^{rr}_{dq0} = P_r L^{rr}_{abc} P_r^{-1} \tag{2.115}$$

$$L^{rs}_{dq0f} = P_r L^{rs}_{abc} f_{abc} \tag{2.116}$$

$$\Phi^r_{dq0} = L^{rs}_{dq0} i^s_{dq0} + L^{rr}_{dq0} i^r_{dq0} - L^{rs}_{dq0f} i^f_{abc} \tag{2.117}$$

Finally, we have:

$$\begin{cases} \Phi^s_{abc2} = f_{abc}\left(L^{ss}_{abc} P_s^{-1} i^s_{dq0} + L^{sr}_{dq0} P_r^{-1} i^r_{dq0} - L^f_{abc} i^f_{abc}\right) \\ \Phi^s_{dq0} = L^{ss}_{dq0} i^s_{dq0} + L^{sr}_{dq0} i^r_{dq0} - L^{ss}_{dq0\mathrm{f}} i^f_{abc} \\ \Phi^r_{dq0} = L^{rs}_{dq0} i^s_{dq0} + L^{rr}_{dq0} i^r_{dq0} - L^{rs}_{dq0f} i^f_{abc} \end{cases} \tag{2.118}$$

2.4.3. Mechanic equations

The equation for mechanical speed is represented by equation (2.59).

$$J \frac{d}{dt} \Omega = C_e - C_r - f_v \Omega \tag{2.119}$$

We expand the expression of electromechanical torque represented in equation (2.61) to:

$$Ce = P[i'^s_{abc}]^T [\tfrac{d}{d\theta} L'^{sr}_{abc}] \; [i^r_{abc}] \tag{2.120}$$

For a short circuit on the three phases of the stator, the expression of the torque becomes:

$$\mathrm{Ce} = \mathrm{P}[i^s_{dq0}]^T [P_s] [\tfrac{d}{d\theta} L^{sr}_{abc}] [P_r^{-1}] [i^r_{dq0}] + \mathrm{P}[i^f_{abc}]^t \; [f_{abc}] [\tfrac{d}{d\theta} L^{sr}_{abc}] [P_r^{-1}] [i^r_{dq0}] \tag{2.121}$$

2.4.4. State space model

To obtain the state-space model in terms of flux, we expand the expressions (2.121). in matrix form:

$$\begin{bmatrix} \boldsymbol{\Phi^s_{a2}} \\ \boldsymbol{\Phi^s_{b2}} \\ \boldsymbol{\Phi^s_{c2}} \\ \boldsymbol{\Phi^s_d} \\ \boldsymbol{\Phi^s_q} \\ \boldsymbol{\Phi^r_d} \\ \boldsymbol{\Phi^r_q} \end{bmatrix} = \begin{bmatrix} \boldsymbol{L_{11}} & \boldsymbol{L_{12}} & \boldsymbol{L_{13}} & \boldsymbol{L_{14}} & \boldsymbol{L_{15}} & \boldsymbol{L_{16}} & \boldsymbol{L_{17}} \\ \boldsymbol{L_{21}} & \boldsymbol{L_{22}} & \boldsymbol{L_{23}} & \boldsymbol{L_{24}} & \boldsymbol{L_{25}} & \boldsymbol{L_{26}} & \boldsymbol{L_{27}} \\ \boldsymbol{L_{31}} & \boldsymbol{L_{32}} & \boldsymbol{L_{33}} & \boldsymbol{L_{34}} & \boldsymbol{L_{35}} & \boldsymbol{L_{36}} & \boldsymbol{L_{37}} \\ \boldsymbol{L_{41}} & \boldsymbol{L_{42}} & \boldsymbol{L_{43}} & \boldsymbol{L_{44}} & \boldsymbol{L_{45}} & \boldsymbol{L_{46}} & \boldsymbol{L_{47}} \\ \boldsymbol{L_{51}} & \boldsymbol{L_{52}} & \boldsymbol{L_{53}} & \boldsymbol{L_{54}} & \boldsymbol{L_{55}} & \boldsymbol{L_{56}} & \boldsymbol{L_{57}} \\ \boldsymbol{L_{61}} & \boldsymbol{L_{62}} & \boldsymbol{L_{63}} & \boldsymbol{L_{64}} & \boldsymbol{L_{65}} & \boldsymbol{L_{66}} & \boldsymbol{L_{67}} \\ \boldsymbol{L_{71}} & \boldsymbol{L_{72}} & \boldsymbol{L_{73}} & \boldsymbol{L_{74}} & \boldsymbol{L_{75}} & \boldsymbol{L_{76}} & \boldsymbol{L_{77}} \end{bmatrix} \begin{bmatrix} \boldsymbol{i^f_a} \\ \boldsymbol{i^f_b} \\ \boldsymbol{i^f_c} \\ \boldsymbol{i^s_d} \\ \boldsymbol{i^s_q} \\ \boldsymbol{i^r_d} \\ \boldsymbol{i^r_q} \end{bmatrix} \tag{2.122}$$

Where:

$$[\boldsymbol{\Phi}] = [\boldsymbol{L}][\boldsymbol{I}] \tag{2.123}$$

With

$$[\Phi] = [\Phi_{a2}^{s} \quad \Phi_{b2}^{s} \quad \Phi_{c2}^{s} \quad \Phi_{d}^{s} \quad \Phi_{q}^{s} \quad \Phi_{d}^{r} \quad \Phi_{q}^{r}]^{t}$$

$$[I] = \left[i_a^f \quad i_b^f \quad i_c^f \quad i_d^s \quad i_q^s \quad i_d^r \quad i_q^r\right]^t$$

$$[\boldsymbol{L}] = \begin{bmatrix} \boldsymbol{L_{11}} & \boldsymbol{L_{12}} & \boldsymbol{L_{13}} & \boldsymbol{L_{14}} & \boldsymbol{L_{15}} & \boldsymbol{L_{16}} & \boldsymbol{L_{17}} \\ \boldsymbol{L_{21}} & \boldsymbol{L_{22}} & \boldsymbol{L_{23}} & \boldsymbol{L_{24}} & \boldsymbol{L_{25}} & \boldsymbol{L_{26}} & \boldsymbol{L_{27}} \\ \boldsymbol{L_{31}} & \boldsymbol{L_{32}} & \boldsymbol{L_{33}} & \boldsymbol{L_{34}} & \boldsymbol{L_{35}} & \boldsymbol{L_{36}} & \boldsymbol{L_{37}} \\ \boldsymbol{L_{41}} & \boldsymbol{L_{42}} & \boldsymbol{L_{43}} & \boldsymbol{L_{44}} & \boldsymbol{L_{45}} & \boldsymbol{L_{46}} & \boldsymbol{L_{47}} \\ \boldsymbol{L_{51}} & \boldsymbol{L_{52}} & \boldsymbol{L_{53}} & \boldsymbol{L_{54}} & \boldsymbol{L_{55}} & \boldsymbol{L_{56}} & \boldsymbol{L_{57}} \\ \boldsymbol{L_{61}} & \boldsymbol{L_{62}} & \boldsymbol{L_{63}} & \boldsymbol{L_{64}} & \boldsymbol{L_{65}} & \boldsymbol{L_{66}} & \boldsymbol{L_{67}} \\ \boldsymbol{L_{71}} & \boldsymbol{L_{72}} & \boldsymbol{L_{73}} & \boldsymbol{L_{74}} & \boldsymbol{L_{75}} & \boldsymbol{L_{76}} & \boldsymbol{L_{77}} \end{bmatrix}$$

The elements of the stator and rotor inductance matrix are in the appendix B.

From equation (2.97), we develop the state-space model in terms of flux for an IM with SITSC faults.

$$\begin{cases} \dfrac{d}{dt}\Phi_{a2}^{s} = \left(f_a R_s + r_{af}\right) i_a^f - f_a \sqrt{\dfrac{2}{3}} R_s i_d^s \\ \dfrac{d}{dt}\Phi_{b2}^{s} = \left(f_b R_s + r_{bf}\right) i_b^f + f_b \sqrt{\dfrac{1}{6}} R_s i_d^s - f_b \sqrt{\dfrac{1}{2}} R_s i_q^s \\ \dfrac{d}{dt}\Phi_{c2}^{s} = \left(f_c R_s + r_{cf}\right) i_c^f + f_c \sqrt{\dfrac{1}{6}} R_s i_d^s + f_c \sqrt{\dfrac{1}{2}} R_s i_q^s \\ \dfrac{d}{dt}\Phi_{d}^{s} = v_d^s + f_a \sqrt{\dfrac{2}{3}} R_s i_a^f - f_b \sqrt{\dfrac{1}{6}} R_s i_b^f - f_c \sqrt{\dfrac{1}{6}} R_s i_c^f - R_s i_d^s \\ \dfrac{d}{dt}\Phi_{q}^{s} = v_q^s + f_b \sqrt{\dfrac{1}{2}} R_s i_b^f - f_c \sqrt{\dfrac{1}{2}} R_s i_c^f - R_s i_q^s \\ \dfrac{d}{dt}\Phi_{d}^{r} = \omega_r \Phi_q^r - R_s i_d^r \\ \dfrac{d}{dt}\Phi_{q}^{r} = -\omega_r \Phi_d^r - R_s i_q^r \end{cases} \tag{2.124}$$

In a condensed manner:

$$\left[\dot{\Phi}\right] = [\mathrm{B}]\,[\mathrm{V}] + \omega_r [\mathrm{A}]\,[\Phi] - [\mathrm{R}]\,[I] \tag{2.125}$$

Where:

$$\left[\dot{\Phi}\right] = \left[\dot{\Phi_{a2}^{s}} \quad \dot{\Phi_{b2}^{s}} \quad \dot{\Phi_{c2}^{s}} \quad \dot{\Phi_{d}^{s}} \quad \dot{\Phi_{q}^{s}} \quad \dot{\Phi_{d}^{r}} \quad \dot{\Phi_{q}^{r}}\right]^{t}$$

The currents can be expressed in terms of the fluxes, by inversing equation (2.123).

For L to be invertible, it is necessary that f_a, f_b and $f_c$are different from zero.

$$[L]^{-1} = [L^{-1}] \quad (2.126)$$

We have:

$$[I] = [L^{-1}]\,[\Phi] \quad (2.127)$$

In a condensed manner, we can write:

$$\left[\dot{\Phi}\right] = [\mathrm{B}]\,[\mathrm{V}] + \omega_r[\mathrm{A}]\,[\Phi] - [\mathrm{R}]\,([L^{-1}]\,[\Phi]) \quad (2.128)$$

The state model of the asynchronous machine with faults can thus be defined by the following system of equations:

$$\left[\dot{\Phi}\right] = (\omega_r[\mathrm{A}] - [\mathrm{R}]\,[L^{-1}])\,[\Phi] + [\mathrm{B}]\,[\mathrm{V}] \quad (2.129)$$

With:

$$\mathrm{B}=\begin{bmatrix} 0 & 0 & 0 & 0 & 0 & 0 & 0 \\ 0 & 0 & 0 & 0 & 0 & 0 & 0 \\ 0 & 0 & 0 & 0 & 0 & 0 & 0 \\ 1 & 0 & 0 & 0 & 0 & 0 & 0 \\ 0 & 1 & 0 & 0 & 0 & 0 & 0 \\ 0 & 0 & 0 & 0 & 0 & 0 & 0 \\ 0 & 0 & 0 & 0 & 0 & 0 & 0 \end{bmatrix} \qquad \mathrm{A}=\begin{bmatrix} 0 & 0 & 0 & 0 & 0 & 0 & 0 \\ 0 & 0 & 0 & 0 & 0 & 0 & 0 \\ 0 & 0 & 0 & 0 & 0 & 0 & 0 \\ 0 & 0 & 0 & 0 & 0 & 0 & 0 \\ 0 & 0 & 0 & 0 & 0 & 0 & 0 \\ 0 & 0 & 0 & 0 & 0 & 0 & -1 \\ 0 & 0 & 0 & 0 & 0 & 1 & 0 \end{bmatrix}$$

$$\mathrm{R}=\begin{bmatrix} r_{11} & r_{12} & r_{13} & r_{14} & r_{15} & r_{16} & r_{17} \\ r_{21} & r_{22} & r_{23} & r_{24} & r_{25} & r_{26} & r_{27} \\ r_{31} & r_{32} & r_{33} & r_{34} & r_{35} & r_{36} & r_{37} \\ r_{41} & r_{42} & r_{43} & r_{44} & r_{45} & r_{46} & r_{47} \\ r_{51} & r_{52} & r_{53} & r_{54} & r_{55} & r_{56} & r_{57} \\ r_{61} & r_{62} & r_{63} & r_{64} & r_{65} & r_{66} & r_{67} \\ r_{71} & r_{72} & r_{73} & r_{74} & r_{75} & r_{76} & r_{77} \end{bmatrix} \qquad \mathrm{V}=\begin{bmatrix} 0 \\ 0 \\ 0 \\ v_d^s \\ v_q^s \\ 0 \\ 0 \end{bmatrix}$$

The elements of the stator and rotor resistance matrix are in the appendix B.

2.5. Simulation results

In this section, we address the simulation of the IM models established in previously.

- The simulation is carried out in the Matlab/Simulink environment, which provides the opportunity to analyze the machine's behavior under various unbalance and fault conditions.
- The simulation parameters for the machine are presented in table 2.1.
- The simulation of the two models is established for a star-connected IM. The machine is feed by a balanced system of three-phase voltages in the given form:

- $\begin{bmatrix} V_a \\ V_b \\ V_c \end{bmatrix} = 220 * \sqrt{2} \begin{bmatrix} \sin(2\pi f * t) \\ \sin(2\pi f * t - 2\pi/3) \\ \sin(2\pi f * t - 4\pi/3) \end{bmatrix}$ with $f_s = 50Hz$.

Table 2.1 The IM parameters used for the simulation	
Maximum voltage (V)	220√2
Rated Current (A)	1.6
Nombre of winding turns per phase	528
Nombre of pole pairs	2
Moment of inertia	0.00177007
Viscous Coefficient	0.0006437777
Resistance of stator (Ω)	13.6324
Resistance of rotor (Ω)	13.3072
Resistance of fault (Ω)	1.3
Frequency (Hz)	50
Mutuelle Inductance (H)	0.6380
Stator leakage inductance (H)	0.0388
Rotor leakage inductance (H)	0.0388

2.5.1. Induction motor asymmetrical-model simulation

First, we will provide and interpret the results obtained from the simulation of a symmetrical IM, which it is called healthy. Then, we will analyze the behavior of an asymmetric machine, which is also healthy but differently constructed.

In case of symmetrical IM, the simulation involves a no-load start followed by the application of a resistive torque (*Cr = 3.8 Nm*) at *t=0.5 s*. figures from 2.4 to 2.9 illustrate the obtained results.

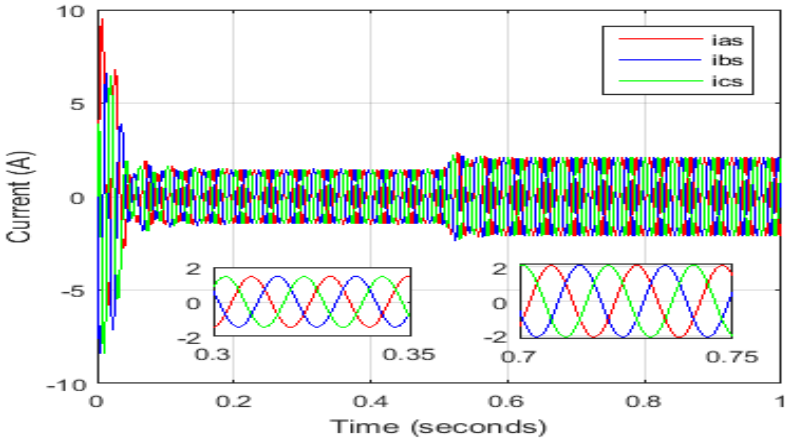

Figure 2.4: Stator current signals.

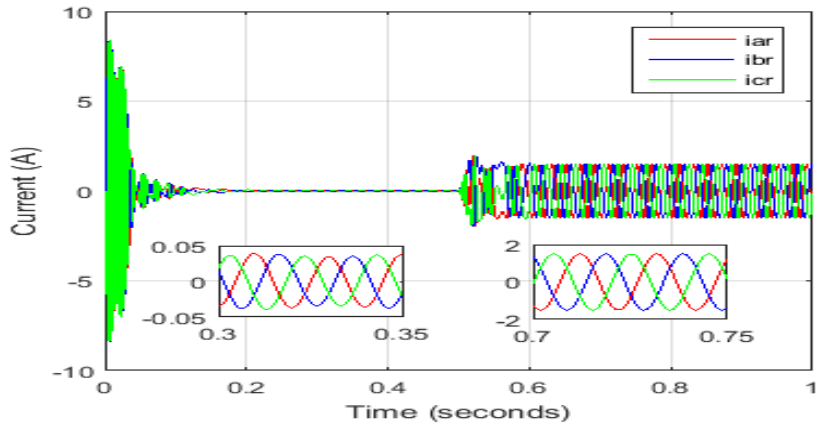

Figure 2.5: Rotor current signals

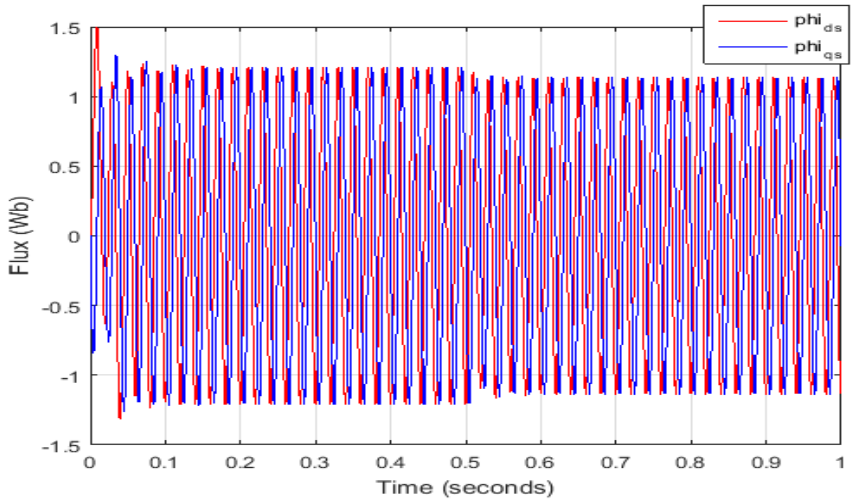

Figure 2.6: Park's stator flux signals

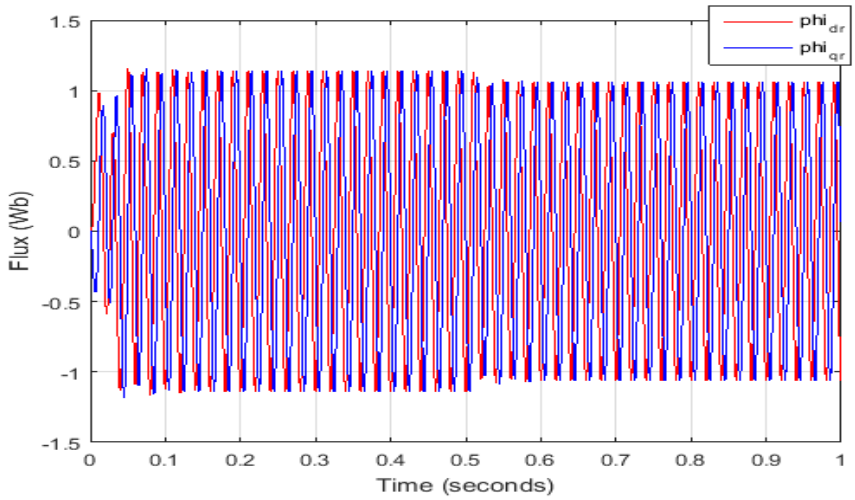

Figure 2.7: Park's rotor flux signals

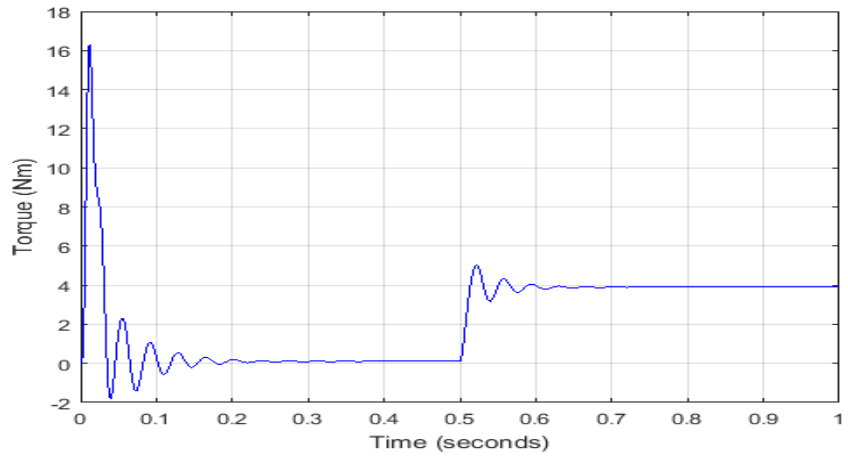

Figure 2.8 : Electromagnetic Torque signal

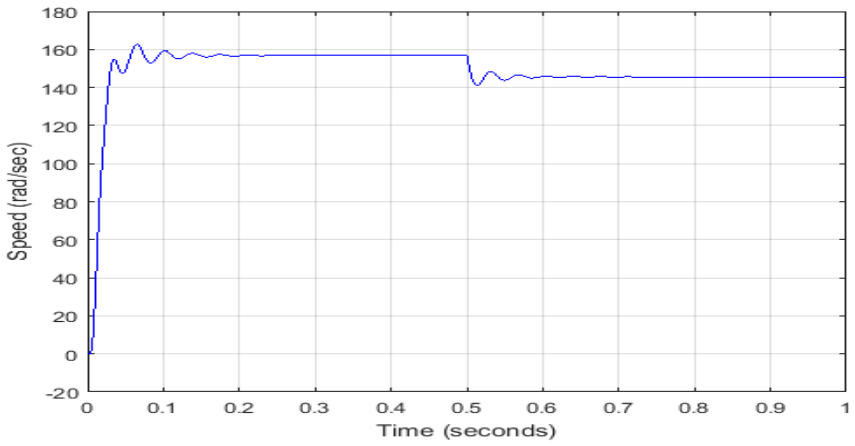

Figure 2.9 : Mechanic Speed signal

All quantities settle quickly after a transient regime of *0.25s*, representing the machine's response time. There is a strong initial surge in stator current, although brief, which then stabilizes at a constant value of *1.45* A, defining the current required for the magnetization of the machine at no-load (Figure 2.4). A brief surge in rotor current occurs, followed by stabilization at an almost negligible value at no-load (Figure 2.5).

In the initial moments of start-up, the electromagnetic torque exhibits oscillations reaching a maximum value of *16.3 Nm*. This is necessary to overcome the motor's inertia, and then it returns to a very low value to compensate for no-load mechanical losses (Figure 2.8).

The speed evolution over time shows a steady increase, eventually settling around the synchronous speed (*≈156.8 rad/s*) after *0.25s* (Figure 2.9). With the application of the load (*Cr = 3.8 Nm*) to the machine at time *t=0.5s*, the stator current increases, the electromagnetic torque grows to the imposed load value (*Cr*), and the speed decreases to *145.5 rad/s*.

Figures from 2.10 to 2.15 illustrate the results of Asymmetrical IM model simulation. This simulation will be conducted under the same conditions as the symmetrical IM. The goal is to clearly observe the differences in the behavior of variables between a symmetrical and asymmetrical IM. In this case, IM model has 30 turns subtracted from phase a_s, 50 turns from phase b_s, and 70 turns from phase c_s.

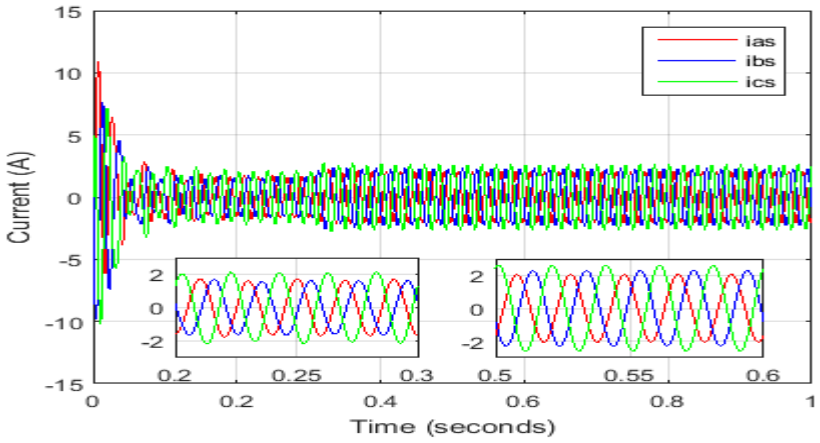

Figure 2.10: Stator current signals.

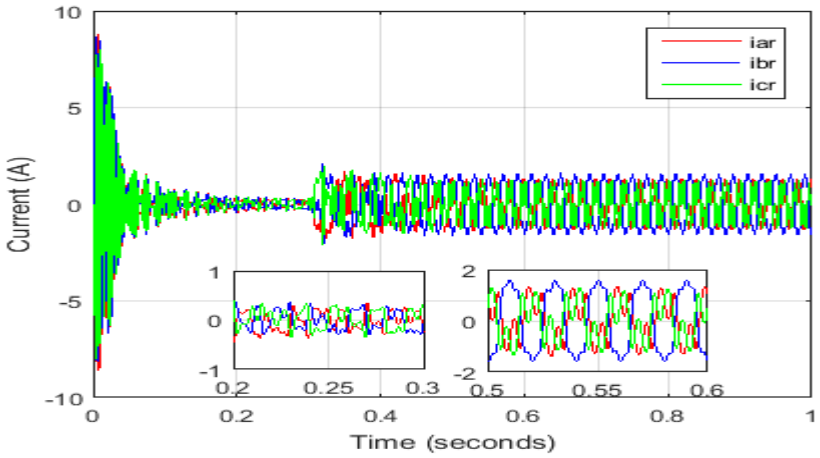

Figure 2.11: Rotor current signals

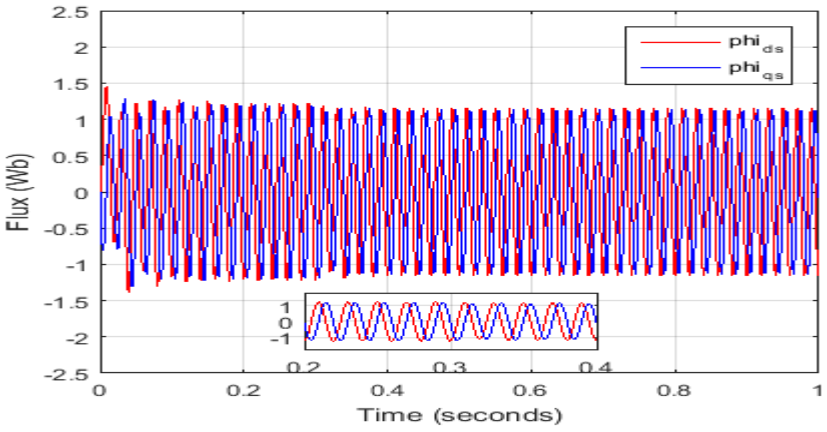

Figure 2.12: Park's stator flux signals

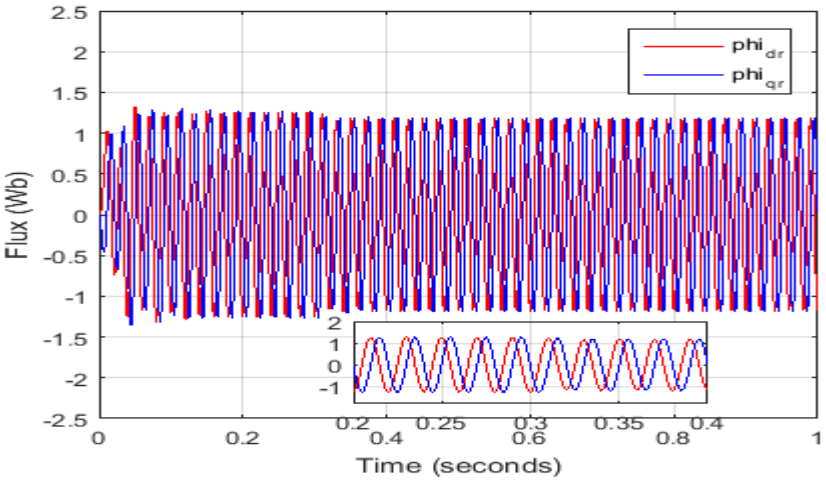

Figure 2.13: Park's rotor flux signals.

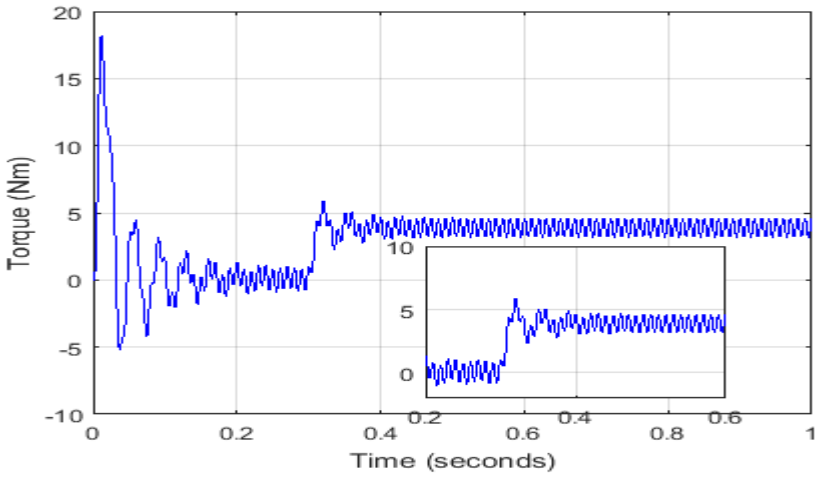

Figure 2.14 : Electromagnetic Torque signal.

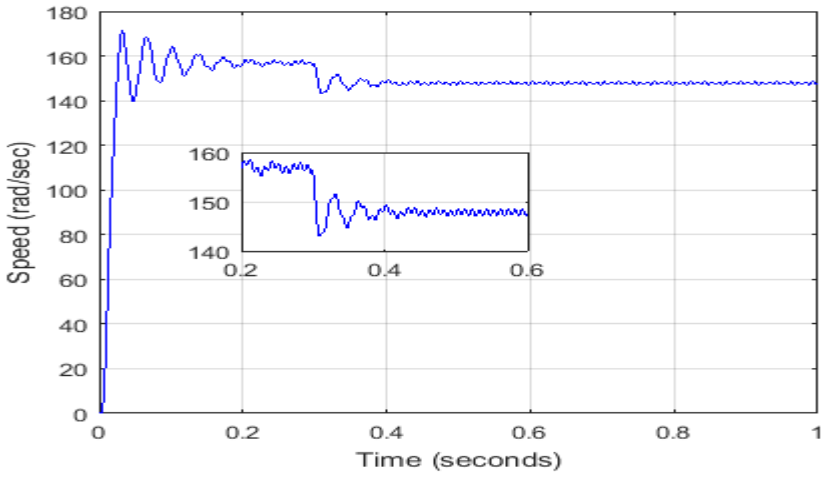

Figure 2.15 : Mechanic Speed signal

The machine exhibits asymmetry in all three phases. There is an increase in stator currents in all three phases, which have changed from *1.45 A* to *1.68 A* for phase a_s, *1.61 A* for phase b_s, and *2.1 A* for phase c_s. This fault is manifested as an irregular evolution of current in the phases, as illustrated in Figure 2.10. The change in the number of turns of the windings influences the rotor current, and a deformation in the waveform of the graphs is perceived (Figure 2.11).

In the initial moments of start-up, the electromagnetic torque exhibits oscillations reaching a maximum value of *18 Nm*. It is notable that there are ripples in the torque waveform in the steady-state regime, as shown in Figure 2.14.

A steady increase in speed during startup, settling at *157 rad/s*, is observed. As speed reflects the electromagnetic torque, its evolution in the steady-state regime also shows a wavy pattern (Figure 2.15), which is dampened by the inertia of the load. This implies intense mechanical vibrations.

2.5.2. Induction motor SITSC- model simulation

The objective of this section is to clearly observe the difference in the evolution of quantities between a faulty machine and a healthy machine. We will present the simulation of a no-load start under sinusoidal voltage followed by the application of a resisting torque (*Cr = 3.8 Nm*) at time *t=0.3s*. The machine has a short circuit of 30 turns on phase $a_s$at time *t=0.4s*, then 50 turns on phase b_s at time *t=0.6s*, and finally, 70 turns on phase c_s at time *t=0.8s*. The results obtained from the simulation are presented in figures from 2.16 to 2.21.

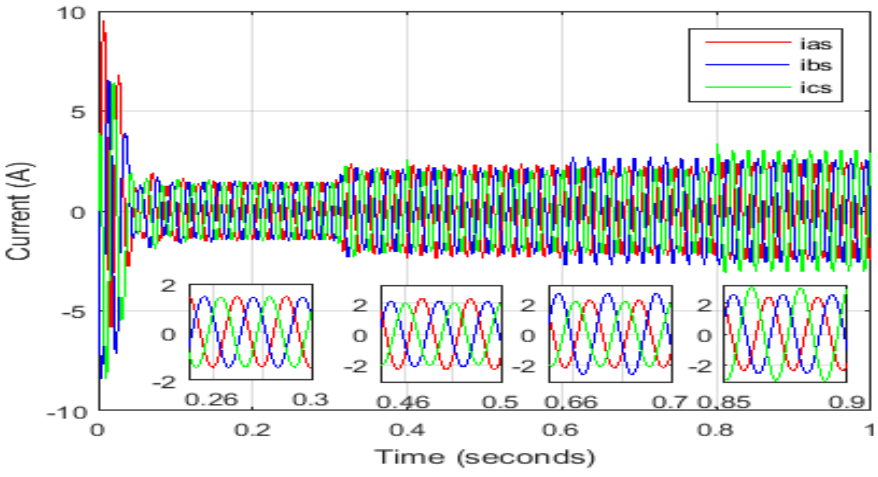

Figure 2.16: Stator current signals

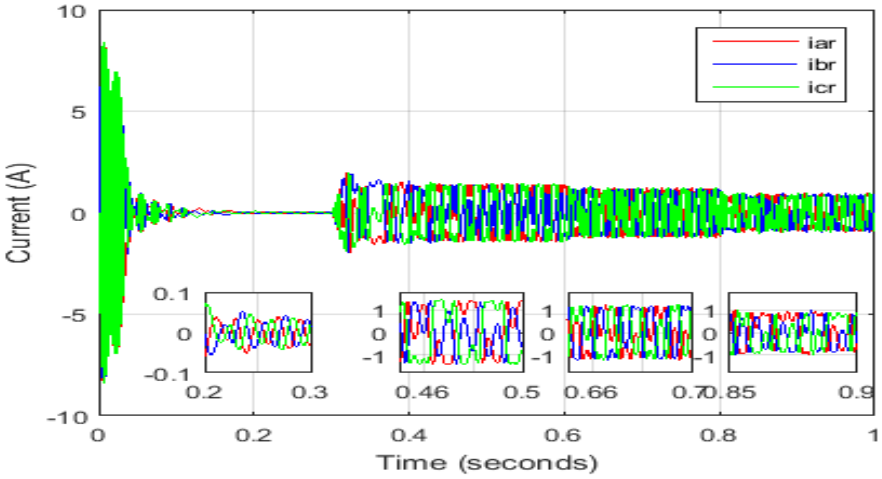

Figure 2.17: Rotor current signals

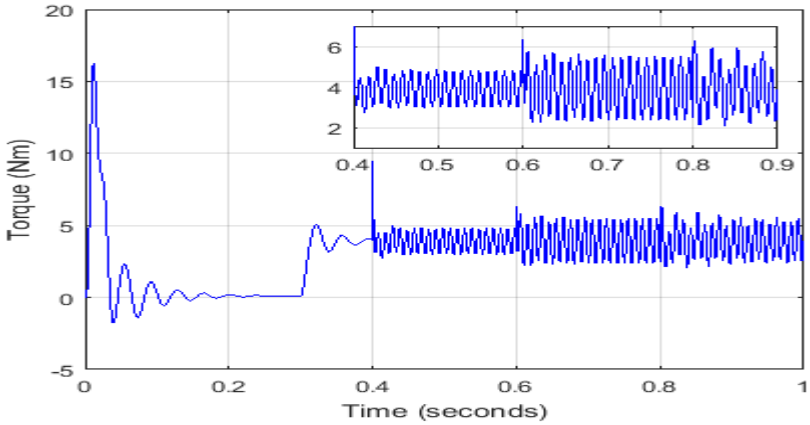

Figure 2.18 : Electromagnetic Torque signal

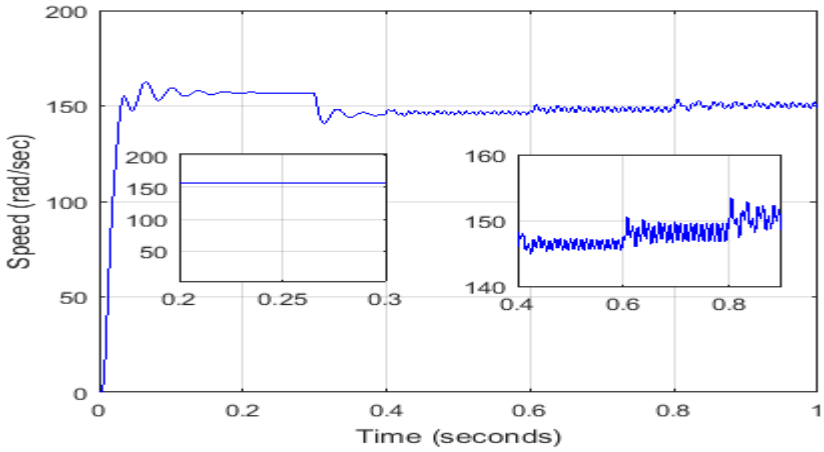

Figure 2.19 : Mechanic Speed signal

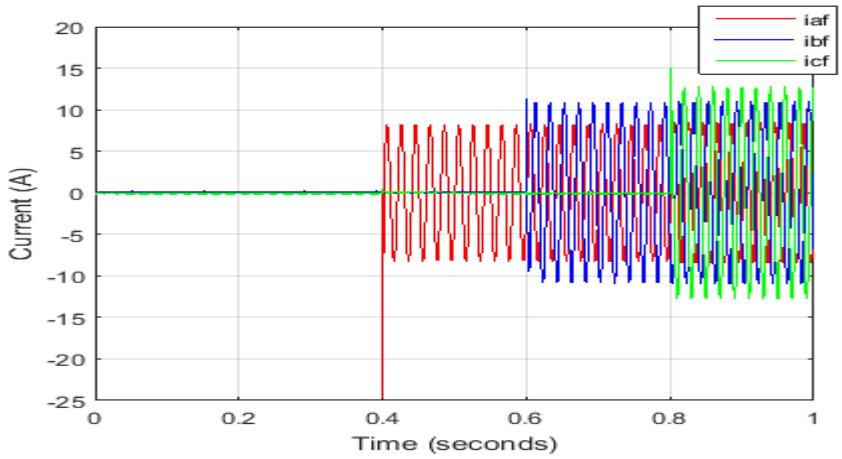

Figure 2.20: Faulty current signals

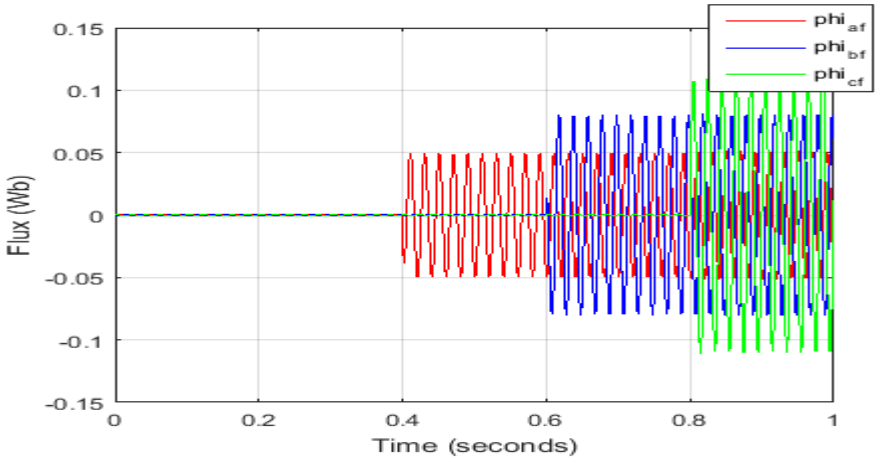

Figure 2.21: Faulty flux signals

Upon the occurrence of a short-circuit fault starting at $t = 0.4\ s$, it is observed that the amplitude of the current in phase $a_s$is larger than the other phases (Figure 2.16). At $t = 0.6\ s$, the amplitude of the current in phase $b_s$is getting bigger than the phases a_s, c_s. Finally; at $t = 0.8\ s$, the amplitude of phase $c_s$is higher than the phases a_s, b_s. Thus, it can be noticed that the rotor currents of the IM are strongly influenced by the fault, as these signals are highly distorted (figure 2.17).

The electromagnetic torque exhibits strong oscillations from the moment the fault appears at $t = 0.4\ s$, due to the unbalance in currents that give birth to it (figure 2.18). These oscillations are dampened at the mechanical speed level due to the inertia of the rotor (figure 2.19).

The appearance of fault currents and fluxes, taking a sinusoidal shape, is visualized. It is observed that the larger the number of short-circuited turns, the more significant the increase in amplitudes, as illustrated in Figure 2.20 and 2.21.

2.5.3. Comparison & comments

In order to compare the two models developed and simulated previously, a table summarizing the results of multiple simulations is presented below (table 2.2). In this table, the amplitude of stator currents was considered to discern and compare the outcomes of the two models. Both models were simulated for various cases of unbalance in one or more phases.

Table 2.2: The amplitude of stator currents for the two models

Unbalance stator phases			Asymmetrical motor model				SITSC motor model			
a_s	b_s	c_s	i_{as} (A)	i_{bs} (A)	i_{cs} (A)	Ω *(rad/sec)*	i_{as} (A)	i_{bs} (A)	i_{cs} (A)	Ω *(rad/sec)*
6	-	-	1.5	1.5	1.4	156.8	1.5	1.5	1.4	156.8
-	24	-	1.4	1.6	1.5	156.9	1.4	1.6	1.6	156.9
-	-	30	1.6	1.3	1.7	156.8	1.6	1.4	1.6	156.8
30	6	-	1.7	1.6	1.3	156.8	1.6	1.6	1.4	156.9
-	30	24	1.4	1.6	1.7	156.8	1.5	1.6	1.7	156.8
6	-	30	1.6	1.3	1.7	156.8	1.6	1.4	1.6	156.8
24	30	6	1.5	1.7	1.5	156.8	1.6	1.7	1.5	156.9

Upon observing the preceding table, it is evident that both models yielded values close to 99% for the two measurements of current and mechanical speed. Furthermore, the discrepancy between the two measurement models appears to be minimal. Thus, we can conclude that the inclusive SITSC motor model is valuable for studying fault detection.

2.6. Experimental investigation

2.6.1 Description of the test bed.

The test-bed (figure 2.22) comprises a power supply voltage source with an RMS value of 380 V per phase applied to the terminals of the three star-coupled stator phases of the IM. These voltages form a system of balanced sinusoidal three-phase voltages with a frequency of 50Hz. A three-phase rewound IM was used, possessing the same parameters as the IM models. Its stator contains four coils for each phase, with each coil having 132 turns connected in series. The motor was rewound to create stator short-circuits, as

depicted in Figure 2.23(a). Current and voltage were measured using Hall-effect sensors, and the signals from these sensors were conditioned and amplified using an op-amp based circuit, as shown in Figure 2.23(b). The measured signals go through a filtering with a Butterworth-type anti-aliasing low pass filter with a 500Hz cutting frequency. The DSPACE1104 platform, equipped with MPC 8240 processor, was used for signal acquisition and control figure 2.23(c). This platform can be directly programmed using MATLAB/Simulink software. The program was integrated into Simulink using the basic functions and specific blocks of the DSPACE system, and after successful debugging; it was uploaded onto the DS1104 platform. The CONTROLDESK software managed the platform and supervised the experiment, offering the ability to access, visualize, and record various variables for further analysis. Additionally, it allowed online modification of program parameters, such as regulator gains.

Figure 2.22: Experimental test bed

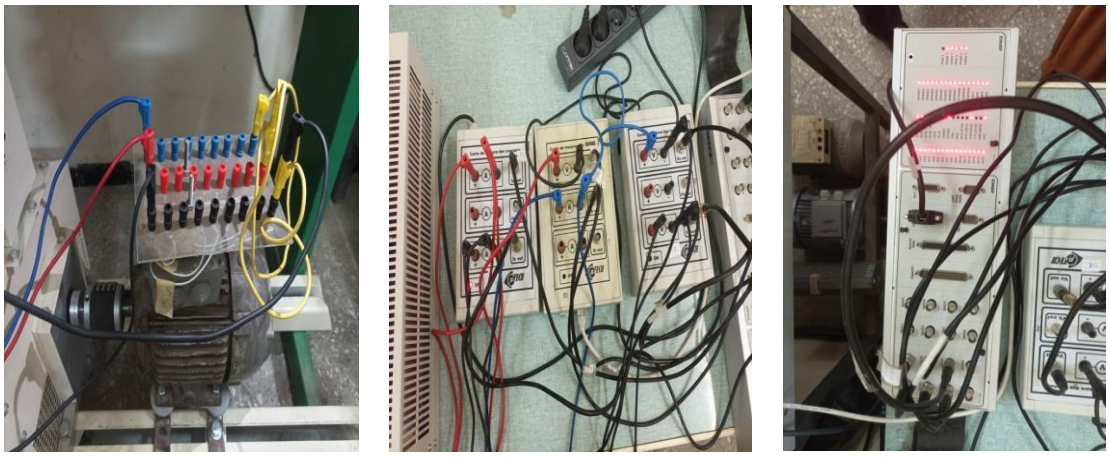

(a) (b) (c)

Figure 2.23: (a) rewound IM, (b) currents & voltages measuring boxes, (c) DS1104 acquisition card.

2.6.2. Start-up of the test-bed

Figures from 2.24(a) to 2.24(d) illustrate the results of experimental IM start-up. This start-up will be conducted under the different cases of unbalance stator. The goal is to clearly observe the currents of a real motor.

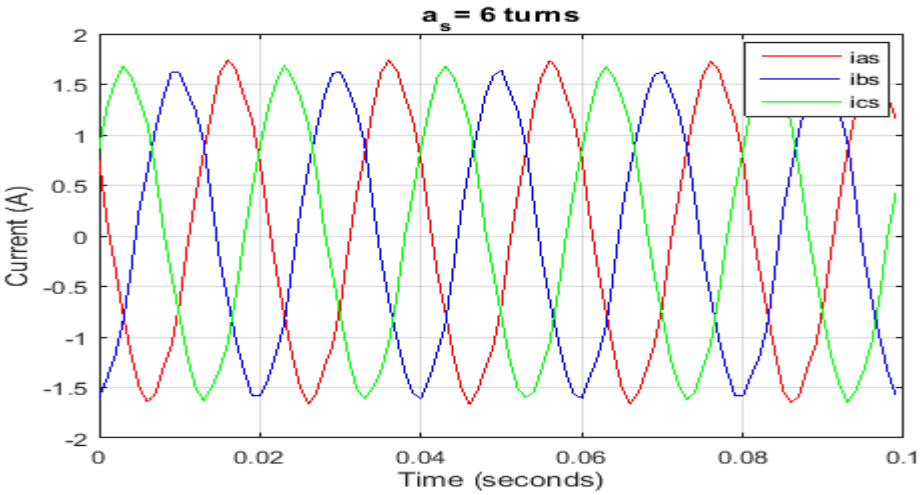

(a)

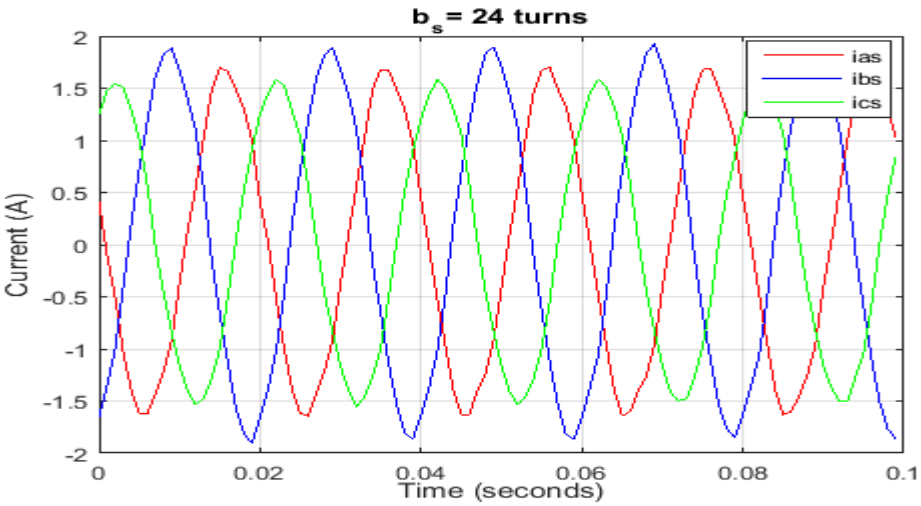

(b)

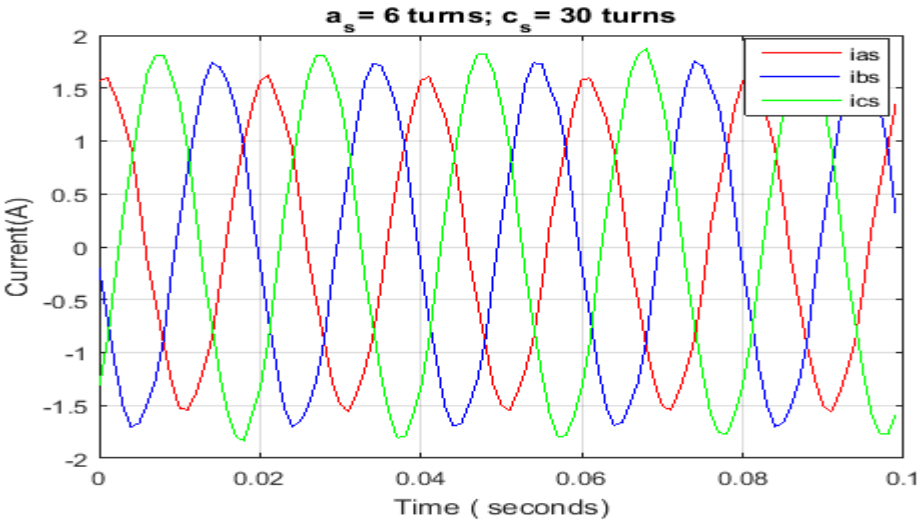

(c)

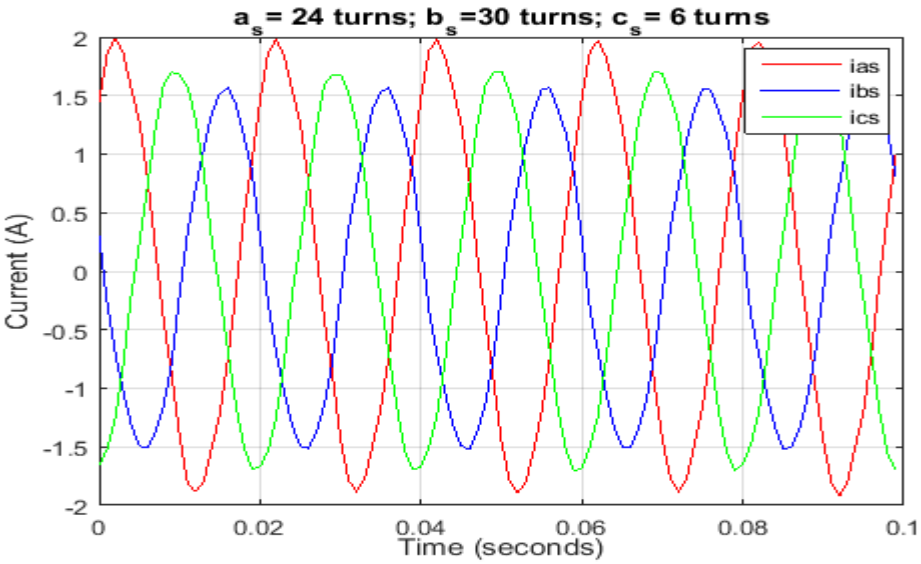

(d)

Figure 2.24: Currents signals of experimental IM.

It can be seen from Figure 2.24 that the curves are not smooth and this is due to the fact of sampling time which equal to 10^{-4} second (data acquisition). The results show that for a case of a short circuit in one phase, the amplitude of the current of the concerned phase is larger than the other healthy ones. Unlike the appearance of the short circuit in two or more phases, the current amplitudes increase in different ways.

2.6.3. Comparison & comments

In this section, we opt for comparison between the two models and experimental IM, a table summarizing the results of multiple simulations is presented below (table 2.3).

In this table, the amplitudes of stator currents were considered to observe and compare the outcomes of different bases. All systems were simulated for various cases of unbalance in one or more phases.

Table 2.3 The amplitude of stator currents

Number of removed turns			Asymmetrical motor model			SITSC motor model			Experimental simulation		
a_s	b_s	c_s	i_{as} (A)	i_{bs} (A)	i_{cs} (A)	i_{as} (A)	i_{bs} (A)	i_{cs} (A)	i_{as} (A)	i_{bs} (A)	i_{cs} (A)
6	0	0	1.5	1.5	1.4	1.5	1.5	1.4	1.7	1.6	1.6
0	24	0	1.4	1.6	1.5	1.4	1.6	1.6	1.5	1.7	1.8
0	0	30	1.6	1.3	1.7	1.6	1.4	1.6	1.7	1.9	1.6
30	6	0	1.7	1.6	1.3	1.6	1.6	1.4	1.9	1.6	1.7
0	30	24	1.4	1.6	1.7	1.5	1.6	1.7	1.6	1.9	1.8
6	0	30	1.6	1.3	1.7	1.6	1.4	1.6	1.7	1.9	1.6
24	30	6	1.5	1.7	1.5	1.6	1.7	1.5	1.7	1.8	1.9

Upon observing the last table, we see that the measurements of the rewound motor are slightly higher than the two created models. This is due to the fact that the motor is powered by supply voltage source that is obviously unbalanced. Furthermore, the simplifying assumptions already made in section (2.2.3) are not guaranteed in real mode. The experimental current measurements are close to 80% for both models; indeed, the difference between the motor measurements and the two models sometimes seems significant (a difference of 0.5 A). But; by carefully noticing the results, we can realize that the model with SITSC is a bit closer to experimental motor.

2.7. Conclusion

In this chapter, we have modeled the asymmetric induction machine and the machine with stator short-circuit fault. This modeling is based on the application of the Park transformation, the primary advantage of which is to simplify the three-phase model into a two-phase model. This modeling will serve as a basis for developing the two models.

The asymmetric model of the IM assumes that the stator phases do not have the same number of turns. The model with a fault assumes that the short-circuited phase is divided into two parts (healthy portion and short-circuited portion).

The modeling of the IM with a stator inter-turn short-circuit fault allowed for a precise simulation of the machine's behavior under fault conditions. It requires a significant computation time due to the number of differential equations representing the model.

Finally, we have validated the operation of a (healthy) symmetric and asymmetric induction machine through simulation. From a modeling perspective, a symmetric induction machine can be considered a special case of the asymmetric machine, and the asymmetric machine is a healthy machine but constructed in a different way. Then, we have compared the results obtained through simulation and experimentation for the two developed models.

Chapter (3)
Detection, classification and severity estimation of Multi induction motor faults

3.1. Introduction

In this chapter, two types of IM diagnosis were discussed.

The first one is Fault Detection and Classification (FDC) of SITSC. A Feed Forward Neural Network (FFNN), trained by the back-propagation algorithm, is applied for the FDC process. It is based on monitoring the three-phase instantaneous power average (*IP*) using the stator currents and voltages.

The second diagnosis involves an efficient approach to estimate the percentage of SITSC and detect Unbalance Supply Voltage (USV) occurrences. A fault classifier for SITSC and USV is implemented using a Multi-Layer Perceptron Neuronal Network (MLP-NN). The fault identification process monitors three types of signals: total instantaneous power, shift between line current and phase voltage, and negative sequence voltage.

Both approaches demonstrate good performance in the diagnostic field.

3.2. Detection and classification of SITSC fault

This section introduces an ANN-based approach for detecting and classifying SITSC faults in a three-phase Induction Motor. The FDC process enables the identification of SITSC faults and categorizes them into phases a_s, b_s, or c_s. A feed forward neural network (FF-NN) trained by the back propagation algorithm is employed. The FDC process relies on monitoring the average three-phase instantaneous power (*IP*) using stator currents and voltages signals.

3.2.1. Fault indicators selection

The FDC process uses instantaneous power signals to pursue the diagnosis. IP is obtained using only motor current and voltage signals.

3.2.1.1. Instantaneous power analysis

The selection of anomaly indicators is a crucial initial step in the fault detection and classification, its selection directly influences the final results. In this section, we conduct a study on the behavior of three-phase instantaneous power (*IP*) in the presence of SITSC faults. The IM model with SITSC fault developed previously in chapter 2 is used to gain the issue. The three phases IPs are calculated as follow [48]:

$$\begin{cases} IP_{as}(t) = V_{as}(t) \times I_{as}(t) \\ IP_{bs}(t) = V_{bs}(t) \times I_{bs}(t) \\ IP_{cs}(t) = V_{cs}(t) \times I_{cs}(t) \end{cases} \tag{3.1}$$

Simulation results for the three-phase instantaneous power in healthy and faulty cases are shown in Figures from 3.1 to 3.4.

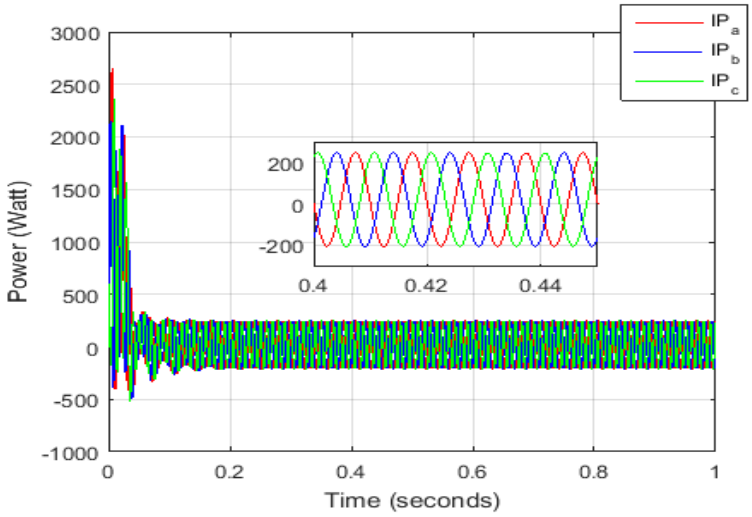

Figure 3.1: Simulation of *IP* (healthy case)

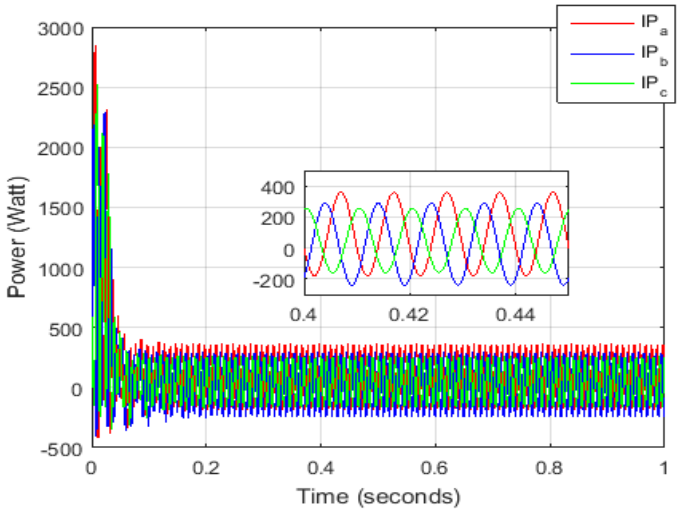

Figure 3.2: Simulation of *IP* (fault in phase a_s)

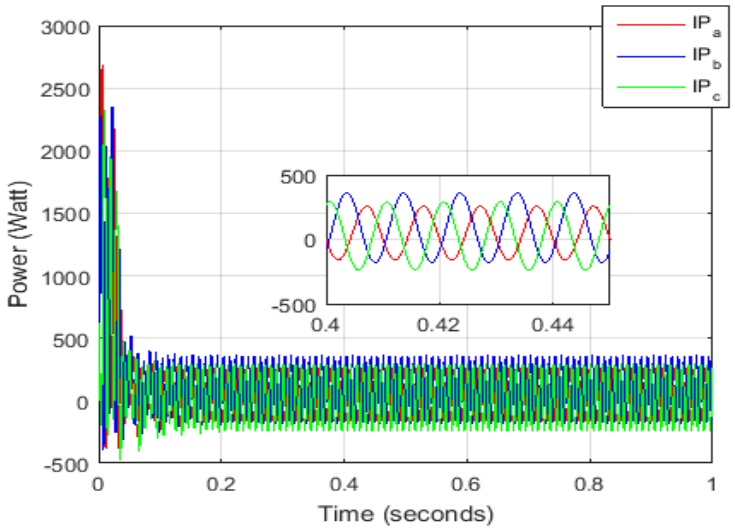

Figure 3.3: Simulation of *IP* (fault in phase b_s)

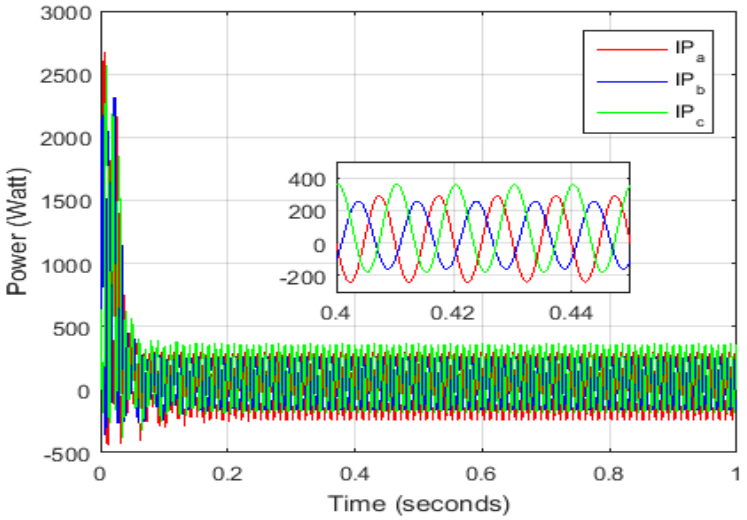

Figure 3.4: Simulation of *IP* (fault in phase c_s)

Upon examining the preceding figures, it is observed that the instantaneous power signal is a sinusoidal signal with a frequency of 100 Hz, since it is the product of the current and voltage signals. Initially, the motor takes high values, which are necessary for motor startup (high power required to turn on a motor). Thus, its average value is not equal to zero like the current and voltage signals, but it is a low value that keeps the motor running. In a healthy motor scenario, the instantaneous power values have the same amplitude in the whole phases. The occurrence of a short circuit fault brings change in the amplitudes, where the damaged phase has a higher average value of *IP* than the others, leading to a change in the amplitude.

3.2.1.2. Load torque variation influence

Load torque variation in one of the motor common functioning conditions. It influences on currents, consequently on instantaneous power. Therefore, analyzing it is very important to see whether it can give a fault alarm for the FDC process or not. Figures from 3.5 to 3.8 illustrate the *IP* signals under no load condition, then a load torque is applied at *t=0.3s* where $c_r = 3.8\ Nm$.

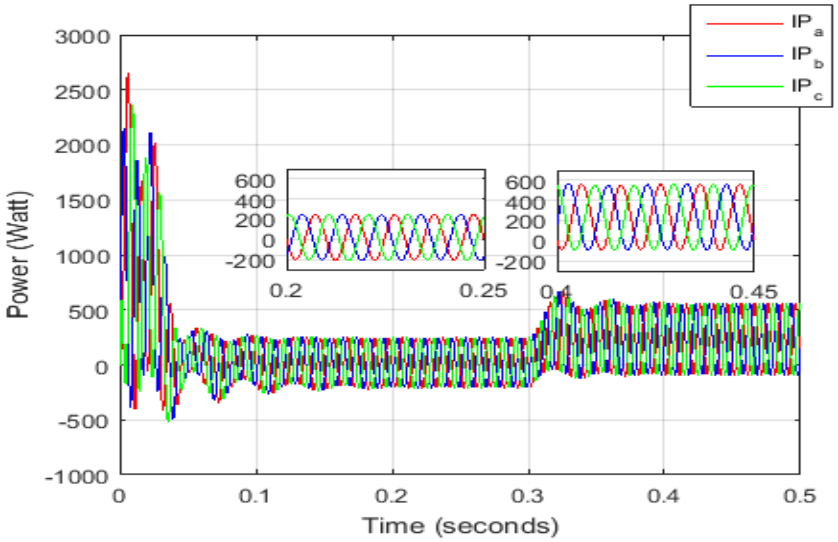

Figure 3.5: Simulation of *IP* (healthy case) under load torque ($c_r = 3.8\ Nm$)

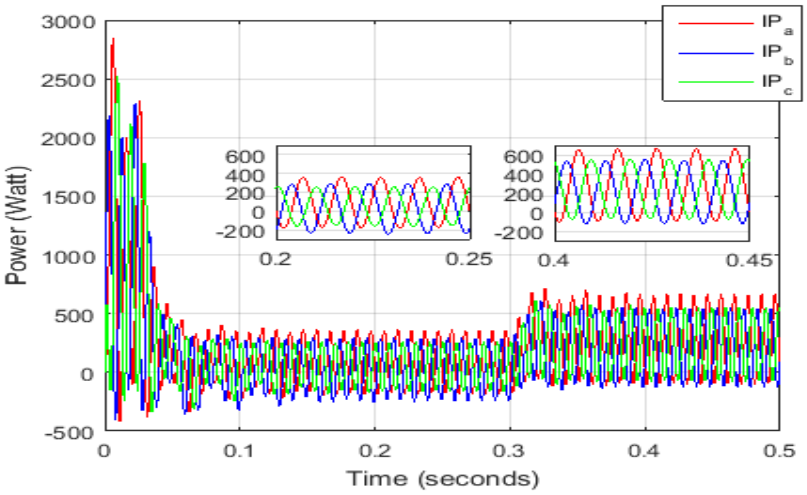

Figure 3.6: Simulation of *IP* (fault in phase a_s) under load torque ($c_r = 3.8\ Nm$)

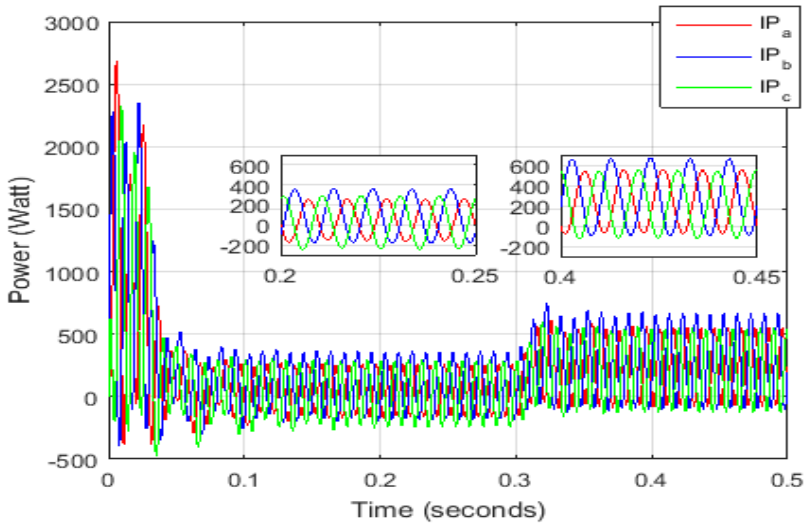

Figure 3.7: Simulation of *IP* (fault in phase b_s) under load torque ($c_r = 3.8\ Nm$)

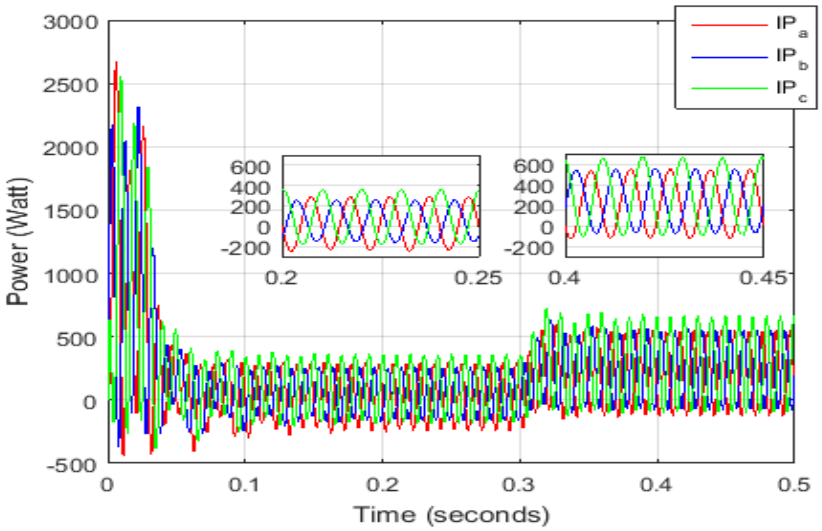

Figure 3.8: Simulation of *IP* (fault in phase c_s) under load torque ($c_r = 3.8\ Nm$)

The change in load torque in the preceding figures reveals another insight. Initially, in the first steady-state period (t=0.15 sec to t=0.3 sec), the motor exhibits a low average value of *IP*, previously justified by the motor's running power. Once the load torque reaches its rated value, the power undergoes a sudden change in its average value while maintaining the amplitude. This change is attributed to the necessary power to turn the motor under the new conditions. For a healthy motor, the values of instantaneous power have the same amplitude. The occurrence of a short circuit fault results in a change in amplitudes, with the damaged phase having a higher average value than the others.

3.2.2. Features extraction

FDC method utilizing artificial intelligence tools necessitate a dataset. This dataset is acquired through features extracted. Feature extraction is a process in which relevant information or characteristics (features) are identified and extracted from raw data (indicators). This is typically done to reduce the dimensionality of the data, highlight important patterns, and provide meaningful input for diagnosis algorithm. Therefore, using the entire *IP* signal seems unreasonable. Hence, the instantaneous power average on one period appears as a good feature to select. The calculation of the *IP* average is given by [48]:

$$IP_{(abc)} = \frac{1}{T_{ip}} \int_{t_0}^{t_0+T_{ip}} IP_{(abc)s}(t)\, dt \tag{3.2}$$

$$T_{ip} = 2 \times T_{sv} = \frac{2}{F}. \tag{3.3}$$

Where: F is the supply voltage frequency (50 Hz).

The variation of the average instantaneous power concerning the number of short-circuited turns under no-load conditions is depicted in Figure 3.9. [48]

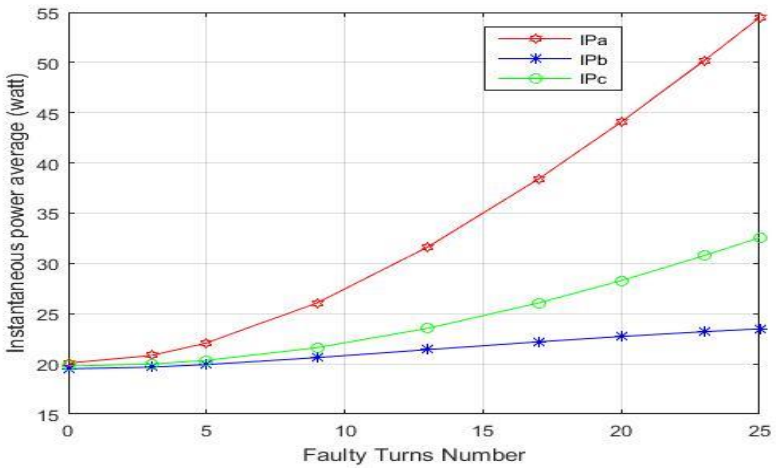

(a)

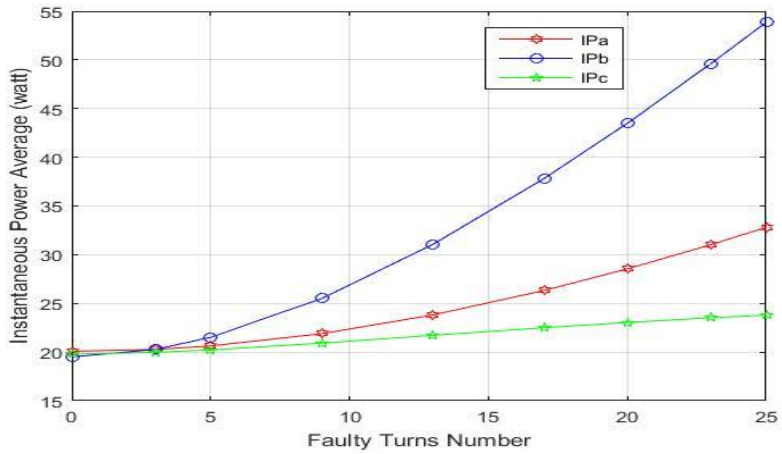

(b)

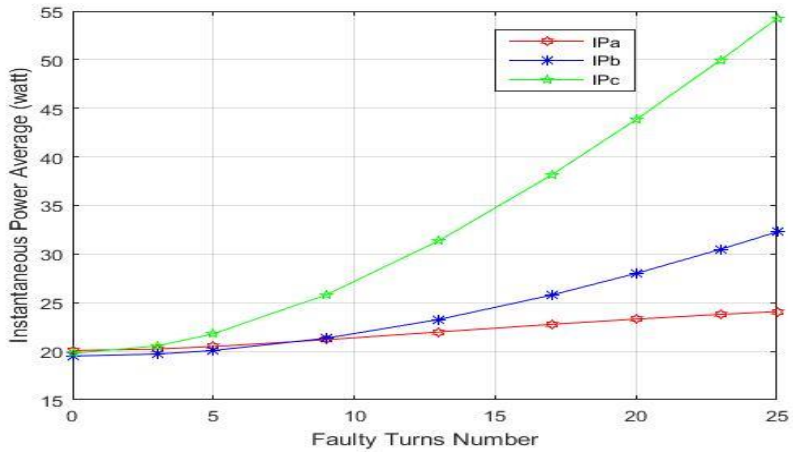

(c)

Figure 3.9: Instantaneous power average for SITSC fault on (a) phase a_s, (b) phase b_s, (c) phase c_s (no load conditions) [48].

The SITSC faults simulations are repeated with five load torque values (C_r=0%, C_r=10%, C_r=30%, C_r=70%, C_r=100%) of the fully load torque (C_r=3.8 N.m)), in order to investigate the load effect on the IPs average. Figure 3.10 illustrate the obtained results. [48]

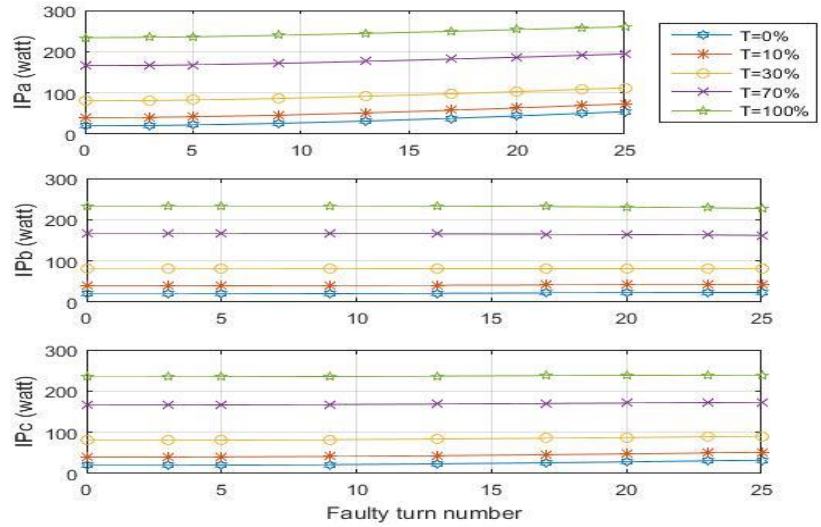

(a)

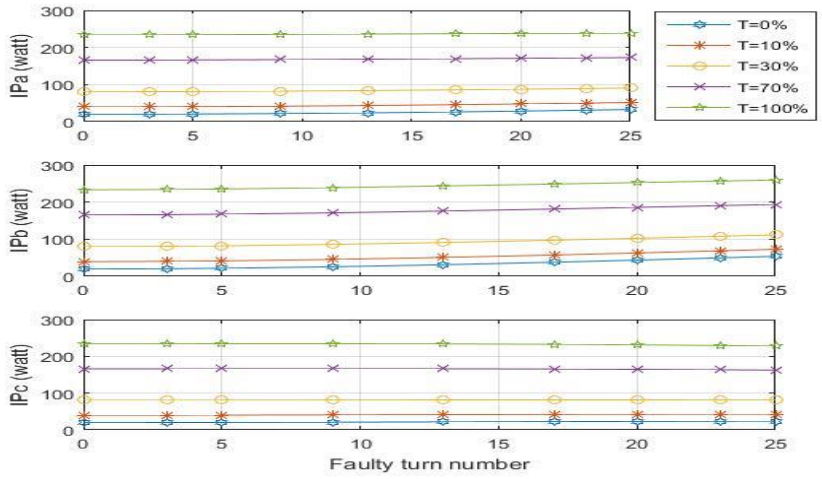

(b)

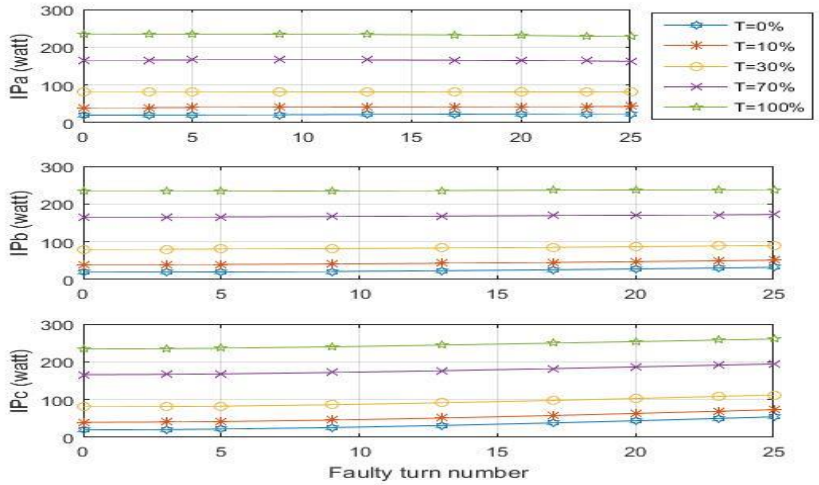

(c)

Figure 3.10: The three phase IP average under 4 load conditions, in case of SITSC fault on (a) phase a_s, (b) phase b_s, (c) phase c_s [48].

It is understandable from Figure 3.9 that the average values of three-phase IPs are correlated with the number of shorted turns. Additionally, the maximum *IP* value corresponds to the phase where the fault occurs. For example, if an SITSC fault occurs in phase a_s, the decreasing order of *IPs* is: IP_a-IP_c-IP_b. If an SITSC fault occurs in phase b_s, the decreasing order of IPs is: IP_b-IP_a-IP_c. If an SITSC fault occurs in phase c_s, the decreasing order of IPs is: IP_c-IP_b-IP_a. Moreover; as depicted in Figure 3.10, the average *IPs* of the faulty stator under various load conditions do not overlap. As result, the fault detection system is insensitive to load variations. According their favorable behavior against SITSC fault and load condition, we choose the three-phase stator instantaneous power averages (IP_a, IP_b, IP_c) as the greatest suitable inputs for the FF-NN.

3.2.3. Fault diagnosis approach

The primary objective of this study is to utilize ANN for the detection and localization of SITSC faults in Induction Motors (IMs). The IM model with SITSC fault, developed earlier, is simulated under various load-torque (0- 100%) levels and different percentages of shorted turns (0 - 10%). Currents and voltages are measured for all simulated cases at steady state. These signals are thoroughly explored and analyzed to identify representative indicators. The selected indicators are then used to extract distinctive features, namely (IP_a, IP_b and IP_c). These features serve as inputs for the proposed Feed Forward Neural Network (FF-NN) designed for Fault Detection and Classification (FDC) purposes.

To train and test the FF-NN, a dataset is required, which is obtained by collecting data under different percentages of SITSC fault, and load torque. The FF-NN is employed to correlate the extracted features with their corresponding affected phases. For the validation of the proposed FF-NN, a new dataset extracted from the experimental test bed is created to validate the diagnostic tool. Figure 3.11 illustrates the flowchart of the overall system.

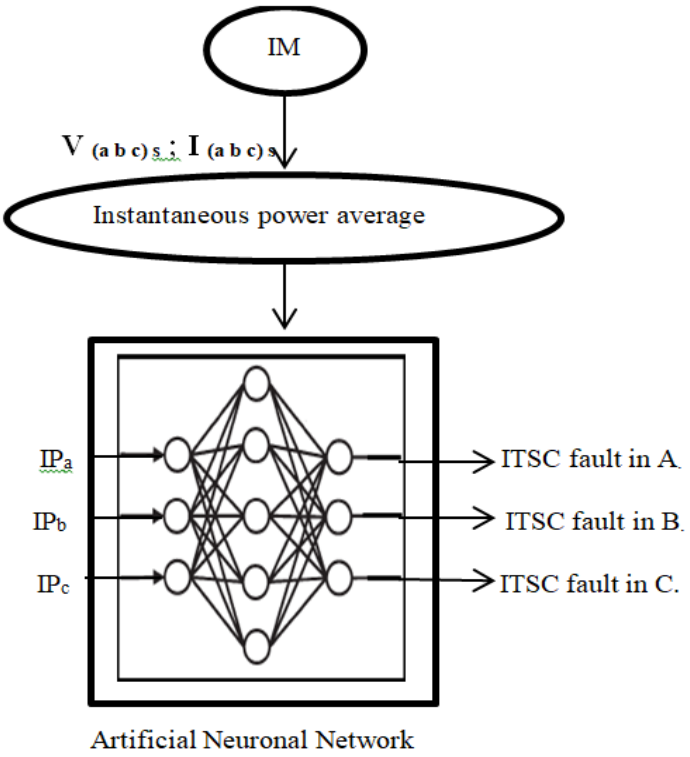

Figure 3.11: Block diagram of the proposed method. [48]

3.2.3.1. Feed forward neural network architecture and configuration

This study utilizes a FF-NN trained with the Levenberg–Marquardt backpropagation (BP) algorithm to automatically detect and locate ITSC faults. The ANN architecture comprises three layers; input layer consists of three neurons which correspond to the *IPs* values. The output layer consists of three neurons which correspond to the affected phase. Finally, the hidden layer consists of five neurons (see Figure 3.11). The activation functions for the hidden layer are "tansig". While the activation function of the output layers is "logsig". The selection of the number of neurons in the hidden layer is done through trial and error, as too few neurons may lead to undertraining, while too many neurons might result in memorization of the training set (overtraining). Both scenarios obstruct good generalization. The ANN is trained and subsequently tested with separate datasets to assess both training and testing errors.

3.2.3.2. Training and testing dataset

In the initial phase of this study, the induction motor models presented in the previous chapter were employed to generate simulation data under normal operating conditions and with varying levels of SITSC fault. The collected data enabled the calculation of *IP*

averages and the creation of datasets for training and testing the Artificial Neural Network (ANN).

To enhance the network's generalization ability, training and testing data were encompassed to cover the complete spectrum of operating conditions. This included various fault occurrences and healthy operations under different load torques [48]. The training dataset was constructed to include different operating scenarios of the induction motor: 'healthy' (one point), faults with (n=3, 5, 9, 13, 17, 20, 23, 25) shorted turns on each stator phase (24 points), and load torque variations of (0%, 10%, 30%, 70%, 100% of the rated load torque). This resulted in a dataset comprising 125 points. The testing dataset included faults with (n=4, 8, 10, 14, 18, 22) shorted turns on each stator phase (18 points) and load torque variations of (20%, 40%, 80%, 90% of the rated load torque), making the dataset consist of 72 points.

3.2.4. Results and discussion

3.2.4.1. Simulation results

The performance of the ANN is assessed by its Mean Squared Error (MSE), as depicted in Figure 3.12. Remarkably, after only sixty-four epochs of learning, the network achieves a low training MSE, equal to 6.6891×10^{-12}. Figure 3.13 illustrates the desired output, training outputs. The training results are highly conclusive; the ANN effectively learns the training data by reproducing the desired outputs with minimal training errors. The generalization capacity of the trained network is assessed using the test dataset, as depicted in Figure 3.14. The test results affirm that the ANN-based method effectively detects SITSC faults in each of the three phases.

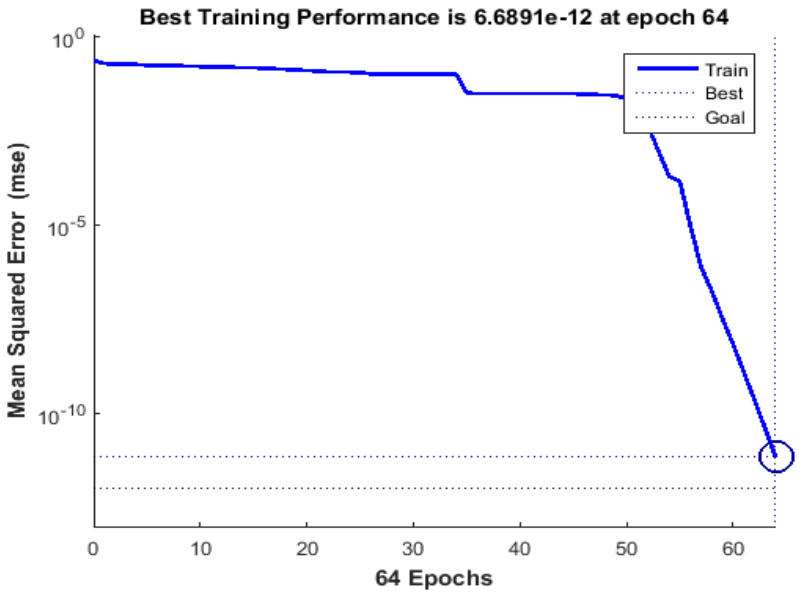

Figure 3.12: Training performance of the neuronal network.

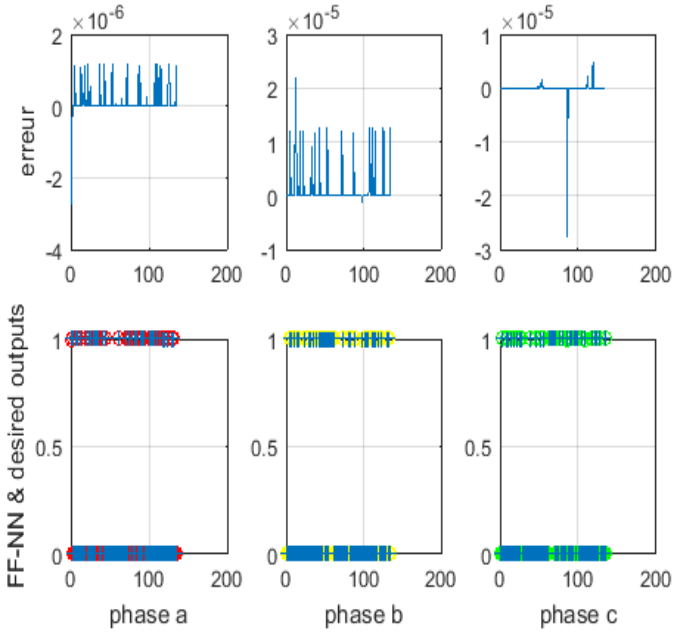

Figure 3.13: Training errors, training & desired outputs.

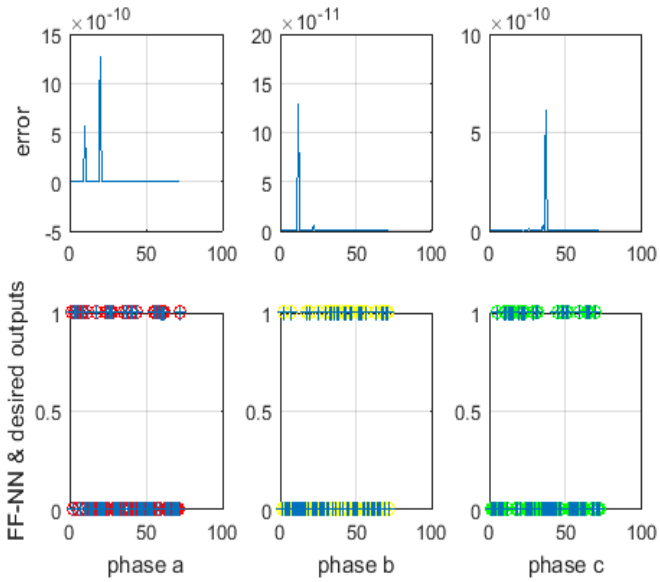

Figure 3.14: Testing errors, testing & desired outputs.

3.2.4.2. Experimental results

In order to validate the proposed FDC technic, experimental tests were conducted for the diagnosis of SITSC in the IM. The three-phase squirrel cage induction motor used in Laboratory has the same parameters as that of the simulated model (see chapter 2, table 2.1) [48]. The validation of the ANN is discussed, by using the real motor under healthy operation as well as in presence of SITSC fault.

The SITSC faults appear in the whole three phases of the stator. The validation dataset composed of fifty-one samples. One healthy case and fifty combined faults occurrence, the shorted turns vary as (6, 24, 30 turns) for each phase. And the variation of the load torque is taken into account. The results of the validation are shown in Figure 3.15.

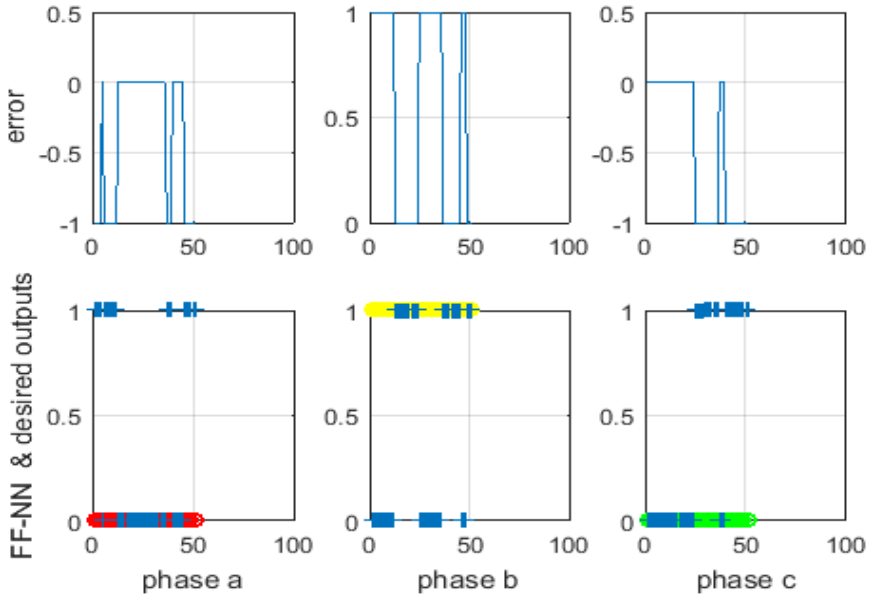

Figure 3.15: Validation errors, FF-NN & desired outputs.

As it can be observed in figure 3.15, The ANN has recognized more than 90% of the cases. In phases a_s and b_s the FF-NN recognize 91% of the cases, in phase c_s the ANN did recognize 95% of the cases.

3.3. Detection, classification and severity estimation of SITSC and USV faults

IMs undergo various stresses that can disrupt their normal operation. Excessive stress can exhibit symptoms before the IM faces a failure situation. Therefore, detecting these symptoms early allows for shutting down IMs to prevent complete destruction. Fault detection is a primary objective of diagnosis systems, and SITSC is a significant cause of IM breakdown. However, unbalanced supply voltage is a contributing factor affecting IMs' operation. To avoid false alarms caused by USV, the diagnosis system must distinguish between USV and SITSC faults. The training, testing, and validation phases of the MLP-NN require dataset creation, and the necessary data is obtained from the developed model and the laboratory test-bed (Chapter 2). The results demonstrate the sensitivity and effectiveness of the proposed diagnosis system.

3.3.1. Fault indicators selection

In this section, three types of indicators obtained from time domain current and voltage signals where selected to do the diagnosis purpose.

3.3.1.1. phase shift between line current and phase voltage analysis

To calculate the phase shift between current and voltage signals, it is necessary to estimate the zero time (*ZT*) of each signal. Subsequently, determine the zero crossing time (*ZCT*) between them, and finally, convert the *ZCT* values from seconds to degrees. Figure 3.16 illustrates how to calculate an approximate zero crossing point, and equation (3.4) provides its expression.

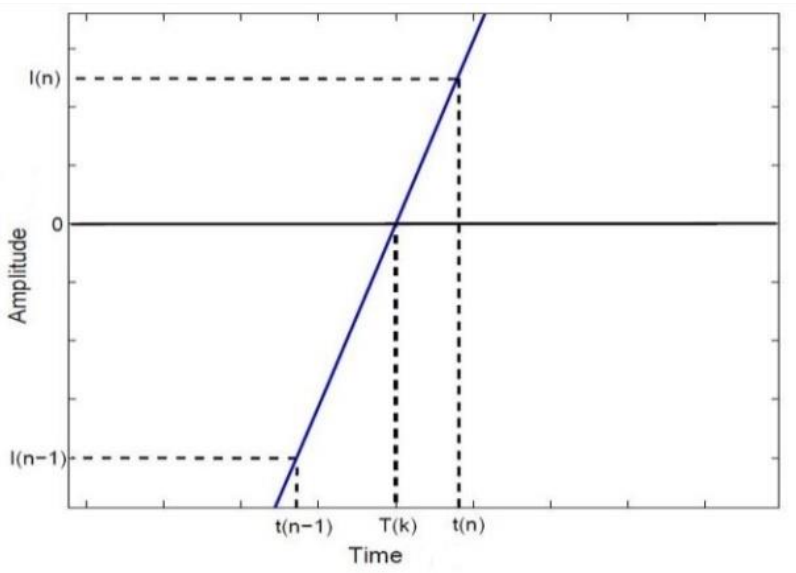

Figure 3.16: Approximate zero time calculation method

The ZT is given as follows:

$$\frac{I(n)-0}{I(n)-I(n-1)} = \frac{t(n)-T(k)}{t(n)-t(n-1)} \tag{3.4}$$

The approximate $T(k)$ is defined as:

$$T(k) = t(n) - \frac{I(n)[t(n)-t(n-1)]}{I(n)-I(n-1)} \tag{3.5}$$

So, ZCT between current and voltage signals is defined as :

$$ZCT_{abc} = ZCTv^{s}_{abc} - ZCTi^{s}_{abc} \tag{3.6}$$

Where: $ZCTv^{s}_{abc}$ are the stator voltages zero crossing times in phases a_s, b_s and c_s.

$ZCTi^{s}_{abc}$ are the stator currents zero crossing times in phase a_s, b_s and c_s.

Finally; phase shift is calculate as:

$$\varphi_{abc} = \frac{ZCT_{abc}}{T} \times 360 \tag{3.7}$$

Where T is the period of the supply voltage ($T = \frac{1}{f} = \frac{1}{50} = 0.02\ sec$)

Simulation results for the three-phase shift between line current and phase voltage in healthy and faulty cases are shown in Figures from 3.17 to 3.21.

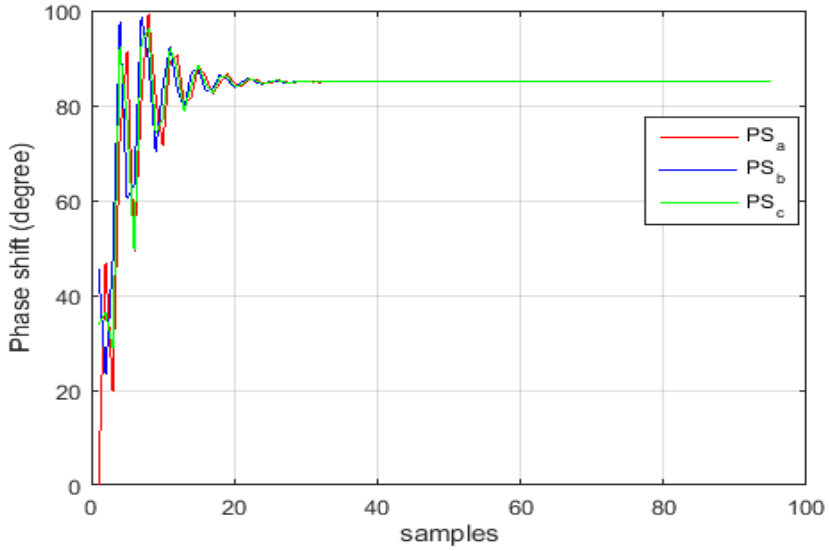

Figure 3.17: Simulation of $PS_{(abc)}$ (healthy case)

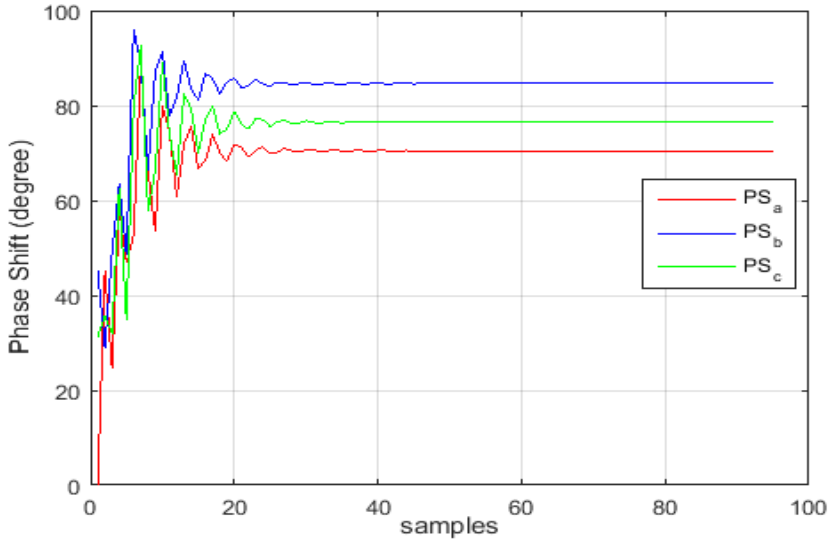

Figure 3.18: Simulation of $PS_{(abc)}$ (fault in phase a_s)

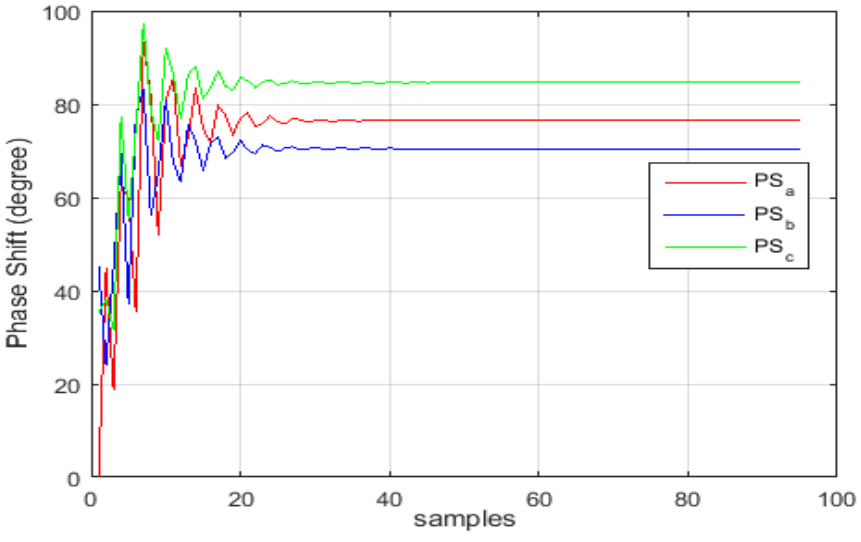

Figure 3.19: Simulation of $PS_{(abc)}$ (fault in phase b_s)

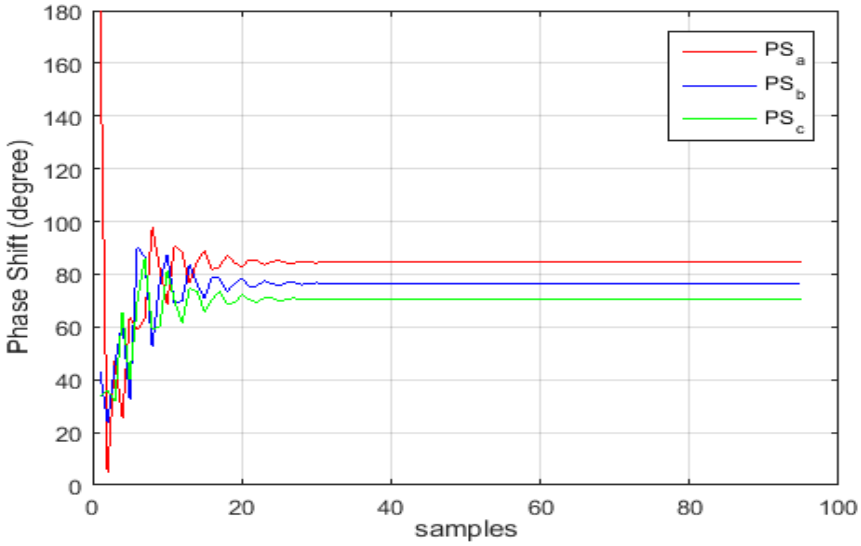

Figure 3.20: Simulation of $PS_{(abc)}$ (fault in phase c_s)

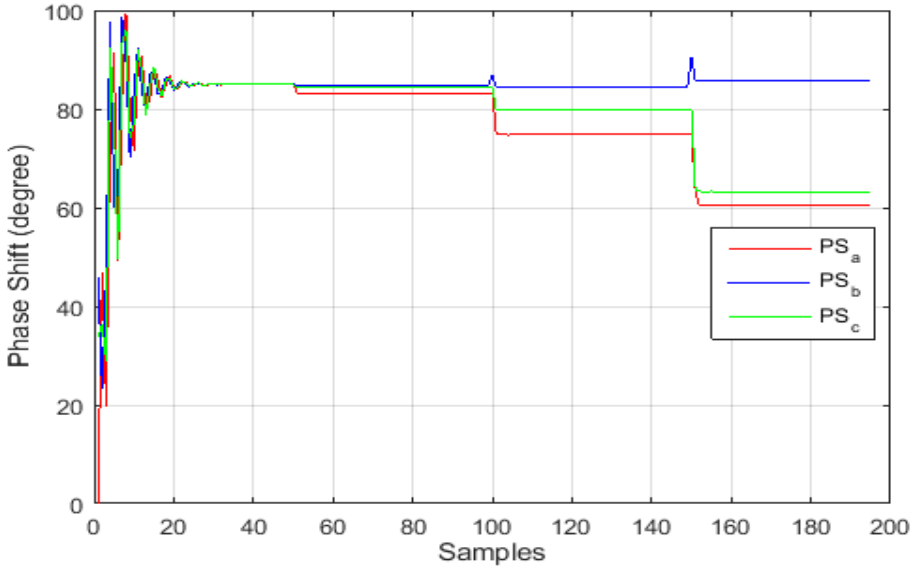

Figure 3.21: Simulation of $PS_{(abc)}$: healthy case, (*t=0.5)* 10 shorted turns in a_s, (*t=1 sec)* 20 shorted turns in a_s, (*t=1.5 sec)* 40 shorted turns in a_s.

In the transient regime, the values of the *PS* are unstable because the current and voltage signals are also in the transitional regime. In the steady-state, the *PS* takes on a constant value. In the case of a healthy motor, the three *PS* values are equal (*PS=85 degrees*). The occurrence of a SITSC fault brings a change, where the faulty phase takes the smallest value of *PS*, and this value decreases as the level of SITSC increases.

Load torque variation in one of the motor functioning conditions. It influences on the currents, consequently on phases shift. Therefore, analyzing it is very important to see whether it can disturb the diagnosis process by given faulted calculation of SITSC

percentage or not. Figure from 3.22 to 3.25 illustrate the *PS* signals under no load condition, then a load condition application at *t=0.5s* where $c_r = 3.8\ Nm$.

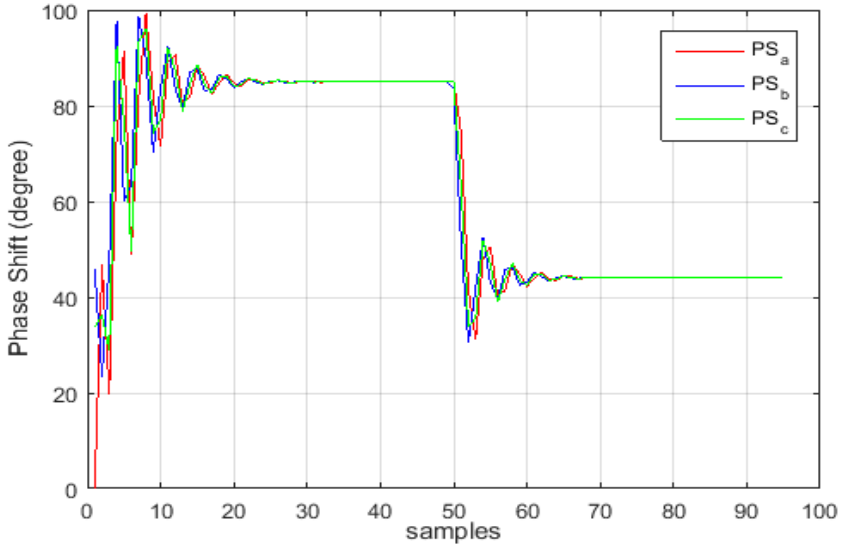

Figure 3.22: Simulation of $PS_{(abc)}$ (healthy case) under load torque ($c_r = 3.8\ Nm$)

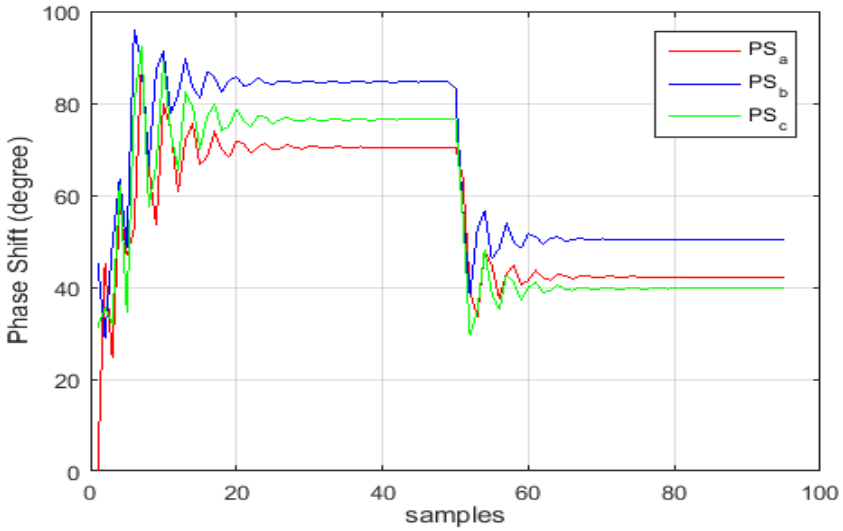

Figure 3.23: Simulation of $PS_{(abc)}$ (fault in phase a_s) under load torque ($c_r = 3.8\ Nm$)

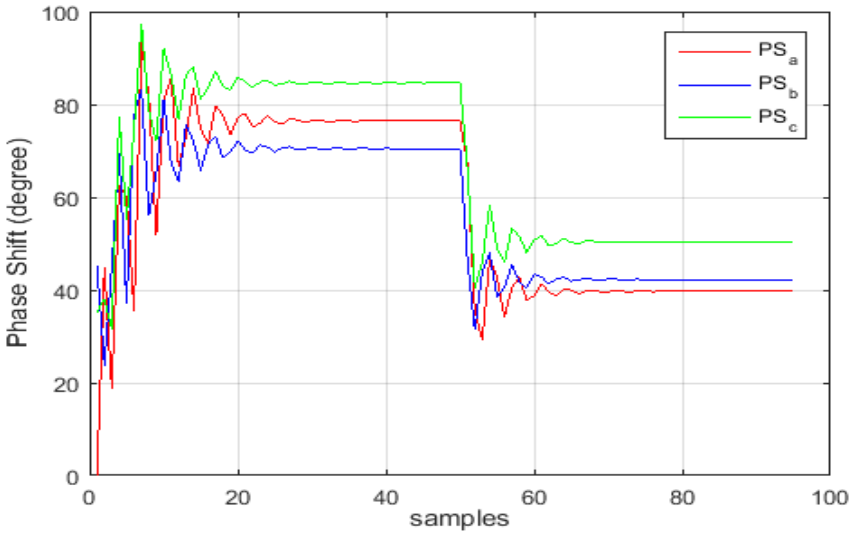

Figure 3.24: Simulation of $PS_{(abc)}$ (fault in phase b_s) under load torque ($c_r = 3.8\ Nm$)

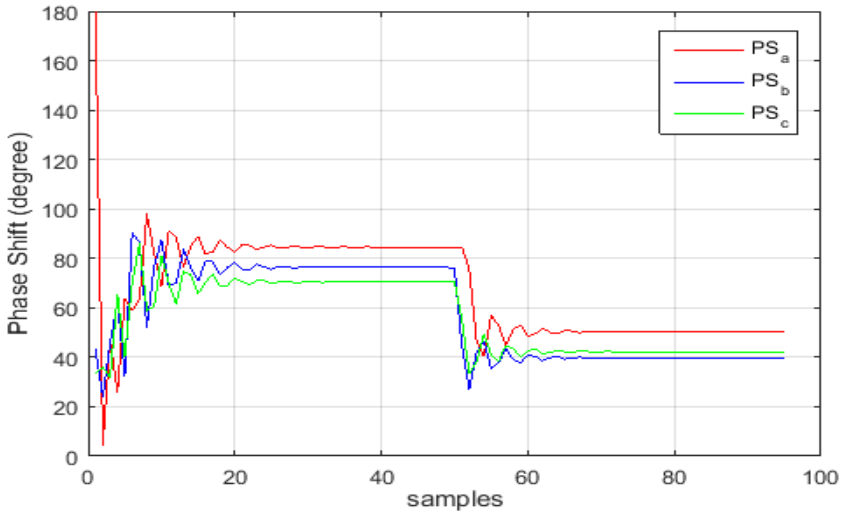

Figure 3.25: Simulation of $PS_{(abc)}$(fault in phase c_s) under load torque ($c_r = 3.8\ Nm$)

An increase in the load torque affects the *PS* by decreasing its value. For a healthy motor case, the values of the *PS* decrease until *PS*=45 degrees. In the event that the motor faces a short circuit fault; the same reasoning holds, the damaged phase is the one with the lowest value of *PS*.

In order to explore the impact of USV on the *PS*. The IM model has been simulated under USV conditions, the results are illustrated figures from 3.26 to 3.29.

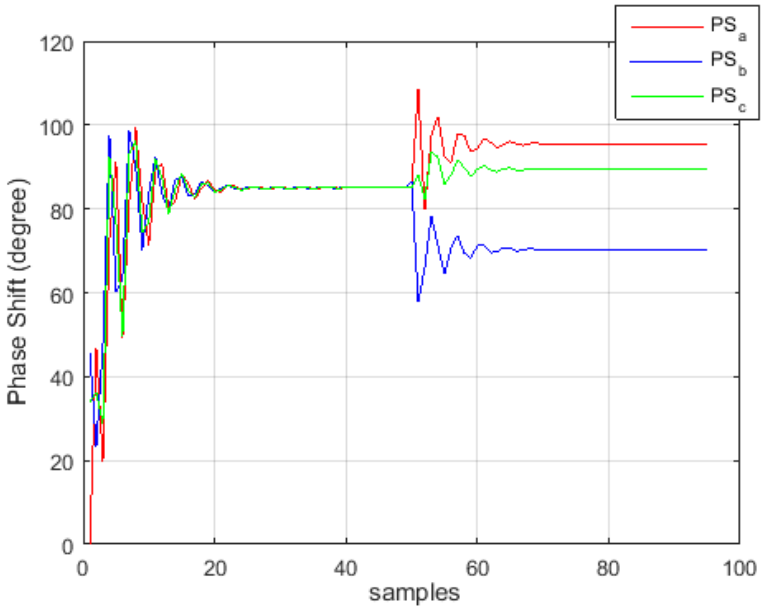

Figure 3.26: Simulation of healthy IM $PS_{(abc)}$ under USV in phase a_s.

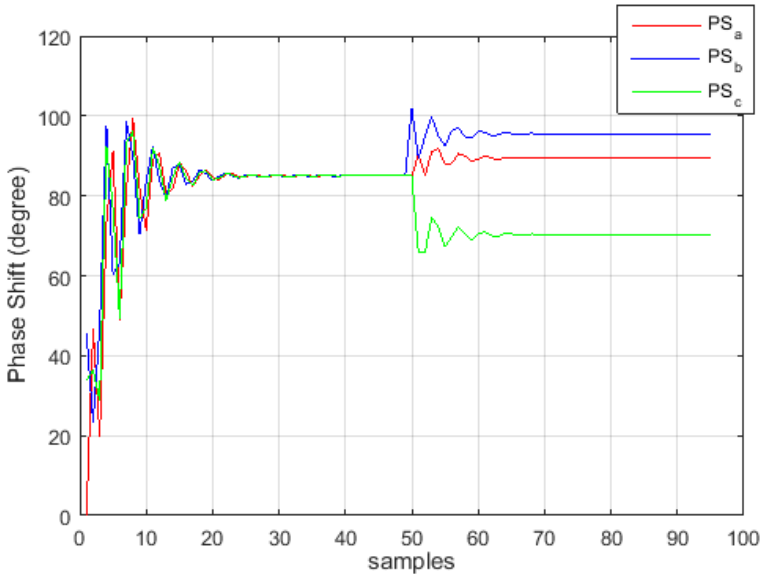

Figure 3.27: Simulation of healthy IM $PS_{(abc)}$ under USV in phase b_s.

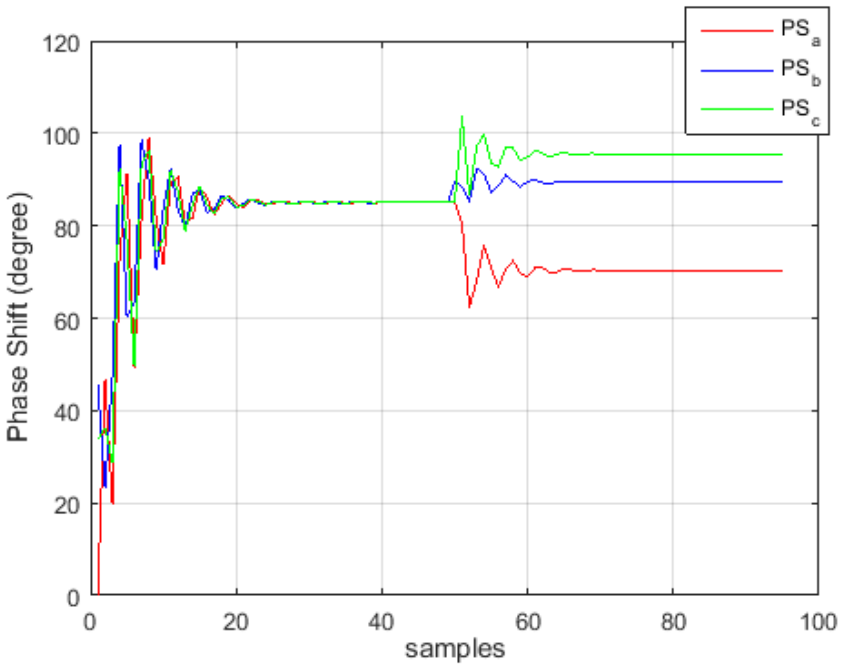

Figure 3.28: Simulation of healthy IM $PS_{(abc)}$ under USV in phase c_s.

Oppositely to the SITSC effect on the phase shifts, the damaged phase is the one with highest value of *PS*. we can explain that by the fact that the phases voltage are not the same, where the damaged one has a lowest amplitude of voltage.

3.3.1.2. Total instantaneous power analysis

In an induction motor supplied from an ideal three-phase source, the currents and voltages of the three phases are given as:

$$v^s_{abc} = \begin{cases} v^s_a = \sqrt{2}\,V\cos(\omega t) \\ v^s_b = \sqrt{2}\,V\cos(\omega t + 2\pi/3) \\ v^s_c = \sqrt{2}\,V\cos(\omega t - 2\pi/3) \end{cases} \quad i^s_{abc} = \begin{cases} i^s_a = \sqrt{2}\,I\cos(\omega t - \varphi) \\ i^s_b = \sqrt{2}\,I\cos(\omega t + \frac{2\pi}{3} - \varphi) \\ i^s_c = \sqrt{2}\,I\cos(\omega t - \frac{2\pi}{3} - \varphi) \end{cases} \tag{3.8}$$

Where: I and V are respectively the root mean square (*RMS*) values of the fundamental component of the current and voltage. φ is the phase shift between current and voltage, ω is the supply frequency in radians per second.

In a healthy motor, the total instantaneous power (*TIP*) is given by[51] equation (3.9):

$$TIP(t) = \sum v^s_{abc}(t) i^s_{abc}(t) = 3VI\cos(\varphi) = P_0. \tag{3.9}$$

In the case of a SITSC occurrence, the *TIP* equation changes where an expression define fault is being added. [21] has developed the TIP equation and gives it as follows:

$$TIP(t) = P_0 + TIPf(t) \tag{3.10}$$

Where:

$$TIPf(t) = 3V(I_l\, cos[\omega_{osc}t - \varphi_l] + I_r\, cos[\omega_{osc}t - \varphi_r]) \tag{3.11}$$

I_l is the *RMS* value of the lower side-band current component, I_r is the *RMS* value of the upper side-band current component, ω_{osc} is the modulating frequency, φ_l and φ_r are the current left and right phase shift respectively.

Simulation results for the total instantaneous power in healthy and faulty cases and under USV and load torque variations are shown in Figures 3.29 and 3.30.

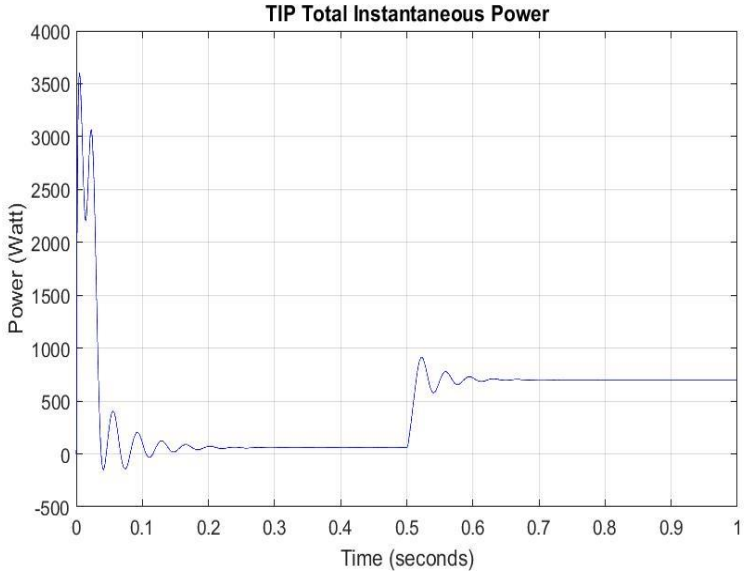

Figure 3.29: Healthy motor instantaneous power under load torque conditions [51].

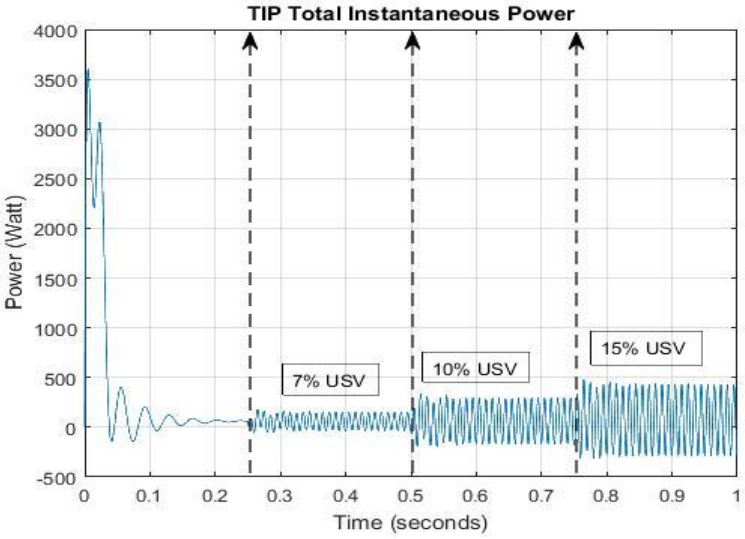

Figure 3.30: Healthy motor instantaneous power under USV [51].

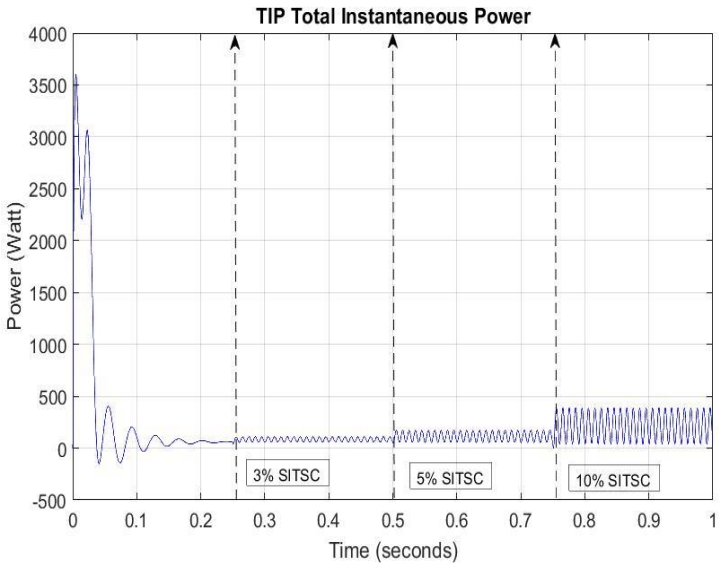

Figure 3.31: Total instantaneous power for one faulty phase [51].

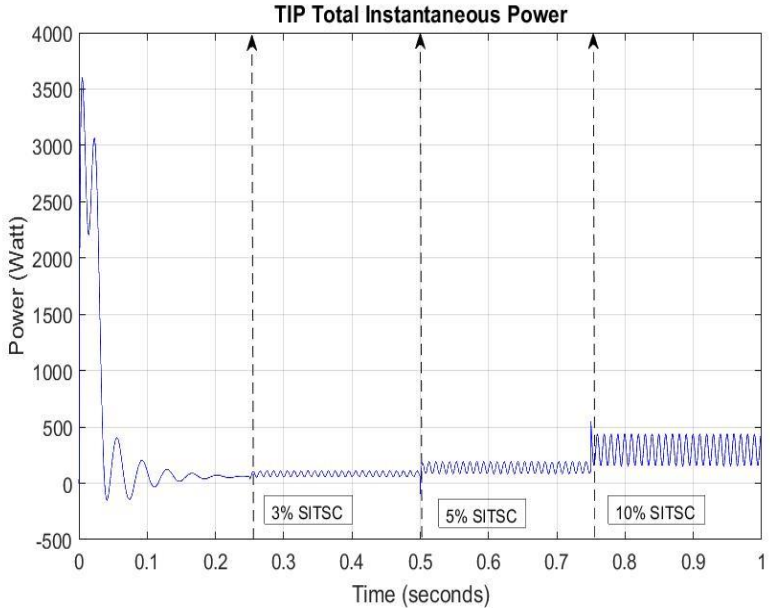

Figure 3.32: Total instantaneous power for three faulty phases [51].

Figure 3.29 illustrates that in the case of a healthy IM, the TIP maintains a low, constant value, attributed to IM losses (iron losses and joule losses). Application of a load causes the TIP to quickly increase until it reaches the rated TIP. In Figure 3.30, the TIP value remains constant. However, in the presence of an USV fault, the TIP signal exhibits ripples around the constant low value. The amplitude of these ripples amplifies with the developing of USV fault severity. The occurrence of SITSC fault (as depicted in Figures 3.31 and 3.32) induces undulations in the TIP signal. The amplitude of these undulations increases proportionally with the fault severity. Moreover, the average TIP value fluctuates with changes in the SITSC percentage.

3.3.1.3. Sequence Component analysis

In 1918, Fortescue proposed a transformation that decomposes any unbalanced system into three balanced ones [49]. Therefore, this transformation is used to convert unbalanced supply voltage (USV) into three sets of symmetrical balanced supply voltage components, namely positive, negative, and zero sequence components. This transformation is defined by:

$$\begin{bmatrix} PSV \\ NSV \\ ZSV \end{bmatrix} = \frac{1}{3}\begin{bmatrix} 1 & a^2 & a \\ 1 & a & a^2 \\ 1 & 1 & 1 \end{bmatrix} . \begin{bmatrix} v_a^s \\ v_b^s \\ v_c^s \end{bmatrix} \quad (3.12)$$

Where: $a = e^{j2\pi/3}$, v_a^s, v_b^s and v_c^s are the three-phase supply voltages.
PSV, NSV, and ZSV are successively the positive, negative, and zero sequence voltages.

If the supply voltage is balanced, only the positive sequence exists, and other components (negative & zero) are equal to zero. The appearance of USV fault causes an increase in the NSV value. Figure 3.33 shows the evaluation of the symmetrical components of a healthy supply voltage, then a USV occurrence in phase a_s at 0.2 sec, this USV increases from 5% to 15%.

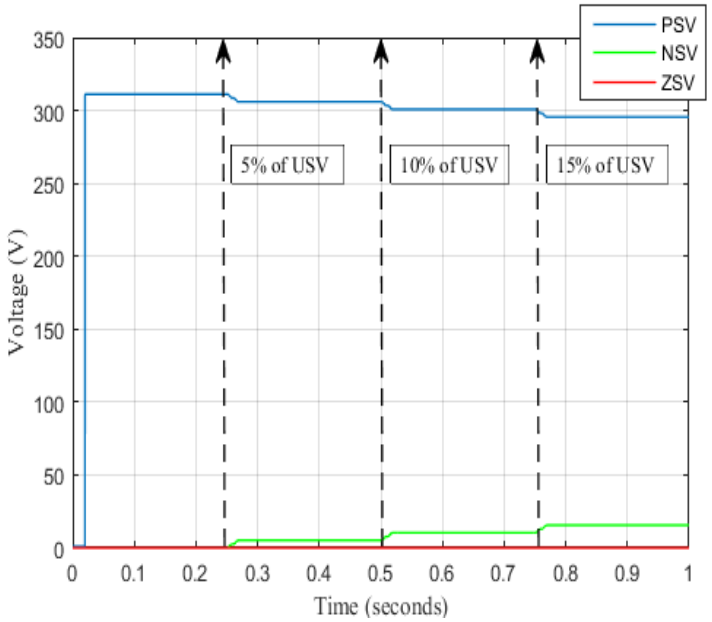

Figure 3.33: Sequence component simulation under: (*t=0.2 sec*) 5% of USV, (*t=0.5 sec*) 10% of USV, (*t=0.75 sec*) 15% of USV. [51].

Figure 3.33 demonstrates that as the USV increases, the NSV also increases, while the PSV decreases. Meanwhile, the ZSV remains constant at zero. It's noteworthy that the occurrence of a SITSC fault and the application of a load charge do not affect the sequence

components; this is because the sequence components are associated with the motor itself, however the USV is linked to the power supply voltage.

3.3.2. Features extraction

The proposed MLP-NN-based diagnosis system requires a dataset, which is acquired through feature extraction. Feature extraction is a process in which relevant information is identified and extracted from raw data indicators. This is done to reduce the dimensionality of the data by capturing important patterns and providing meaningful input for the diagnosis process. Therefore, using the entire signals of indicators seems unreasonable. Hence, averaging, maximum, and minimum values over one period sound like a good solution to select features.

3.3.2.1. Three phase shift between current and voltage

According to figures from 3.17 to 3.30, the transient regime contains non-equal values of the *PS*. However, the steady-state regime provides a fixed value of the *PS*, and it is this value that we will consider for this diagnosis approach.

To study the behavior of *PS* under SITSC fault, the IM model is simulated at no load torque for various percentages of SITSC (SITSC= 0%, 2%, 4%, 6%, 8% and 10%) and various percentages of USV (USV= 0%, 2%, 3%, 5%, 7%, 10% and 15%) in the three phases. The results are illustrated in Figures 3.34 and 3.35. To observe the effect of load torque variation on *PS*, the IM model is simulated at three load torque levels (0%, 50%, 100% of full load) and under the same percentages of SITSC fault and USV. The results are summarized in Figures 3.36 and 3.37.

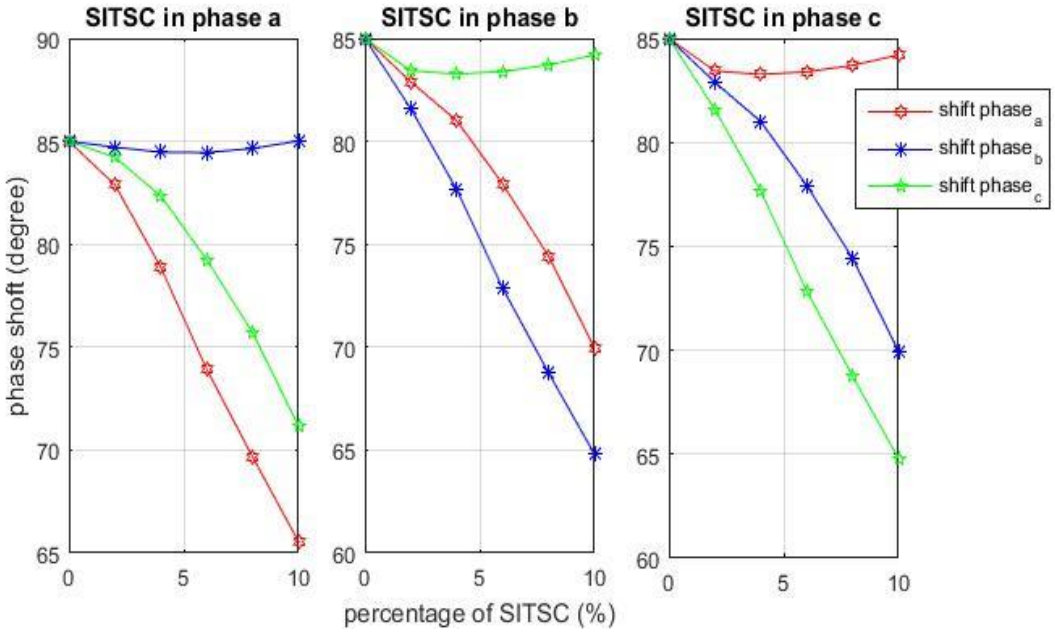

Figure 3.34: *PS* evaluation as function of SITSC percentages

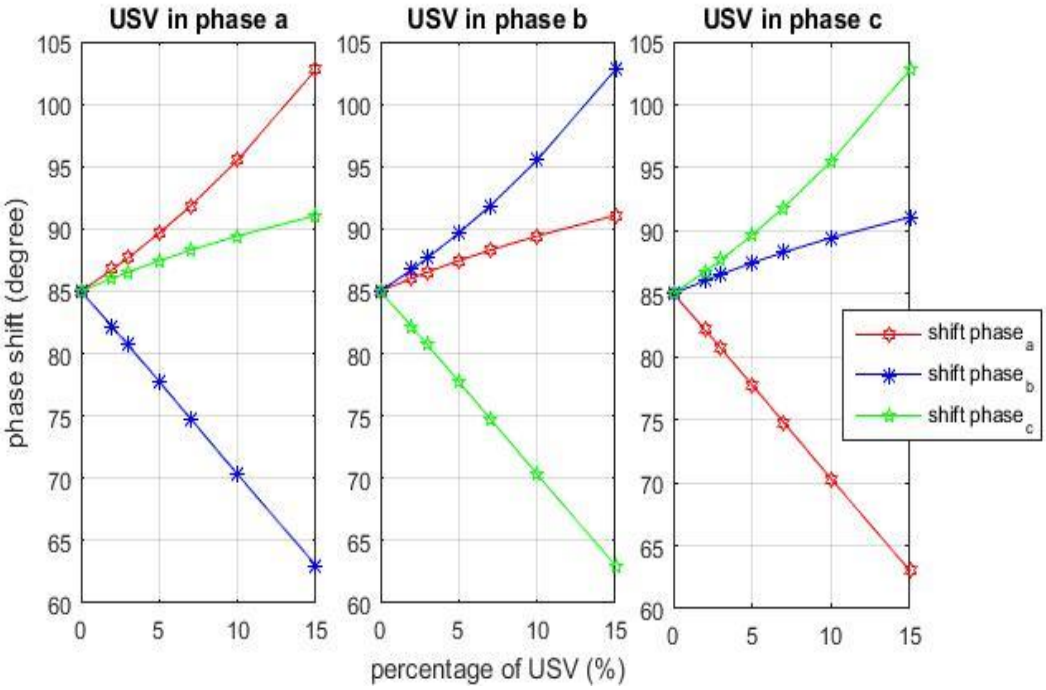

Figure 3.35: *PS* evaluation as function of USV percentages

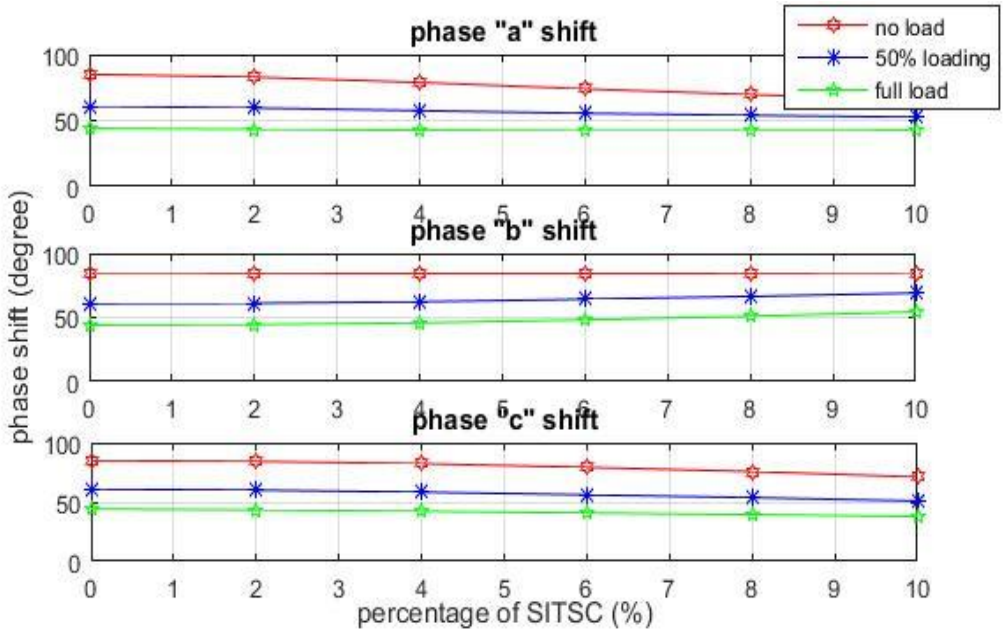

Figure 3.36: *PS* evaluations as function of SITSC percentages and load condition.

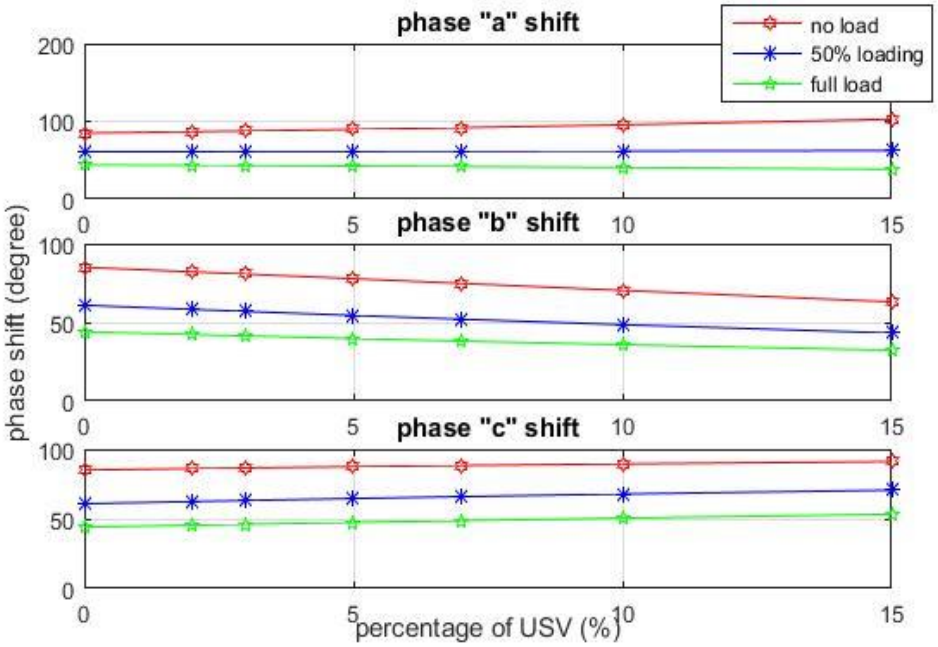

Figure 3.37: *PS* evaluations as function of USV percentages and load condition.

From Figure 3.34, it is clear that as the SITSC percentage increases, the smallest PS value regresses in the damaged phase, while the PS values in the other phases increase. Conversely, in Figure 3.35, as the USV percentage increases, the largest PS value reverts to the unbalanced phase, while the others decrease. Particularly, the load torque does not significantly impact the system; as depicted in Figures 3.36 and 3.37, variations in load torque do not overlap with changes in PS indicators, ensuring the diagnosis system remains unaffected by load variations.

3.3.2.2. The minimum, maximum and average of the total instantaneous power

In this diagnosis approach; the statistical characteristics of the *TIP* signal (minimum, maximum and average) were selected as the powerful features of this indicator. To study the behavior of the statistical features under SITSC fault and USV, the IM model is simulated at no load torque for different percentages of shorted turns (0%, 2%, 4%, 6%, 8%, 10% of the total turns) and different percentages of USV (0%, 2%, 3%, 5%, 7%, 10%, and 15%). The obtained results are summarized in Figures 3.38 and 3.39. To observe the effect of load torque variation on these features, the IM model is simulated at three load torque levels (0%, 50%, 100% of the full load) and under the same percentages of SITSC fault and USV previously used. The results are summarized in Figures 3.40 and 3.41.

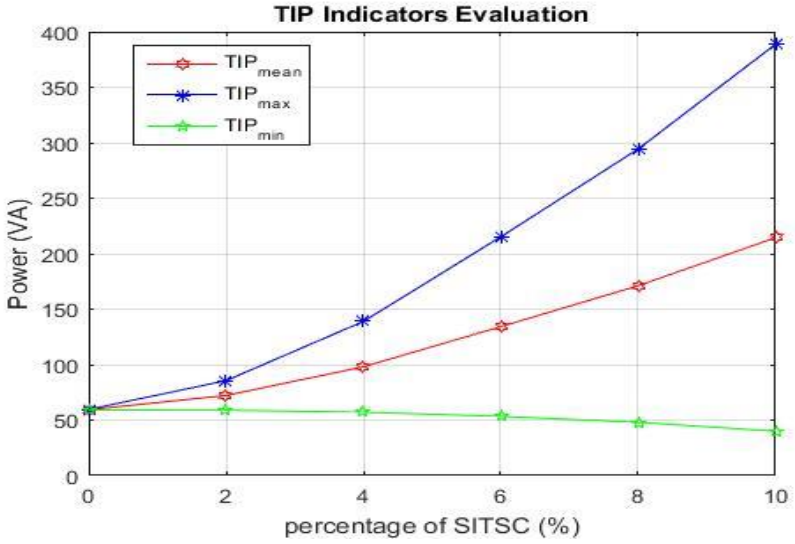

Figure 3.38: *TIP* features evaluation as function of SITSC percentages.

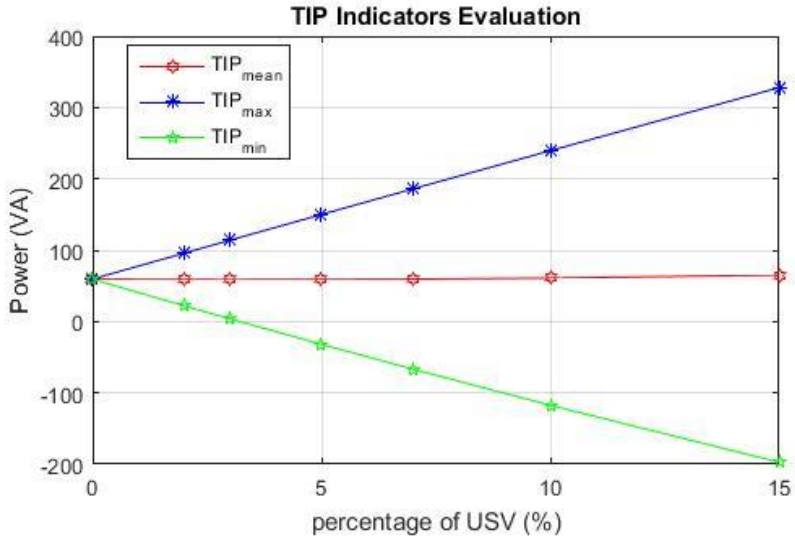

Figure 3.39: *TIP* features evaluation as function of USV percentages

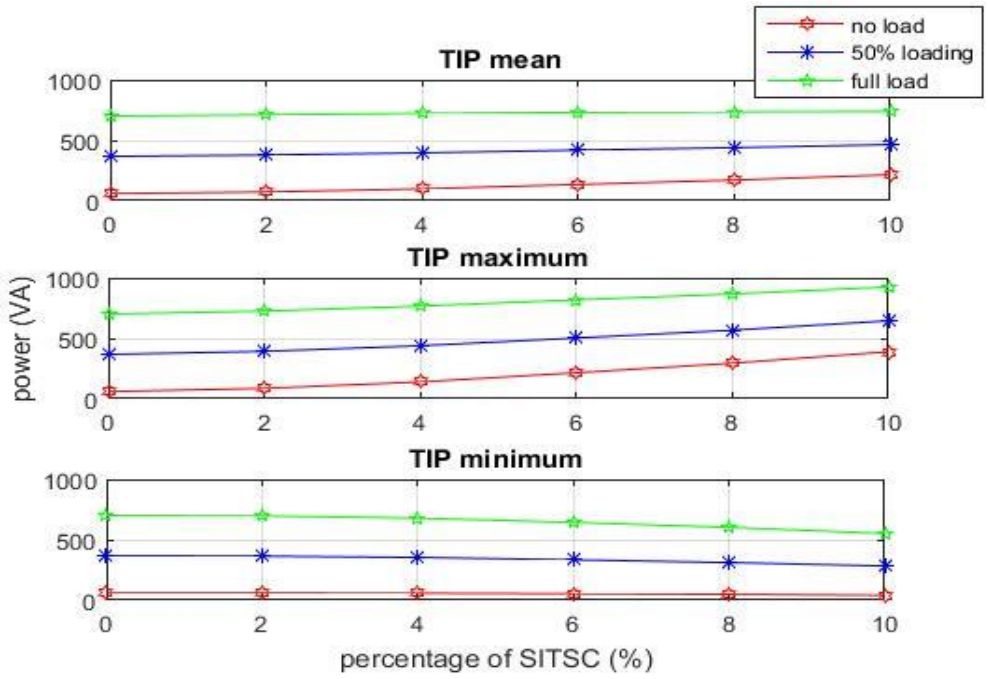

Figure 3.40: *TIP* features evaluation as function of SITSC percentages and load condition.

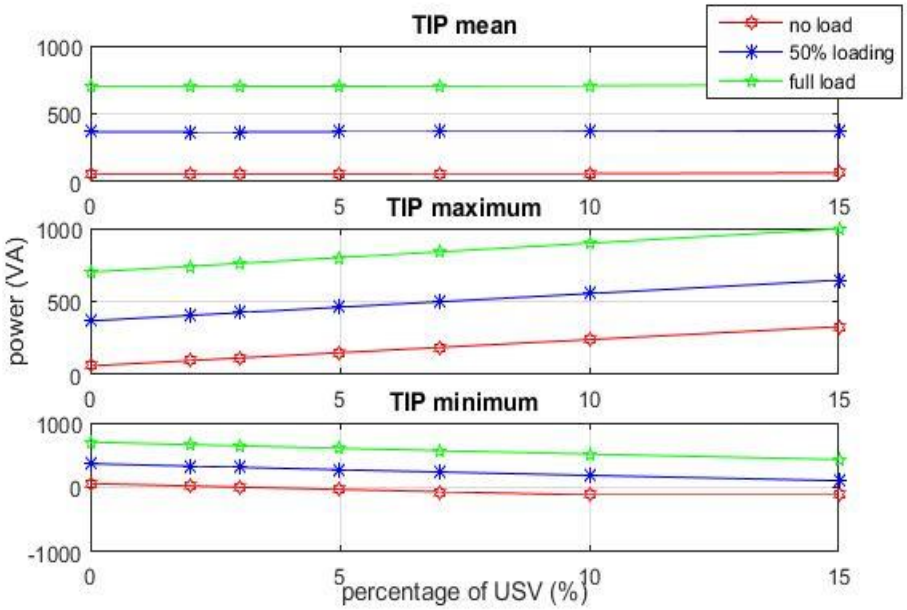

Figure 3.41: *TIP* features evaluation as function of USV percentages and load condition.

Figures 3.38 and 3.39 reveal that with increasing severity of SITSC faults and USV, the TIP_{max}, TIP_{min}, and TIP_{mean} values diverge from each other. This enlargement gap is a result of the undulations observed in the TIP signal, corroborating the findings from Figures 3.30 and 3.32. Furthermore, in Figures 3.40 and 3.41, the progression of selected

indicators across various load torque levels remains distinct, indicating that the proposed diagnosis system remains insensitive to variations in load torque.

3.3.2.3.Negative sequence voltage

The occurrence of a SITSC will not affect the NSV component, since the USV is a primary influencer of NSV changes. Therefore, in this study we chose the *NSV* as the appropriate feature to indicate the occurrence of a supply voltage unbalance. Figure 3.42 illustrates the evaluation of the *NSV* component as a function of the percentages of USV in the three phases. This figure is employed to investigate the behavior of the negative sequence when unbalanced supply voltage appears in the three phases.

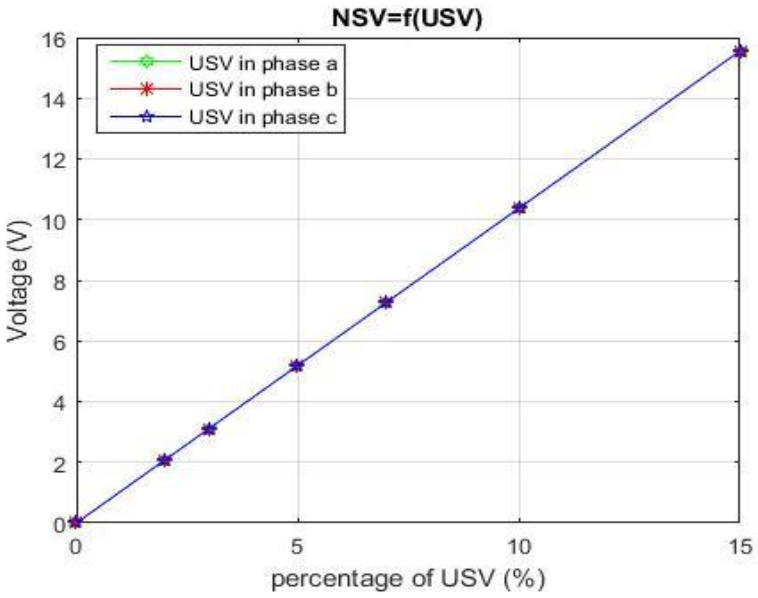

Figure 3.42: *NSV* evaluations as function of USV percentages.

In Figure 3.42, it's evident that the amplitude of the NSV displays a linear dependence on the level of the USV. Additionally, when a USV occurs in phases A, B, or C, the NSV values are identical (as indicated by the superimposed curves). This equality can be clarified by Equation 3.12 of the sequence component. Meanwhile the USV predominantly induces changes in NSV; the NSV factor serves as an indicator for detecting the presence of supply voltage unbalance.

3.3.3. Fault identification approach

The key objective of this study is to employ ANNs for the detection, classification and severity estimation of SITSC in IMs. The previously developed IM model with SITSC

faults is simulated under various percentages of SITSC (0 - 10%) and different load-torque levels (0 - 100%). Currents and voltages are measured for all simulated cases at steady state. These signals are thoroughly explored and analyzed to identify representative indicators. The selected indicators, namely PS, TIP and sequence component are then used to extract distinctive features. These features are PS average, statistical characteristics of TIP and NSV. Those features serve as inputs for the proposed multi-layer perceptron neural network (MLP-NN) designed for Fault detection, classification and severity estimation purposes [51].

MLP-NN is employed to correlate the extracted features with their corresponding SITSC percentages and USV occurrence. For the validation of the proposed FF-NN, a new dataset extracted from the experimental test bed is created to validate the diagnostic tool. Figure 3.43 illustrates the flowchart of the overall system

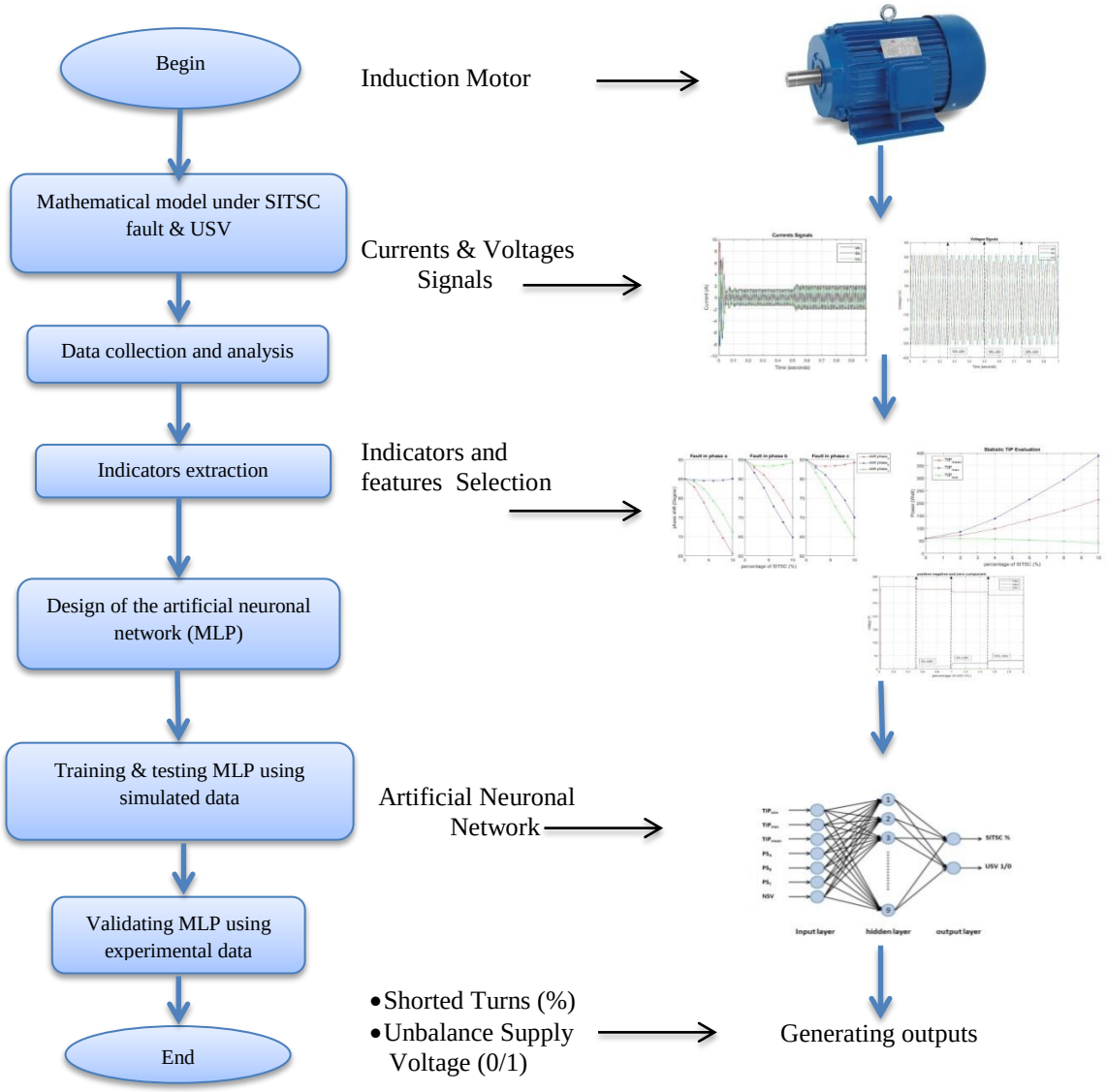

Figure 3.43: Flowchart of the diagnostic system [51].

3.3.3.1. MLP-NN design and parameters configuration

In this study, Multi-Layer Perceptron Neural Network (MLP-NN) is explored as a complementary component to enhance the IM diagnostic system. The MLP-NN architecture consists of an input layer, one hidden layer, and one output layer [51]. Figure 3.44 illustrates the structure of the designed MLP. Based on the analysis of fault indicators in the previous section:

- The input layer comprises seven neurons (TIP_{min}, TIP_{max}, TIP_{mean}, PS_a, PS_b, PS_c, and NSV).
- The hidden layer includes nine neurons, determined as optimal for the network's accuracy through trial and error.
- The output layer consists of two neurons: one for indicating the percentage of SITSC fault and the other for binary output to detect the presence of USV.

The activation functions used are “tangent-sigmoid” for the input and hidden layer and “purelin” for the output layer. The Levenberg-Marquardt algorithm is selected as the training algorithm, with mean square error and regression curves serving as the performance criterion."

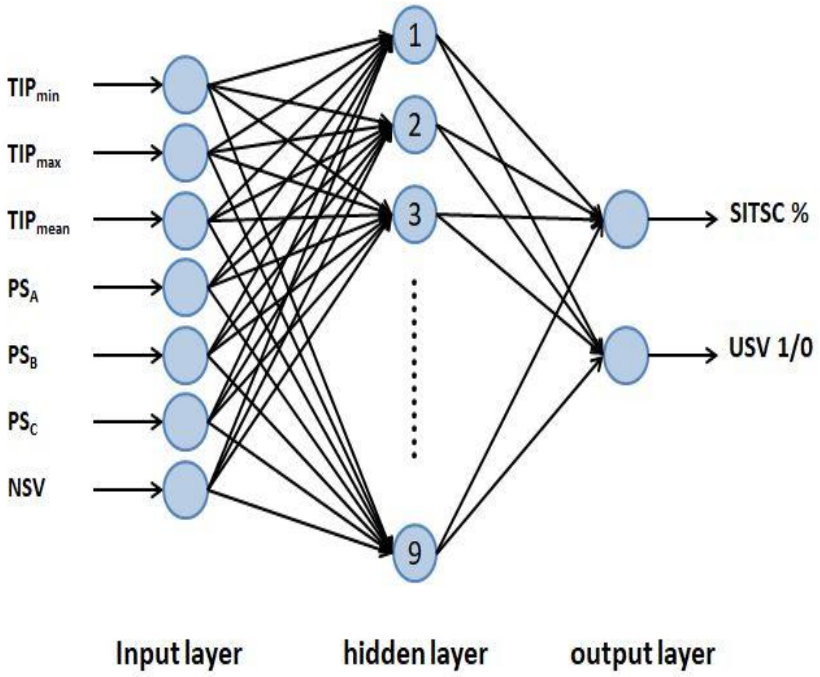

Figure 3.44: MLP-NN architecture for the proposed diagnosis system.

3.3.3.2. Training and testing dataset

The training and testing process of the MLP-NN is conducted offline. To ensure an MLP-NN effective in estimating the percentage of SITSC fault and detecting USV occurrence, the designed NN should demonstrate generalization across a comprehensive range of operating conditions, including various fault occurrences and load torques. To achieve this, an input dataset is prepared with different operating cases, covering a range of SITSC percentages from 0% to 10% (with a step of 1% for each phase).

Additionally, three unbalanced supply voltage cases (7%, 10%, and 15% of the power supply) and balanced supply voltage cases (0%, 2%, 3%, and 5% of the power supply) are included. Load torque varies from 0% to 100% of the full load torque, with a step of 10%. Consequently, the input dataset consists of 203 cases, with 120 cases allocated for training and 83 cases for testing the trained ANN.

For the output dataset, it is a matrix of size (2×203), where 183 cases are designated for SITSC percentage, and 20 cases are reserved for indicating USV occurrence.

3.3.4. Results and discussion

3.3.4.1. Simulation results

The proposed MLP-NN is assessed by three criteria, Mean Squared Error (MSE), regression analysis. As depicted in Figures from 3.45 to 3.47; the performances of the MLP-NN are shown.

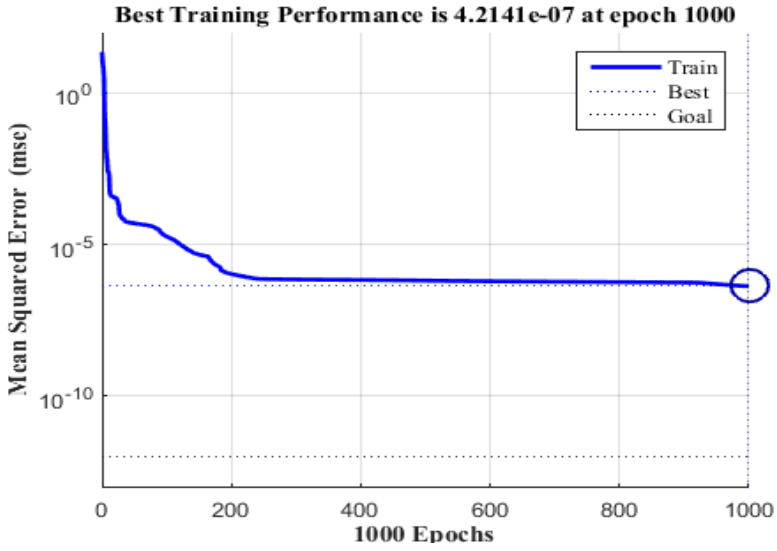

Figure 3.45: MSE training performance.

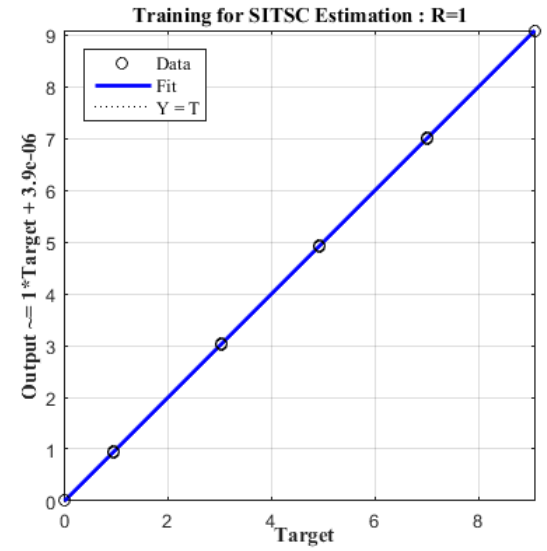

(a)

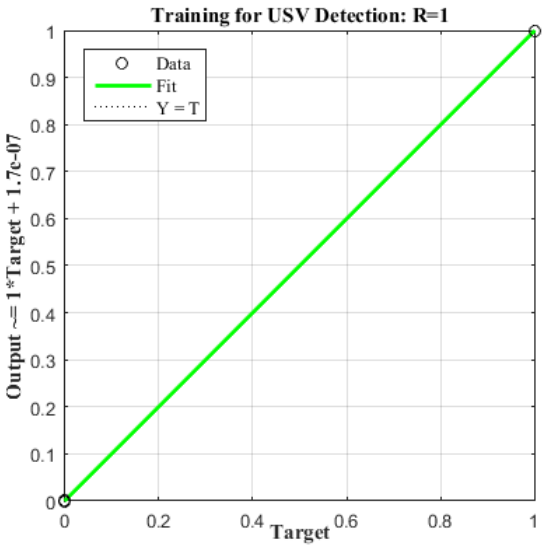

(b)

Figure 3.46: Regression analysis for training (a) SITSC estimation, (b) USV detection

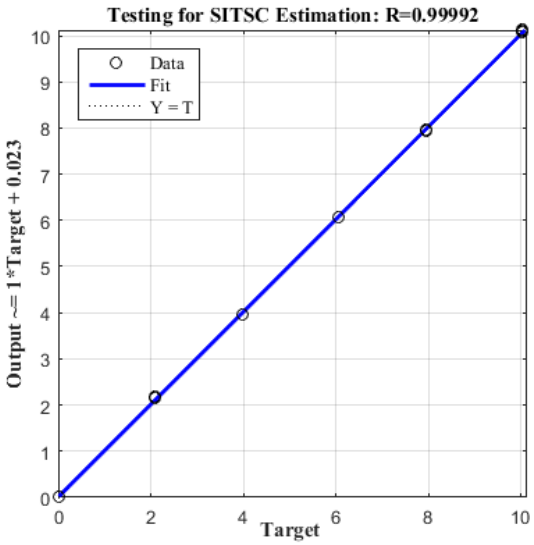

(c)

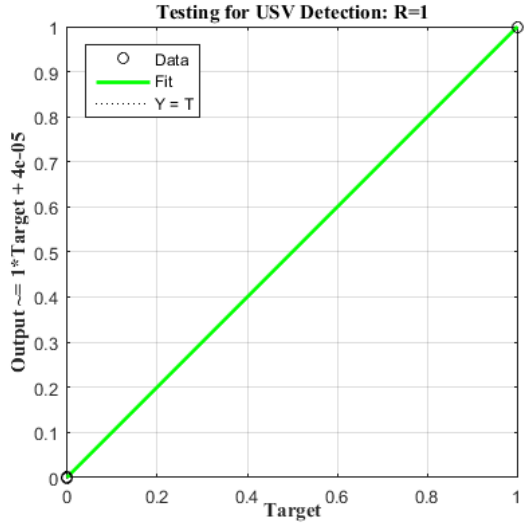

(d)

Figure 3.47: Regression analysis for testing (c) SITSC estimation, (d) USV detection.

The performance of the MLP-NN has reached a significant level, as demonstrated by Figures from 3.45 to 3.47. Specifically, after 1000 epochs of training, the MSE has achieved a value of (4.2141×10^{-7}) (Figure 3.45), within only t=5 seconds.

Figures 3.46 and 3.47 illustrate the results of the regression analysis. Linear regression establishes a model that relates prediction data and responded data in a linear relationship [51], represented the fit function knows as the following equation:

$$y = \alpha x + \beta \tag{3.13}$$

A good fit function is expected to closely align with the identity function ($y = x$), indicating $\alpha \cong 1$ and $\beta \cong 0$. Analysis of the regression study conducted previously reveals

a favorable fit function, where β is varies between 2.3×10^{-2} and 1.7×10^{-7} which can be negligible and α equals 1 for both the training and testing datasets.

3.3.4.2. Experimental results

To validate the proposed Fault identification process, experimental tests were conducted for diagnosing SITSC in the Induction Motor (IM). The three-phase squirrel cage induction motor utilized in the laboratory was simulated under different cases of SITSC, USV and load torque variation. SITSC faults were induced in all three phases of the stator. USV was generated using high power rheostats, by inserting them between the voltage source and the motor terminal board. The validation dataset comprised thirty-four samples, including seven healthy cases, twenty cases with USV occurrence and twenty-seven SITSC fault occurrences [51]. The shorted turns varied as (6, 24, 30, 54, 60 turns). The variations in load torque are (0%, 50% and 100% of the full load). The results of the validation are illustrated in Figures 3.48 and 3.49 [51].

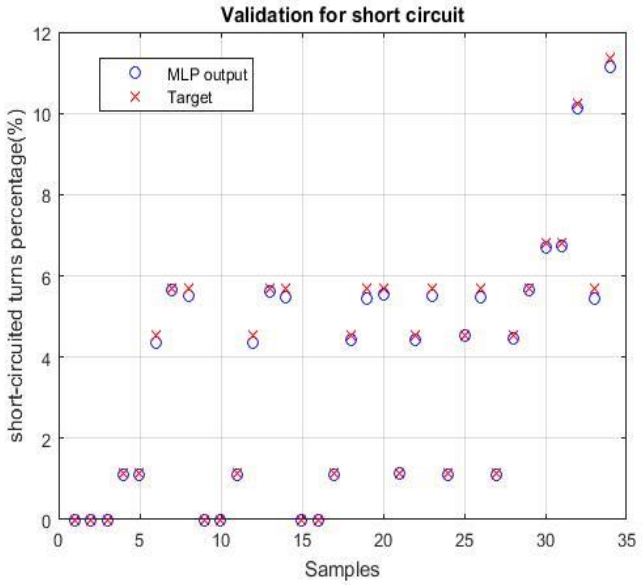

Figure 3.48: Validation of MLP-NN for SITSC fault estimation.

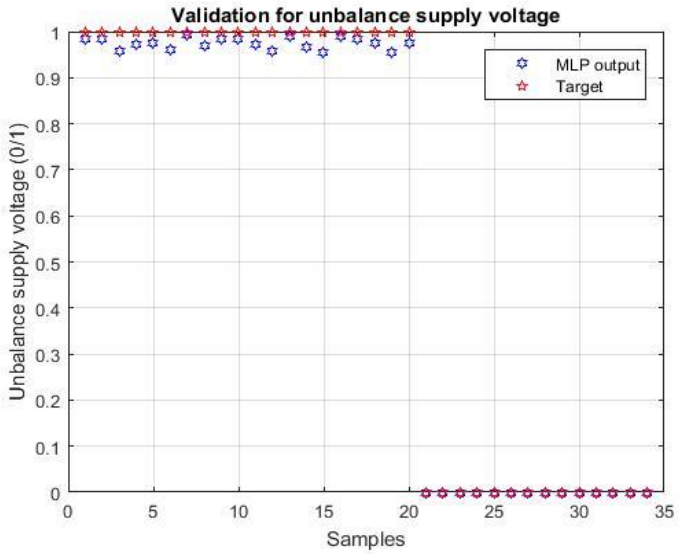

Figure 3.49: Validation of MLP-NN for USV occurrence.

Figure 3.48 demonstrates the commendable performance of the MLP-NN using the dataset provided by the test-bed. These results align closely with the targeted outcomes, indicating high concordance. However, if SITSC fault occur in two or three phases, the MLP-NN performance may diminish due to the data resembling that of a weakly faulted IM.

Additionally, Figure 3.49 showcases the effective detection of USV occurrences. When there is no USV, the indicator remains close to zero, while the indicator ranges between 0.95 and 1 in the presence of USV. Notably the appearance of USV results in an indicator value close to one.

Following a thorough investigation of the proposed diagnostic system, the MLP-NN yields commendable results while maintaining the simplicity of its architecture and calculations. As depicted in the last figures, the accuracy of the proposed method exceeds 95%.

3.4. Conclusion

In this chapter, two distinct approaches for diagnosing Induction Motor (IM) issues were explored. The first method focuses on SITSC-FDC. It employs a FF-NN to classify the SITSC fault source whether it's from phase a_s, b_s or c_s. The FDC process depends on the three- phase *IP* delivered by the three phase stator currents and voltages. The FF-NN-based approach has an accuracy of 90%.

The second diagnosis method introduces an efficient technique for estimating SITSC percentage and detecting occurrences of USV. A fault classifier for SITSC and USV is implemented using MLP-NN. This approach consist of monitoring the statistical characteristic of the total instantaneous power, the average value of shift between line current and phase voltage, and negative sequence voltage. According to the previous results, the proposed process gives good results despite the simplicity of its architecture and calculations.

Chapter (4)
Cascaded approach for SITSC and USV faults identification using multi ANNs

4.1. Introduction

In this chapter, four types of Induction Motor (IM) diagnosis were established. Those are Fault Detection and Classification (FDC) of SITSC, Fault Severity Estimation (FSE) of SITSC, Fault Detection and Classification (FDC) of USV, and finally Fault Severity Estimation (FSE) of USV.

The proposed Fault Identification (FI) process is done in cascaded manner. In the first cascade, the FI permits to detect the category of the fault whether it is a SITSC or USV. Once the FI process recognizes the type of fault, the second cascade is activated automatically. This last allows the estimation of fault severity by the approximate percentage of SITSC or USV.

Four types of Artificial neural networks (ANNs) were investigated to pursue the proposed FI including Feed Forward Neural Network (FFNN), Radial Basis Network (RBN), Radial Basis Extended Network (RBEN), and Generalized Regression Neural Network (GRNN).

The IM-mathematical model (already developed in chapter 2) was used to analyze the current and voltage sequence components in order to extract the best features. The ratios between positive and negative sequence voltage and current were selected as the appropriate features of the cascaded approach.

The four cascaded ANNs where trained and tested under experimented dataset, and they demonstrate good performance in the diagnostic field.

4.2. Fault indicators choice

The symmetrical components are significant tool for analyzing and solving the problems of any unbalanced three-phase system. The symmetrical components are found reliable indicators of SITSC and USV faults. In fact, symmetrical IM supplied with symmetrical three-phase voltage sources will not produce negative and zero sequences of current or voltage. But when a SITSC fault occurs, symmetry will disturb and generate

negative and zero sequences current. Same for USV fault, symmetry will breakdown and generates negative and zero sequences voltage.

Using Fortescue's transformation given by equation (4.1), symmetrical components (I_p, I_n) are calculated from unbalanced phase currents (i_{as}, i_{bs}, i_{cs}) and symmetrical components (V_p, V_n) are calculated from unbalanced phase voltages (v_{as}, v_{bs}, v_{cs}).

$$\begin{cases} I_p = \frac{1}{3}(i_{as} + e^{j4\pi/3} i_{bs} + e^{j2\pi/3} i_{cs}) \\ I_n = \frac{1}{3}(i_{as} + e^{j2\pi/3} i_{bs} + e^{j4\pi/3} i_{cs}) \\ V_p = \frac{1}{3}(v_{as} + e^{j4\pi/3} v_{bs} + e^{j2\pi/3} v_{cs}) \\ V_n = \frac{1}{3}(v_{as} + e^{j2\pi/3} v_{bs} + e^{j4\pi/3} v_{cs}) \end{cases} \quad (4.1)$$

Fundamentally, the three-phase IM is a symmetrical system in healthy conditions and produces only positive sequence currents. It generates positive, negative, and zero sequence when symmetry is disturbed during a SITSC fault situation, not like in voltage source. In reality voltage source is an asymmetrical system. In this work, voltage source is considered symmetrical if the percentage of asymmetry is less than 5%; if it is more than 5% the voltage source is considered as asymmetrical. Due to the difficulty in creating the SITSC and USV and measuring the currents and voltages experimentally for high values of percentage of SITSC and USV, we required to create the Simulink model using MATLAB software. The IM model with SITSC and USV is constructed based on the fundamental equations mentioned in the chapter 2. The model of the IM with SITSC and USV is shown in Appendix C. The unbalance of voltage source is created by changing the amplitude of voltage for one phase.

The model is simulated for different levels of SITSC in the phases of the IM and different levels of USV in only one phase. The values of current and voltage are recorded. From these values, negative and positive sequence currents are calculated; same for negative and positive sequence voltages. These last are tabulated in Tables from 4.1 to 4.5.

Table. 4.1 Symmetrical components in case of Stator Inter turn short-circuit

SITSC %	V_p(V)	V_n(V)	I_p (A)	I_n (A)
0	311.1	3.4e-4	1.5	2.99e-4
2	311.1	3.5e-4	1.5	0.03
4	311.1	3.4e-4	1.5	0.09
6	311.1	3.4e-4	1.5	0.17
8	311.1	3.4e-4	1.6	0.26
10	311.1	3.5e-4	1.7	0.37

Table. 4.2 Symmetrical components in case of unbalance voltage source.

USV %	V_p(V)	V_n(V)	I_p (A)	I_n (A)
0	311.1	3.37e-4	1.5	2.86e-4
3	308	3.1	1.4	0.1
5	305.9	5.2	1.4	0.17
7	303.9	7.3	1.4	0.24
10	300.8	10.4	1.4	0.34

Table. 4.3 Symmetrical components in case of load torque variation

LT (%)	V_p(V)	V_n(V)	I_p (A)	I_n (A)
0	311.1	3.4e-4	1.5	2.99e-4
50	311.1	3.5e-4	1.6	1.9e-4
100	311.1	3.5e-4	2.1	9e-4

The variation of the IM's positive and negative currents and voltages are presented as function of SITSC, USV and load torque (LT) percentages variations successively in tables 4.1, 4.2 and 4.3. In order to analyze the impact of combination of LT with SITSC and LT with USV on V_p, V_n, I_p and I_n, the tables 4.4 and 4.5 resume the obtained results. The analysis shows that in case of a SITSC prevalence; the positive current stills constant for almost all SITSC percentages; but the negative current increases as the SITSC severity rises. Meanwhile the positive and negative voltages have no deviations. An USV occurrence has a different influence; the negative current and voltage amplitudes found to be increasing gradually with the USV level rising. Alike the positive voltage which

decreases as the USV severity rises. However the positive current keeps constant. The LT variation has an expected effect, where the positive and negative voltages save their values, same for the negative current which is approximately zero. The positive current automatically rises up as the LT level grows up.

Table. 4.4 Symmetrical components for a SITSC as function of LT variation

SITSC (%)	LT %	V_p(V)	V_n(V)	I_p (A)	I_n (A)
2	0	311.1	3.5e-4	1.5	0.03
	50	311.1	3.4e-4	1.6	0.03
	100	311.1	3.5e-4	2.1	0.03
4	0	311.1	3.4e-4	1.5	0.09
	50	311.1	3.4e-4	1.7	0.09
	100	311.1	3.6e-4	2.1	0.09
6	0	311.1	3.4e-4	1.5	0.17
	50	311.1	3.4e-4	1.7	0.18
	100	311.1	3.5e-4	2.2	0.18
8	0	311.1	3.4e-4	1.6	0.26
	50	311.1	3.5e-4	1.8	0.27
	100	311.1	3.5e-4	2.2	0.27
1	0	311.1	3.5e-4	1.7	0.37
0	50	311.1	3.5e-4	1.9	0.38
	100	311.1	3.5e-4	2.2	0.39

Table. 4.5 Symmetrical components for a USV as function of LT variation

		LT %	V_p(V)	V_n(V)	I_p (A)	I_n (A)
USV (%)	3	0	308	3.1	1.4	0.1
		50	308	3.1	1.6	0.1
		100	308	3.1	2	0.1
	5	0	305.9	5.2	1.4	0.17
		50	305.9	5.2	1.6	0.17
		100	305.9	5.2	2.1	0.17
	7	0	303.9	7.3	1.4	0.24
		50	303.9	7.3	1.6	0.24
		100	303.9	7.3	2.1	0.24
	10	0	300.8	10.4	1.4	0.34
		50	300.8	10.4	1.6	0.34
		100	300.8	10.4	2.1	0.34

The combination of the LT with SITSC variation furnishes familiar results. The positive current increases slowly when varying SITSC and LT percentages, while the negative current amplitude stabilizes when varying LT and rise up when changing SITSC percentages. Instead the positive and negative voltages, they do not change whenever LT or SITSC varies. The combination of the LT with USV variation gave significant results; the positive and negative voltage amplitudes stabilize when rising LT severity, likewise the negative current; while they rise up when enhancing USV percentage. The positive current increases when LT severity rises and stabilizes when USV severity graduates.

The variation of positive and negative components as function of LT variations demonstrates that LT have no influence on negative voltage, negative current and positive voltage. It has an impact only on positive current.

4.3. Features selection

Feature extraction techniques are widespread in ML. it has different range such as statistical and model based techniques. In ML; it is required to reduce the large amount of information contained in a signal to a small number of features, those last reflects the overall characteristics of a signal. This procedure is known as signal feature extraction

[63]. In this work, the features are extracted from positive and negative current and voltage signals. The two signals should be preprocessed to fit the ML-based FI system. The large information in the two signals must be converted to a few features, so that the proposed system learn how to distinguish between features representing healthy operating condition and faulty one. In this section; the per-unit change in a negative sequence with positive sequence is proposed as an effective fault feature factor for both SITSC and USV. The following equations express the key factors of the proposed FI process:

$$\delta = \frac{positive\ sequence - negative\ sequence}{positive\ sequence} \quad (4.2)$$

In case of a current factor, equation (4.2) becomes:

$$\delta_i = \frac{I_P - I_n}{I_p} \quad (4.3)$$

In case of a voltage factor, equation (4.2) becomes:

$$\delta_v = \frac{V_P - V_n}{V_p} \quad (4.4)$$

δ_i is considered as the main parameter for FDC of SITSC . Also δ_v is considered as the main input parameter for FDC of USV. And both δ_i and δ_v with V_n and I_n are adopted for FSE of SITSC and USV.

The values of δ_i and δ_v are tabulated in table 4.6 and 4.7 respectively for various levels of SITSC and USV.

Table. 4.6 The variation of δ_i and $\delta_v$as function of SITSC variation

LT (%) / SITSC (%)	0		50		100	
	δ_i	δ_v	δ_i	δ_v	δ_i	δ_v
0	0.99	1	0.99	1	1	1
2	0.98	1	0.98	1	0.98	1
4	0.94	1	0.95	1	0.95	1
6	0.89	1	0.9	1	0.9	1
8	0.84	1	0.84	1	0.84	1
10	0.78	1	0.78	1	0.78	1

Table. 4.7 The variation of δ_i and $\delta_v$as function of USV variation

LT (%) / USV (%)	0		50		100	
	δ_i	δ_v	δ_i	δ_v	δ_i	δ_v
0	0.99	1	0.99	1	1	1
3	0.93	0.99	0.94	0.99	0.94	0.99
5	0.89	0.98	0.89	0.98	0.9	0.98
7	0.83	0.97	0.85	0.97	0.85	0.97
10	0.76	0.96	0.79	0.96	0.79	0.96

Observing tables 4.6 and 4.7, it can be noticed that δ_i and δ_v gradually decreases with the increase in SITSC and USV. Furthermore, the LT rise seems to have a slight effect on δ_i and δ_v values, for example for a SITSC of 2% and a USV of 0% , δ_i is 0.98 for all LT levels. Although δ_v remains equal to 1. For a SITSC of 0% and a USV of 7% the δ_i values are between 0.83 and 0.85, therefore a variation of 0.02 for all LT levels. δ_v remains constant for all LT levels and equals to 0.97. From these tables; it can be perceived that δ_i and δ_v are mostly insensitive to the LT variations. This analysis impulses δ_i and δ_v to be the ultimate selected features.

4.4. Description of the fault identification process

The proposed diagnosis procedure begins with the systematic collection of data pertaining to the three-phase stator currents and voltages from an experimental Induction Motor (IM). This IM stator has different number of SITSC: (6, 24, 30, 36, 54, 60) which correspond to (1.13%, 4.54%, 5.68%, 6.82%, 10.23%, 11.36%); at different LT conditions: 10%, 20%, 30, 40, 50, 60, 70, 80, 90 and 100% of the full LT and different levels of voltage shutdown (6V, 7.6V, 8V, 8.3V, 8.8V, 10.9V, 11.2V, 11.8V, 12.4V, 14.4V, 15.6V, 18V, 22V, 22.5V, 23.5V, 30V) which correspond to (1.93%, 2.44%, 2.57%, 2.67%, 2.83%, 3.5%, 3.6%, 3.8%, 3.99%, 4.63%, 5.01%, 5.79%, 7.07%, 7.23%, 7.55%, 9.64%) of voltage source. These currents and voltages are converted to symmetrical components using Fortescue transform. The symmetrical current and voltage signals are recollected in feature extraction. These extracted features are provided for SITSC and USV faults classification and severity estimation using MANNs system, figure 4.2 shows the proposed system. The MANNs system uses ANNs in cascade manner. Three ANNs are clustering to succeed the

proposed FI process. ANN_1 uses δ_i and δ_v to classify the occurred fault. Afterward, ANN_2 and ANN_3 employ the ANN_1 results with negative sequence voltage and current to estimate the fault severity. ANN_2 estimates the percentage of SITSC and the ANN_3 estimates the USV percentage. The performance of each ANN is evaluated taking into account MSE and Regression analysis metrics in order to select the optimal classifier with the highest accuracy. The overall schematic representation of the proposed process is presented in Figure 4.1.

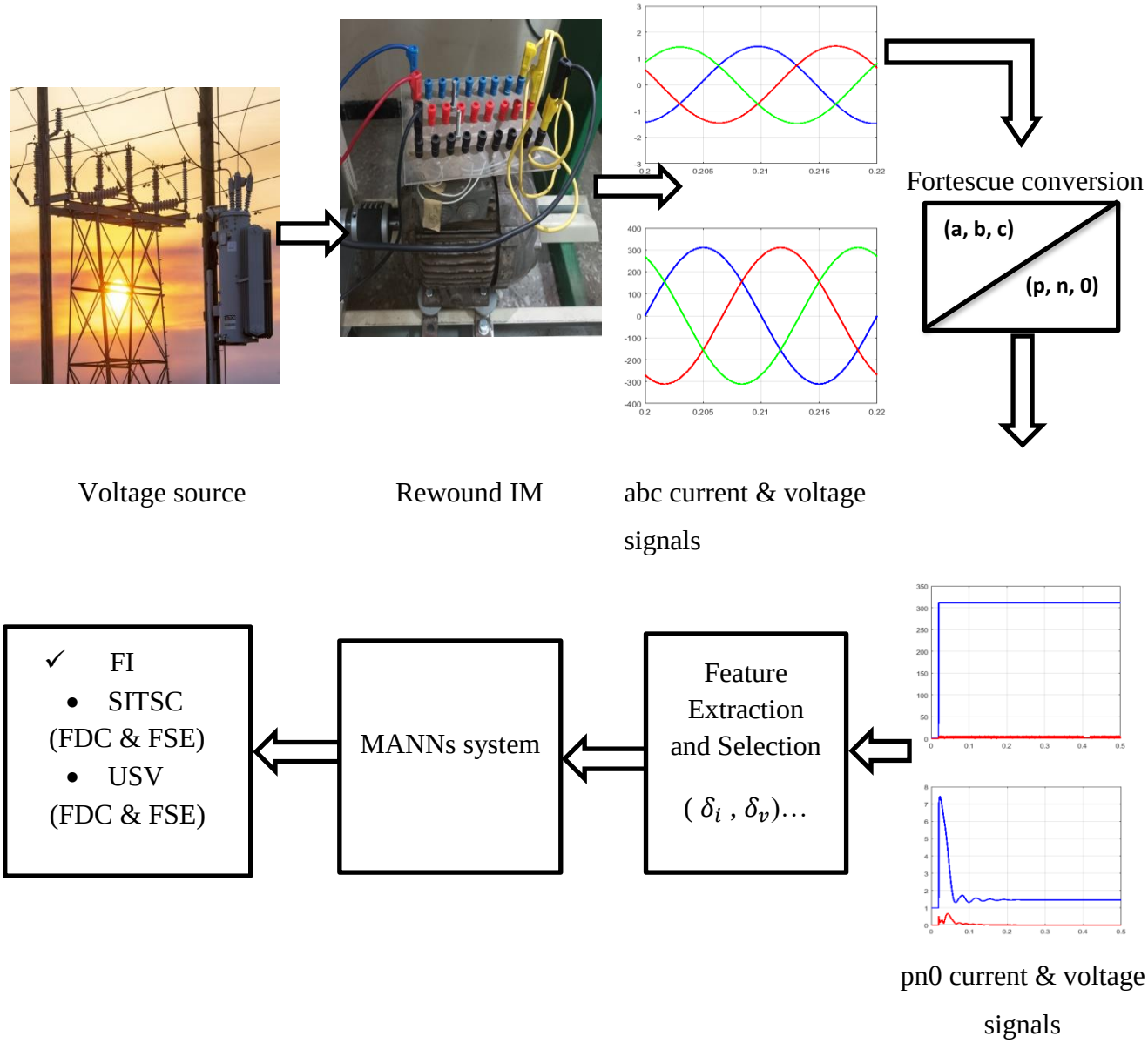

Figure 4.1 : Schematic diagram of the proposed FI process

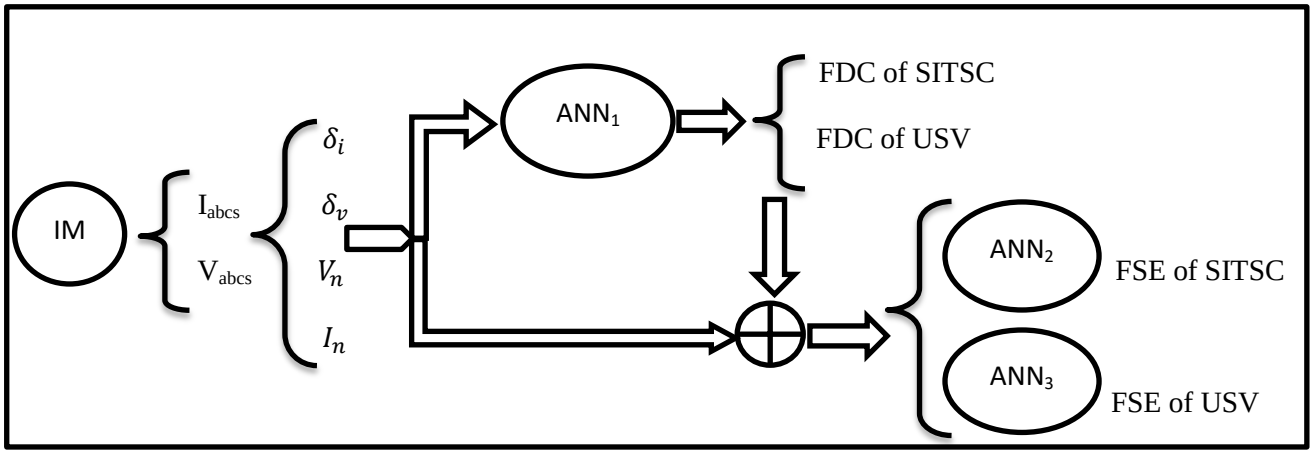

Figure 4.2: MANNs system.

4.5. Results and discussion

4.5.1. Artificial neural networks configuration

Table 4.8 resumes the configuration of each used ANN. Prediction of the used ANNs depends on training and testing dataset, this last is created using experimental set up measures. The main work of NN algorithm is to brand feature extraction. The feature extraction is the important part of the study; δ_i and δ_v selected as the main features of the proposed FI. It helps to split the dataset for analysis. The dataset then is split into training data set and testing data set. 80% of the data set was used to train the ANNs and 20% was used to evaluate the performance of the classifiers for finding out the accuracy of each ANN.

Table. 4.8 ANNs configuration

	ANN_1				ANN_2				ANN_3			
	IL	OL	HL	Transfer Function	IL	OL	HL	Transfer function	IL	OL	HL	Transfer function
FFNN	4	2	7	Sig– Lgsig	6	1	11	Sig- Prln	6	1	11	Sig- Prln
RBNN	4	2	96	Rbf –Prln	6	1	96	Rbf –Prln	6	1	96	Rbf –Prln
RBENN	4	2	96	Rbf –Prln	6	1	96	Rbf–Prln	6	1	96	Rbf –Prln
GRNN	4	2	96	Rbf –Prln	6	1	96	Rbf –Prln	6	1	96	Rbf –Prln

IL: input layer; OL: output layer; HL: hidden layer.
Sig: tangent sigmoid function. Prln: pure line function.
Lgsig: Logarithmic sigmoid function. Rbf: Radial basis function

4.5.2. Training, testing and validating dataset

The training, testing and validating process is conducted using experimental data obtained from laboratory test bed. To ensure effectiveness in estimating the percentage of

SITSC fault and detecting USV occurrence, the designed ANNs should demonstrate generalization across a comprehensive range of operating conditions, including various fault occurrences and load torques. To achieve this, an input dataset is prepared with different operating cases.

- Therefore, the IM stator has different number of SITSC, 6, 24, 30, 36, 54, 60 shorted-turns) which correspond to (1.13%, 4.54%, 5.68%, 6.82%, 10.23%, 11.36% of SITSC), covering a range of SITSC percentages approximately from 1% to 12% .
- Additionally, different levels of voltage shutdown (6V, 7.6V, 8V, 8.3V, 8.8V, 10.9V, 11.2V, 11.8V, 12.4V, 14.4V, 15.6V, 18V, 22V, 22.5V, 23.5V, 30V) which correspond to (1.93%, 2.44%, 2.57%, 2.67%, 2.83%, 3.5%, 3.6%, 3.8%, 3.99%, 4.63%, 5.01%, 5.79%, 7.07%, 7.23%, 7.55%, 9.64%) of voltage source covering a range of USV percentages approximately from 1% to 10% .
- Load torque varies from 0% to 100% of the full load torque, which correspond to 10%, 20%, 30, 40, 50, 60, 70, 80, 90 and 100% of the full load.

Consequently, the input dataset consists of 112 cases, with 80% of cases allocated for training, 10% of cases for testing and 10% for validating the ANNs.

4.5.3. Results and discussion

The mean square errors (MSE_s) were calculated in each iteration to find the ultimate accuracy rate. Table 4.9 resumes the final MSE of every algorithm. The regression is also used to evaluate the performance of the classifiers; Figures 4.3 and 4.5 illustrates the regression plots between ANN outputs and predictive values. To observe the deference between target and output values; the error between those lasts was calculated and illustrated for each ANN. Moreover, the plotting of the outputs and the targets is also illustrated in figures 4.6 and 4.8.

Table 4.9 MSE_s final values

	ANN_1	ANN_2	ANN_3
FFNN	5.21e-4	8.53e-4	1.96e-6
RBN	1.96e-6	1.76e-16	2.28e-28
RBEN	5.06e-6	2.13e-16	2.70e-28
GRNN	8.06e-2	8.95e-2	4.87e-2

The table of MSE values shows a good performance rate for all algorithms used. For the first cascaded ANN_1 which is dedicated to the FDC, GRNN gave a higher MSE

value than the other algorithms, which makes it classified as the lowest in performance. In fact, the RBN and the RBEN showed a very low MSE rate, which explains the robustness of these latters. FFNN has reached an adequate value. The second and third cascade ANN_2 and ANN_3 are assigned for the SITSC and USV FSE; the training and testing results furnish an extremely high performance rate of RBN and RBEN with the rate of 10^{-16} and 10^{-28}, that why they are categorized as the most efficient for the FI purpose. The FFNN presents a low value of MSE which reduces the performance of this last. GRNN has given a higher value of MSE which is considered as the weakest in FDC and FSE.

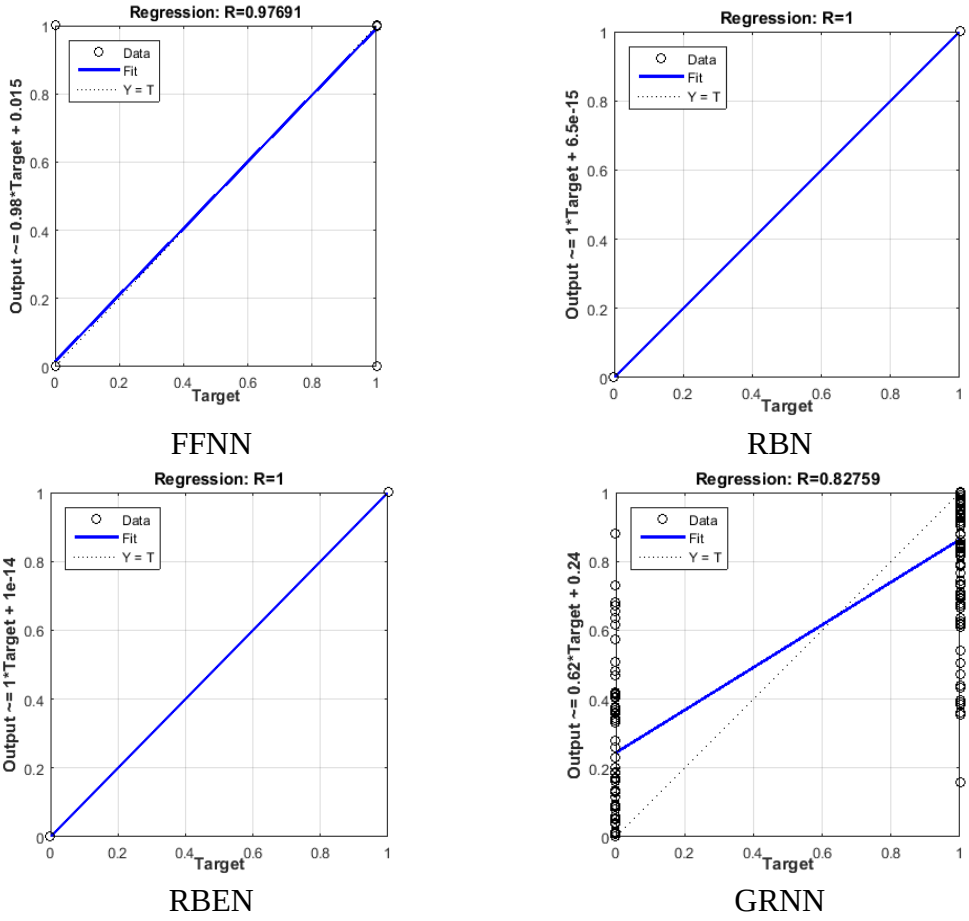

Figure 4.3 ANN_1 regression analysis

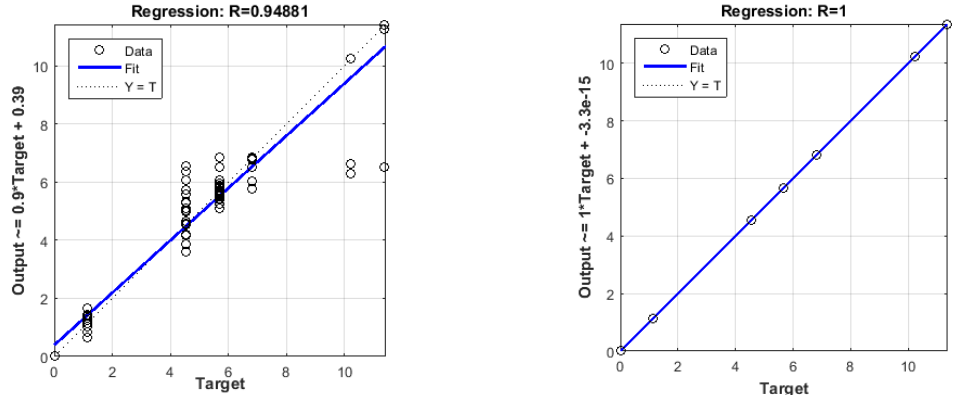

FFNN RBN

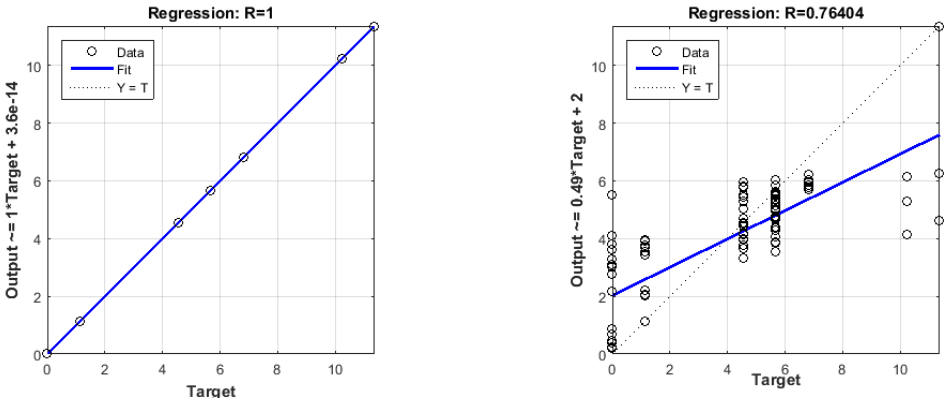

RBEN GRNN

Fig.4.4: ANN_2 regression analysis

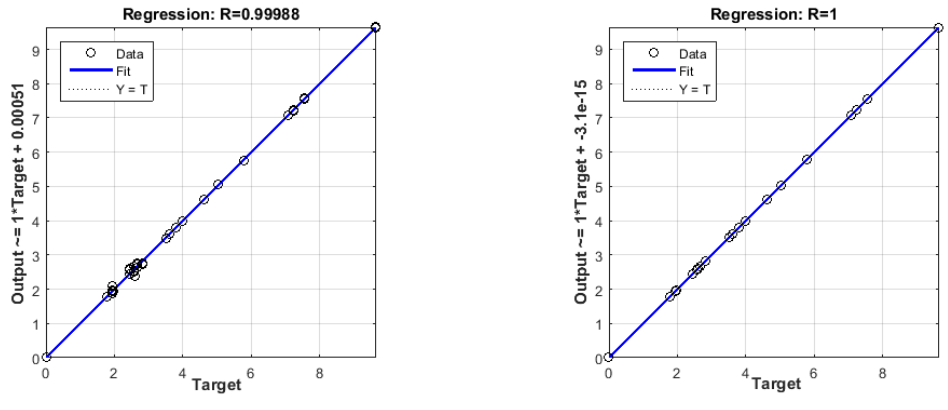

FFNN RBN

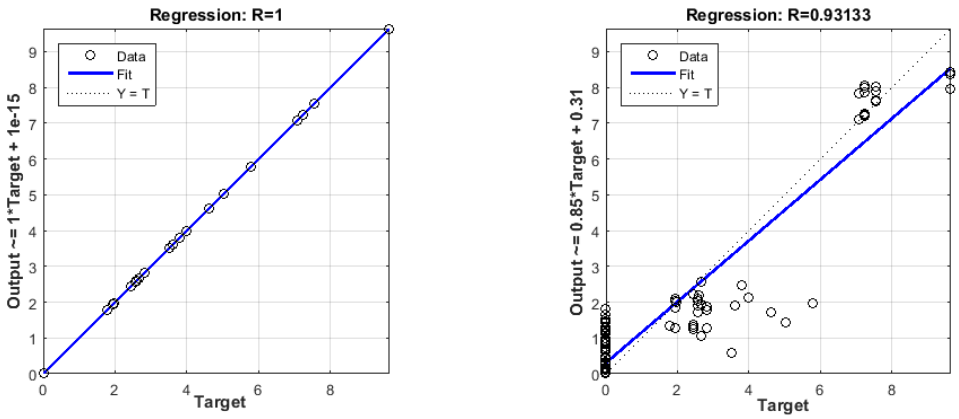

RBEN GRNN

Figure 4.5 : ANN_3 regression analysis

Linear regression forms a model that relates the target (the prediction data) and the ANN output (the response data) in a linear relationship called fit function like shown in equation (4.5) thereafter:

$$y = ax + b \tag{4.5}$$

Where the model is expected to show a good fit ($y = x$) when $a \simeq 1$ and $b \simeq 0$.

Figures from 4.3 to 4.5 shows the regression analysis of all used ANNs; the RBN and RBEN provide a suitable fit between there outputs and the targets; thus all the curves slopes are equal to 1, as well as the coefficient b is extremely small and is close of 10^{-15}; and that is for all ANNs. FFNN also showed a well regression, therefore the slopes of the curves are all greater than 0.9, moreover the coefficient b varies between 0.39 and $5.1 * 10^{-4}$ which makes it reliable. It is worth noting that FFNN regression gives a lower performance, when it is the case of FSE of SITSC. GRNN has not responded to regression analysis as well as other used ANN; in case of FDC and FSE of SITSC the curves slopes are of 0.85 and 0.49 and the coefficient b is of 2 and 10^{-15} successively. These results are less accurate than the first ones.

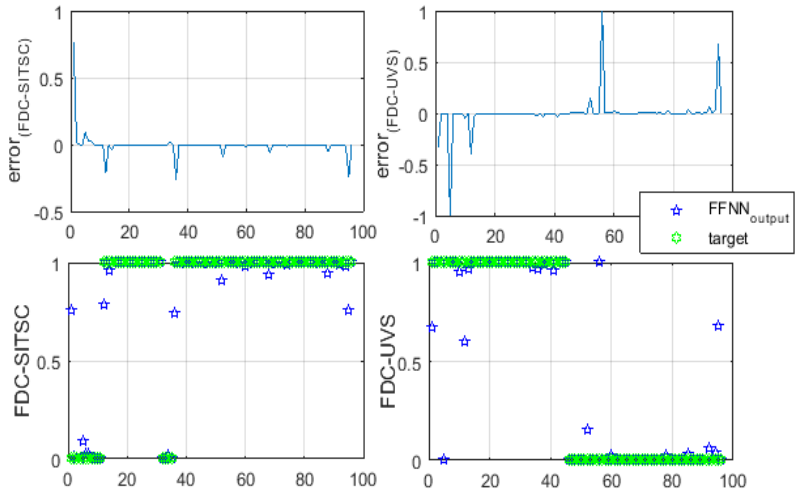

(a)

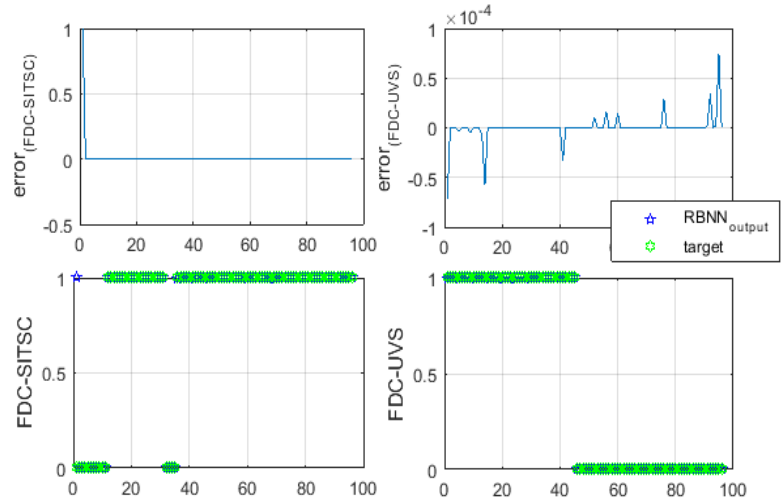

(b)

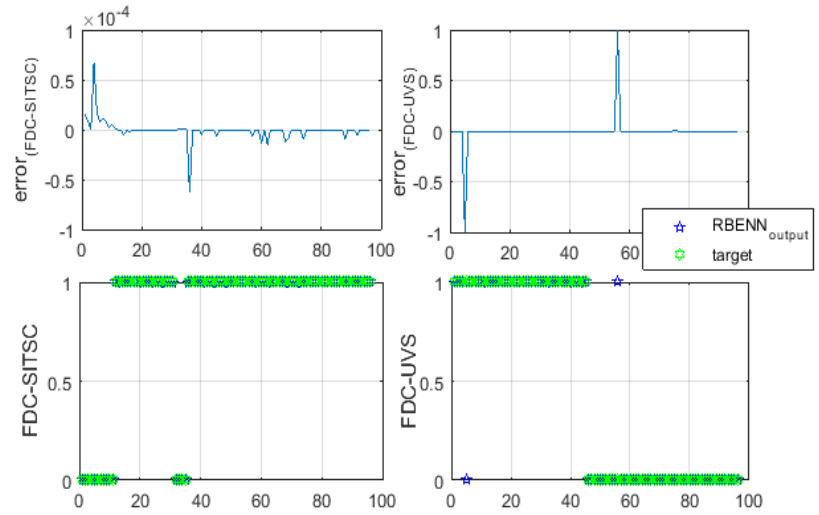

(c)

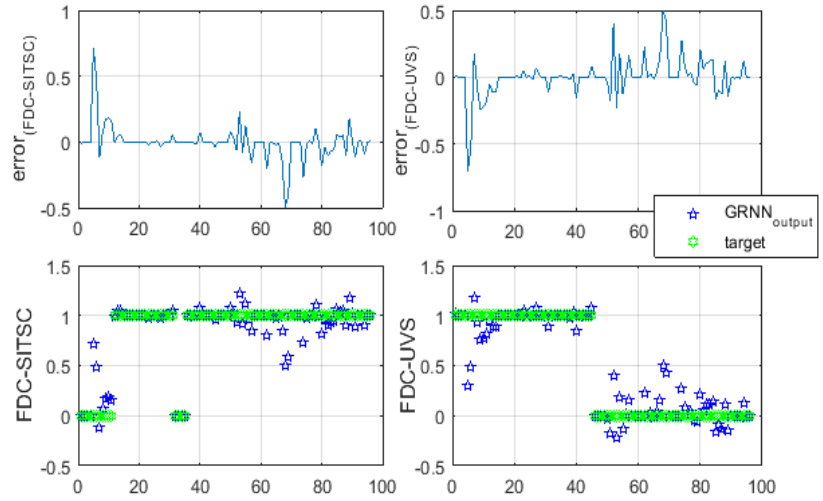

(d)

Figure 4.6 Outputs and targets; Error between outputs and targets for FDC-SITSC and FDC-USV, in case of ANN_1 type of: (a) FFNN, (b) RBNN, (c) RBENN, (d) GRNN.

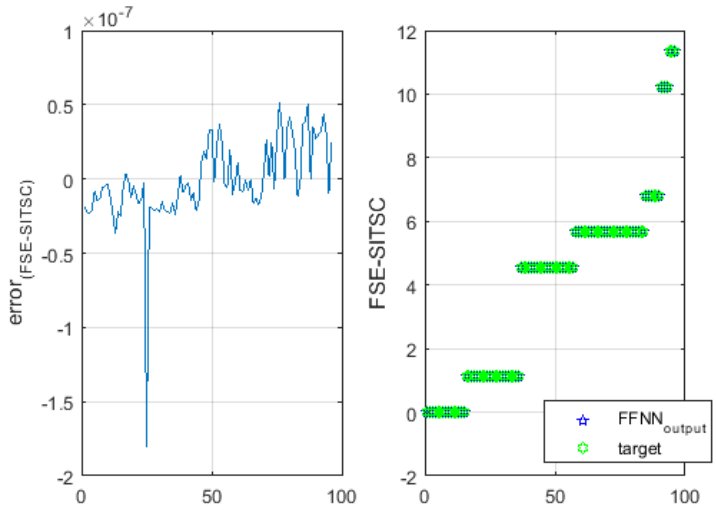

(a)

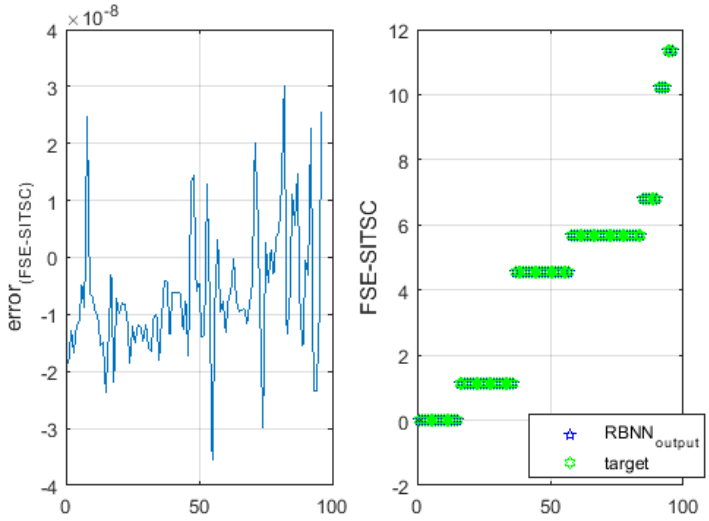
×10^-8
error(FSE-SITSC)
FSE-SITSC
RBNN output
target

(b)

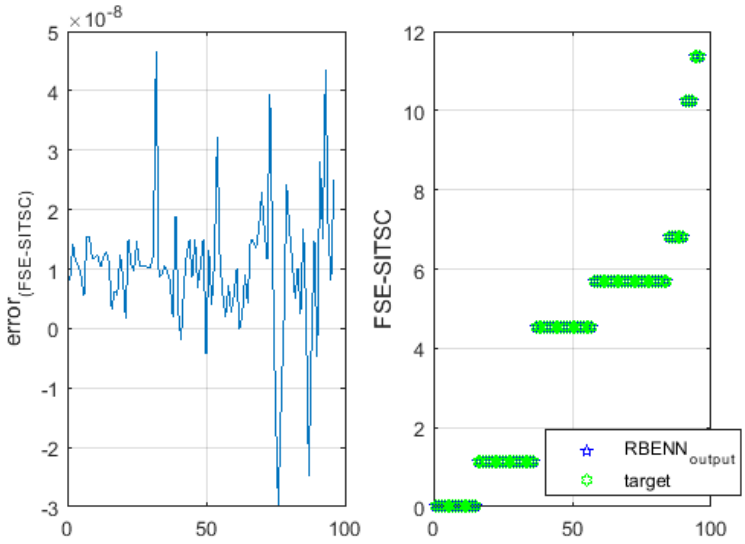
×10^-8
error(FSE-SITSC)
FSE-SITSC
RBENN output
target

(c)

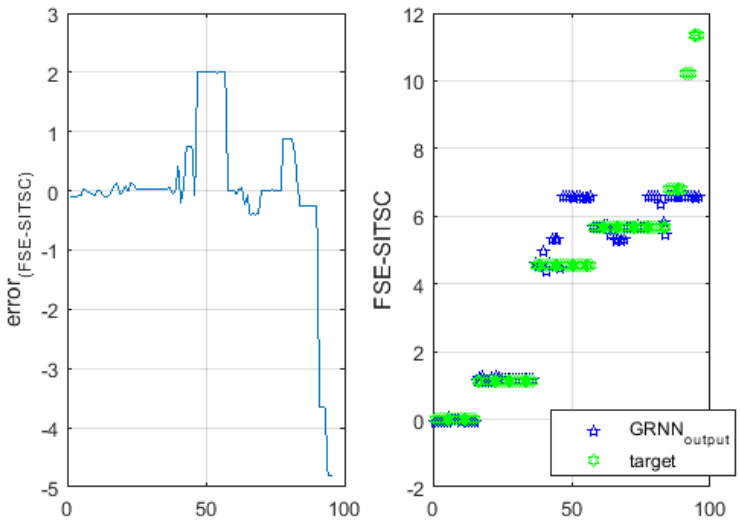
error(FSE-SITSC)
FSE-SITSC
GRNN output
target

(d)

Figure 4.7: Outputs and targets: Error between outputs and targets for FSC-SITSC in case of ANN_2 type of: (a) FFNN, (b) RBNN, (c) RBENN, (d) GRNN.

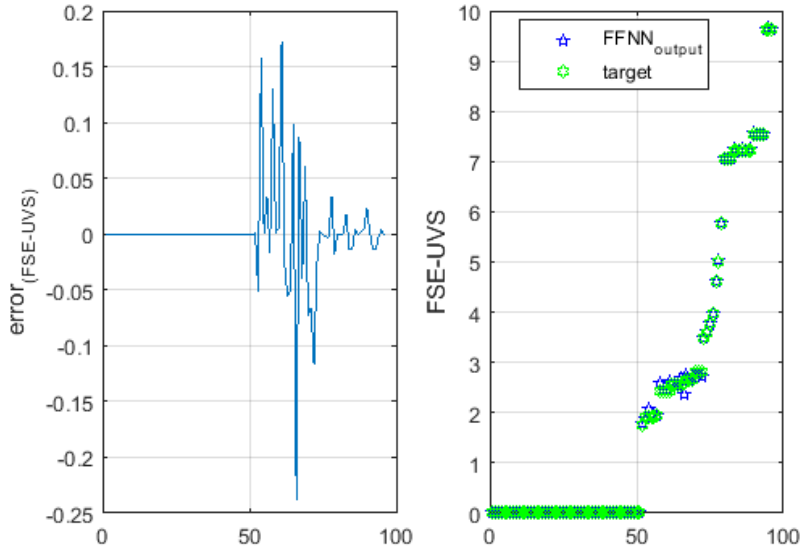

(a)

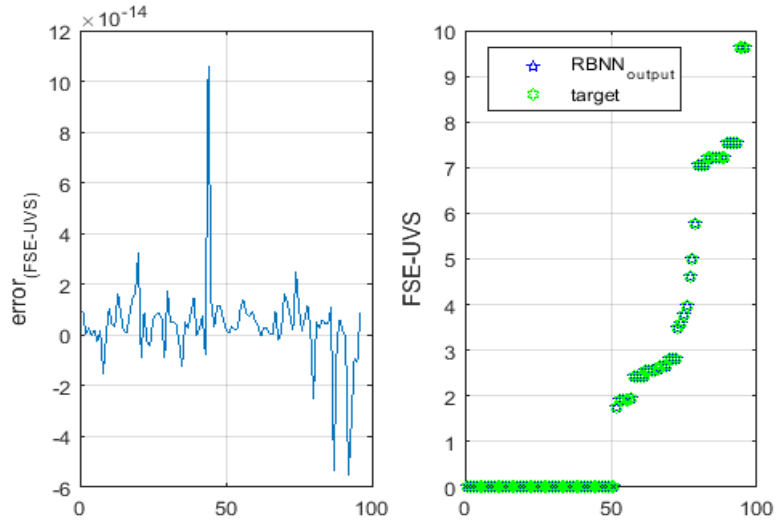

(b)

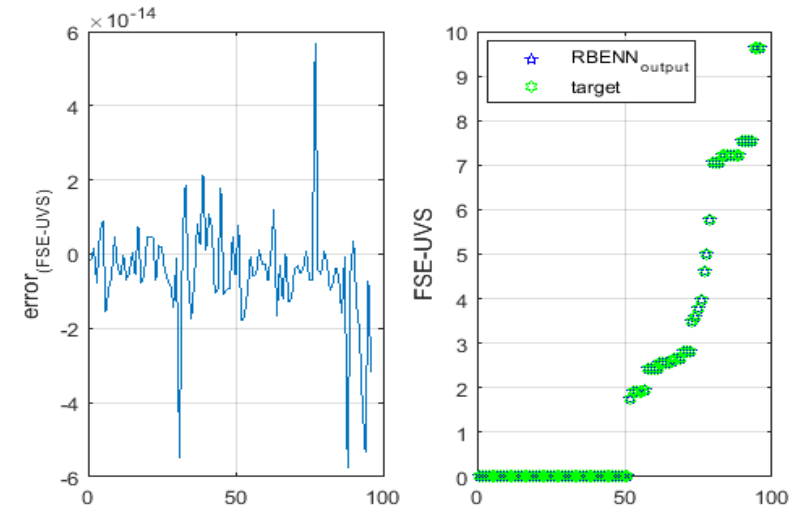

(c)

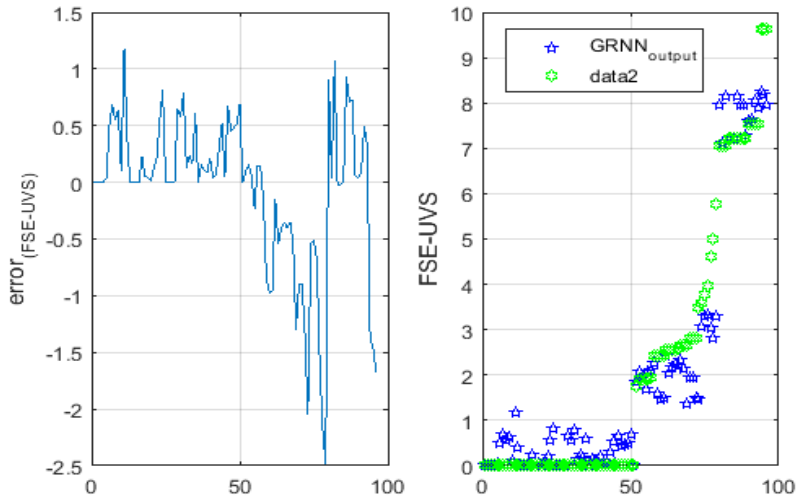

(d)

Figure 4.8 : Outputs and targets ; Error between outputs and targets for FSC-SITSC in case of ANN_3 type of: (a) FFNN, (b) RBNN, (c) RBENN, (d) GRNN.

The error is calculated as the difference between the target and ANN output, this one is presented as follows:

$$error = Target - MLA_{Output} \tag{4.6}$$

Figures from 4.6 to 4.8 illustrations the outputs and targets of all used ANNs, moreover the errors between those last is also presented.

In the case of SITSC-FDC and USV-FDC; the RBNN and RBEN provide a small error (10^{-4} for USV-FDC with RBNN and SITSC-FDC with RBENN) and a good correspondence between all the targets and the outputs. For the SITSC-FDC with RBNN and USV-FDC with RBENN, the errors are slight but show some peaks. The targets and

outputs are in correspondence only a few ones how are far from each other. The FFNN offers a small error of 10^{-1} with peaks about ±1; the correspondence between outputs and targets are appropriate, and a few ones who are distant from one another. Unlike FFNN, GRNN yields target and output values that are slightly separated and error values that vary about ±0.7.

In the case of SITSC-FSE and USV-FSE; the RBN and RBEN provide a very small error (10^{-8} and 10^{-14} for ANN_2 and ANN_3) and an extreme correspondence between there outputs and targets values. For the FFNN and GRNN; the error values are slightly lower (10^{-1} and 10^{0} for ANN_2 and ANN_3), the correspondence between the outputs and targets is highly favorable for FFNN algorithm. Unlike GRNN, the correspondence is acceptable for low percentage values of SITSC and USV. However, for higher percentages, GRNN produces output values far from the targets.

4.6. Conclusion

This chapter presents an FI approach employing ANNs to effectively detect, classify, and quantify both SITSCSC and USV faults. The proposed FI system utilizes four ANNs: FFNN, RBN, RBEN, and GRNN. These ANNs are employed to accurately detect and classify SITSC and USV faults, along with estimating the approximate percentage of each fault type.

The FI process commences with the extraction of significant indicators from the enhanced IM model (see chapter 2) that incorporates SITSC considerations in all three phases and USV in one phase. Moreover, the identification of the ratios between positive and negative sequences of current and voltage as the most critical features for both SITSC and USV faults.

Next, a cascade of ANNs is implemented as the core of the FI system; the MANNs process is responsible for both FDC and FSE of SITSC and USV. Following the training and testing phases for each ANN, the FI system converges to a stable state, achieving a MSE values ranging from 10^{-2} to 10^{-28}.

This work is successfully accomplished using an experimental test bed. Eliminating the need for additional sensors, the terminal voltage and current measurements alone suffice for diagnosis purpose.

Conclusion

The work conducted in this thesis focused on squirrel cage induction motor fault diagnosis. The analysis of statistics on electrical machines has demonstrated that stator faults and supply voltage unbalance are among the most common in induction machines. It has also been shown that the some techniques currently used in IM monitoring require accurate modeling with respect to faults. Therefore, modeling the machine for this purpose was the primary focus of this thesis. Two models were developed for the analysis an IM. Beside, monitoring IM with developed techniques like AI tools was the main objective of this purpose. Two advanced process were introduced for the diagnostic field.

The three-phase IM, due to its interesting characteristics: robustness, low cost, and ease of construction, offers an advantageous choice in many fields of application at fixed or variable speeds. However, in its classical modeling, SITSC faults are not fully taken into account (in the three phases) by researchers. Since the short circuit phenomena extensively occurs and may touch the whole phases; the classical models are no longer valid for describing its operation in fault mode. These various restrictions inherent in modeling have favored the development of mathematical model that could guarantee the simulation of the IM behavior under different classes of SITSC. The mathematical model has been used to promise a wide type of diagnosis process such as those based on AI methods. The use of AI-based methods has become a common tool in IM fault diagnosis, one of the most widespread methods is ANN.

The detection of IM-SITSC faults has been in interest for long years, because more than 36% of IM failures fall into SITSC [29]. Moreover; the presence of USV makes the fault detection system unable to know whether there is a SITSC fault or not, that is why identification of USV is also very important task. Besides; discriminate between SITSC fault and USV fault is too complicate; because the two phenomena give almost the same effects, only a few works arrived to differentiate between them. Additionally, detection is even more crucial when providing an estimate of the fault severity, as it allows time to implement solutions before the induction motor's operational area is compromised. These considerations have led us to focus our work on the development of:

- models dedicated to diagnosis
- AI-based method that:
    - ✓ Ensure the consideration of stator inter-turn short-circuit faults.
    - ✓ Ensure the consideration of unbalance supply voltage faults.

First, we focused on the analytical modeling of an asymmetric machine. The major advantage of such a model is that it allows changing the physical characteristics to simulate, with a relatively short calculation time, its healthy behavior or in the presence of three-phase asymmetry. The second analytical model is deliberate for inter-turn short circuit fault. It is assumed that the stator circuit phases have two kinds of windings in series, one healthy portion and another short-circuited. This second model is also deliberate for voltage source faults.

Additionally, we validated our study through simulation using Matlab/Simulink and experimentally on the test bench for the case of a healthy and faulty IM. With the help of the results obtained through simulation, we observed that a symmetric IM can be considered a special case of an asymmetric machine; also both of the machines are healthy. Furthermore, an IM with an inter-turn short circuit fault can be analytically considered as an asymmetric IM.

Second, we concentrated on the use of AI in the field of induction machine diagnoses. We developed a primary process that detect and categorize stator inter turn short circuit into the corresponded phase. We validate our proposed diagnostic system using the experimental test bed; an accuracy of 90% has been reached.

In Addition; we have taken in consideration of two kinds of fault, stator short circuit and supply voltage unbalance. The secondary process has the ability to detect and classifies the fault in too SITSC or USV fault and also has the ability to estimate the severity of short circuit turns. We validate our proposed diagnostic process using the same experimental test bed; an accuracy of 95% has been attended.

Third; we propose a Fault Identification (FI) approach employing four types of Artificial neural networks (ANNs) to effectively detect and classify faults, accurately estimating the percentage of each fault type. The FI process consists of three cascaded ANNs. This work was successfully implemented using an experimental test bed, achieving an accuracy percentage ranging from 76% to 100% for all employed ANNs

It seems interesting to continue this work, and various directions are open to us.

- ✓ The hardware implementation of the proposed methods constitutes an important extension that can be made to this work.
- ✓ Validating this approach on a controlled IM (scalar or vector control) is also an important issue.
- ✓ Implementing online identification is another important aspect to consider for effective monitoring and prediction of incoming faults.
- ✓ Combining models in different fault situations, associated with multiple diagnostic approaches process, will constitute a comprehensive solution for the diagnosis of multiple faults in IMs such as SITSC, BRBs, ball bearings, and eccentricity.

APPENDIX (A)

$$r_{11}^{s} = \frac{1}{3}(2r_{as} + \frac{1}{2}r_{bs} + \frac{1}{2}r_{cs})$$

$$r_{12}^{s} = \frac{\sqrt{3}}{6}(r_{cs} - r_{bs})$$

$$r_{13}^{s} = \frac{\sqrt{2}}{6}(2r_{as} - r_{cs} - r_{bs})$$

$$r_{21}^{s} = r_{12}^{s}$$

$$r_{22}^{s} = \frac{1}{2}(r_{bs} + r_{cs})$$

$$r_{23}^{s} = -\sqrt{2}r_{12}^{s}$$

$$r_{31}^{s} = r_{13}^{s}$$

$$r_{32}^{s} = r_{23}^{s}$$

$$r_{33}^{s} = \frac{1}{3}(r_{as} + r_{bs} + r_{cs})$$

$$L_{11}^{ss} = \frac{2}{3}(L_{asas} + 0.25L_{bsbs} + 0.25L_{cscs} - L_{asbs} - L_{ascs} + 0.5L_{bscs})$$

$$L_{12}^{ss} = \frac{\sqrt{3}}{6}(L_{cscs} - L_{bsbs} + 2L_{asbs} - 2L_{ascs})$$

$$L_{13}^{ss} = \frac{\sqrt{2}}{6}(2L_{asas} - L_{bsbs} - L_{cscs} + L_{asbs} + L_{ascs} - 2L_{bscs})$$

$$L_{21}^{ss} = \frac{\sqrt{3}}{6}(-L_{bsbs} + L_{cscs} + 2L_{asbs} - 2L_{ascs})$$

$$L_{22}^{ss} = \frac{1}{2}(L_{bsbs} + L_{cscs} - 2L_{bscs})$$

$$L_{23}^{ss} = \frac{\sqrt{6}}{6}(L_{bsbs} - L_{cscs} + L_{asbs} - L_{ascs})$$

$$L_{31}^{ss} = \frac{\sqrt{2}}{6}(2L_{asas} - L_{bsbs} - L_{cscs} + L_{asbs} + L_{ascs} - 2L_{bscs})$$

$$L_{32}^{ss} = \frac{\sqrt{6}}{6}(L_{bsbs} - L_{cscs} + L_{asbs} - L_{ascs})$$

$$L_{33}^{ss} = \frac{1}{3}(L_{asas} + L_{bsbs} + L_{cscs} + 2L_{asbs} + 2L_{ascs} + 2L_{bscs})$$

$$L_{11}^{sr} = (L_{asr} + 0.25L_{bsr} + 0.25L_{csr})$$

$$L_{12}^{sr} = \frac{-\sqrt{3}}{4}(L_{bsr} - L_{csr})$$

$$L_{21}^{sr} = \frac{-\sqrt{3}}{4}(L_{bsr} - L_{csr})$$

$$L_{22}^{sr} = \frac{3}{4}(L_{bsr} + L_{csr})$$

$$L_{31}^{sr} = \frac{-\sqrt{2}}{4}(-2L_{asr} + L_{bsr} + L_{csr})$$

$$L_{32}^{sr} = \frac{\sqrt{6}}{4}(L_{bsr} - L_{csr})$$

APPENDIX (B)

$$f_{11} = (1 - f_a)^2$$
$$f_{12} = f_a(1 - f_a)$$
$$f_{13} = -\frac{(1 - f_a)(1 - f_b)}{2}$$
$$f_{14} = -\frac{f_b(1 - f_a)}{2}$$
$$f_{15} = -\frac{(1 - f_a)(1 - f_c)}{2}$$
$$f_{16} = -\frac{f_c(1 - f_a)}{2}$$
$$f_{21} = f_a(1 - f_a)$$
$$f_{22} = {f_a}^2$$
$$f_{23} = -\frac{f_a(1 - f_b)}{2}$$
$$f_{24} = -\frac{f_b f_a}{2}$$
$$f_{25} = -\frac{f_a(1 - f_c)}{2}$$
$$f_{26} = -\frac{f_c f_a}{2}$$
$$f_{31} = -\frac{(1 - f_a)(1 - f_b)}{2}$$
$$f_{32} = -\frac{f_a(1 - f_b)}{2}$$
$$f_{33} = (1 - f_b)^2$$
$$f_{34} = f_b(1 - f_b)$$
$$f_{35} = -\frac{(1 - f_b)(1 - f_c)}{2}$$
$$f_{36} = -\frac{f_c(1 - f_b)}{2}$$
$$f_{41} = -\frac{f_b(1 - f_a)}{2}$$
$$f_{42} = -\frac{f_b f_a}{2}$$
$$f_{43} = f_b(1 - f_b)$$
$$f_{44} = {f_b}^2$$
$$f_{45} = -\frac{f_b(1 - f_c)}{2}$$
$$f_{46} = -\frac{f_b f_c}{2}$$
$$f_{51} = -\frac{(1 - f_a)(1 - f_c)}{2}$$

$$L_{11} = -f_a(L_{ls} + \tfrac{2}{3} f_a L_m)$$
$$L_{12} = L_{21} = \frac{1}{3} f_a f_b L_m$$
$$L_{13} = L_{31} = \frac{1}{3} f_a f_c L_m$$
$$L_{14} = f_a\sqrt{\tfrac{2}{3}}(L_{ls} + L_m)$$
$$L_{16} = f_a\sqrt{\frac{2}{3}} L_m$$
$$L_{22} = -f_b(L_{ls} + \tfrac{2}{3} f_b L_m)$$
$$L_{23} = L_{32} = \frac{1}{3} f_b f_c L_m$$
$$L_{24} = -f_b\sqrt{\tfrac{1}{6}}(L_{ls} + L_m)$$
$$L_{25} = f_b\sqrt{\tfrac{1}{2}}(L_{ls} + L_m)$$
$$L_{26} = -f_b\sqrt{\frac{1}{6}} L_m$$
$$L_{27} = f_b\sqrt{\frac{1}{2}} L_m$$
$$L_{33} = -f_c(L_{ls} + \tfrac{2}{3} f_c L_m)$$
$$L_{34} = -f_c\sqrt{\tfrac{1}{6}}(L_{ls} + L_m)$$
$$L_{35} = -f_c\sqrt{\tfrac{1}{2}}(L_{ls} + L_m)$$
$$L_{36} = -f_c\sqrt{\frac{1}{6}} L_m$$
$$L_{37} = -f_c\sqrt{\frac{1}{2}} L_m$$
$$L_{41} = -L_{14}$$
$$L_{42} = -L_{24}$$
$$L_{43} = -L_{34}$$
$$L_{44} = L_{55} = (L_{ls} + L_m)$$
$$L_{46} = L_{57} = L_{64} = L_{75} = L_m$$
$$L_{52} = -L_{25}$$

$$f_{52} = -\frac{f_a(1-f_c)}{2}$$
$$f_{53} = -\frac{(1-f_b)(1-f_c)}{2}$$
$$f_{54} = -\frac{f_b(1-f_c)}{2}$$
$$f_{55} = (1-f_c)^2$$
$$f_{56} = f_c(1-f_c)$$
$$f_{61} = -\frac{f_c(1-f_a)}{2}$$
$$f_{62} = -\frac{f_c f_a}{2}$$
$$f_{63} = -\frac{f_c(1-f_b)}{2}$$
$$f_{64} = -\frac{f_b f_c}{2}$$
$$f_{65} = f_c(1-f_c)$$
$$f_{66} = {f_c}^2$$

$$r_{11} = -(f_a R_s + r_{af})$$
$$r_{14} = f_a\sqrt{\frac{2}{3}}R_s$$
$$r_{22} = -(f_b R_s + r_{bf})$$
$$r_{24} = -f_b\sqrt{\frac{1}{6}}R_s$$
$$r_{25} = f_b\sqrt{\frac{1}{2}}R_s$$
$$r_{33} = -(f_c R_s + r_{cf})$$
$$r_{34} = -f_c\sqrt{\frac{1}{6}}R_s$$
$$r_{35} = f_c\sqrt{\frac{1}{2}}R_s$$

$L_{53} = -L_{35}$
$L_{61} = -L_{16}$
$L_{62} = -L_{26}$
$L_{63} = -L_{36}$
$L_{66} = L_{77} = (L_{lr} + L_m)$
$L_{72} = -L_{27}$
$L_{73} = -L_{37}$
$L_{15} = L_{17} = L_{45} = L_{47} = L_{51} = L_{54} =$
$L_{56} = L_{65} = L_{67} = L_{71} = L_{74} = L_{76} = 0$

$r_{12} = r_{13} = r_{15} = r_{16} = r_{17} = r_{21} =$
$r_{23} = r_{26} = r_{27} = r_{31} = r_{32} = r_{36} =$
$r_{37} = 0$
$r_{41} = -r_{14}$
$r_{42} = -r_{24}$
$r_{43} = -r_{34}$
$r_{44} = r_{55} = R_s$
$r_{52} = -r_{25}$
$r_{53} = -r_{35}$
$r_{66} = r_{77} = R_r$
$r_{45} = r_{46} = r_{47} = r_{51} = r_{54} = r_{56} =$
$r_{57} = r_{61} = r_{62} = r_{63} = r_{64} = r_{65} =$
$r_{67} = r_{71} = r_{72} = r_{73} = r_{74} = r_{75} =$
$r_{76} = 0$

Appendix (C)

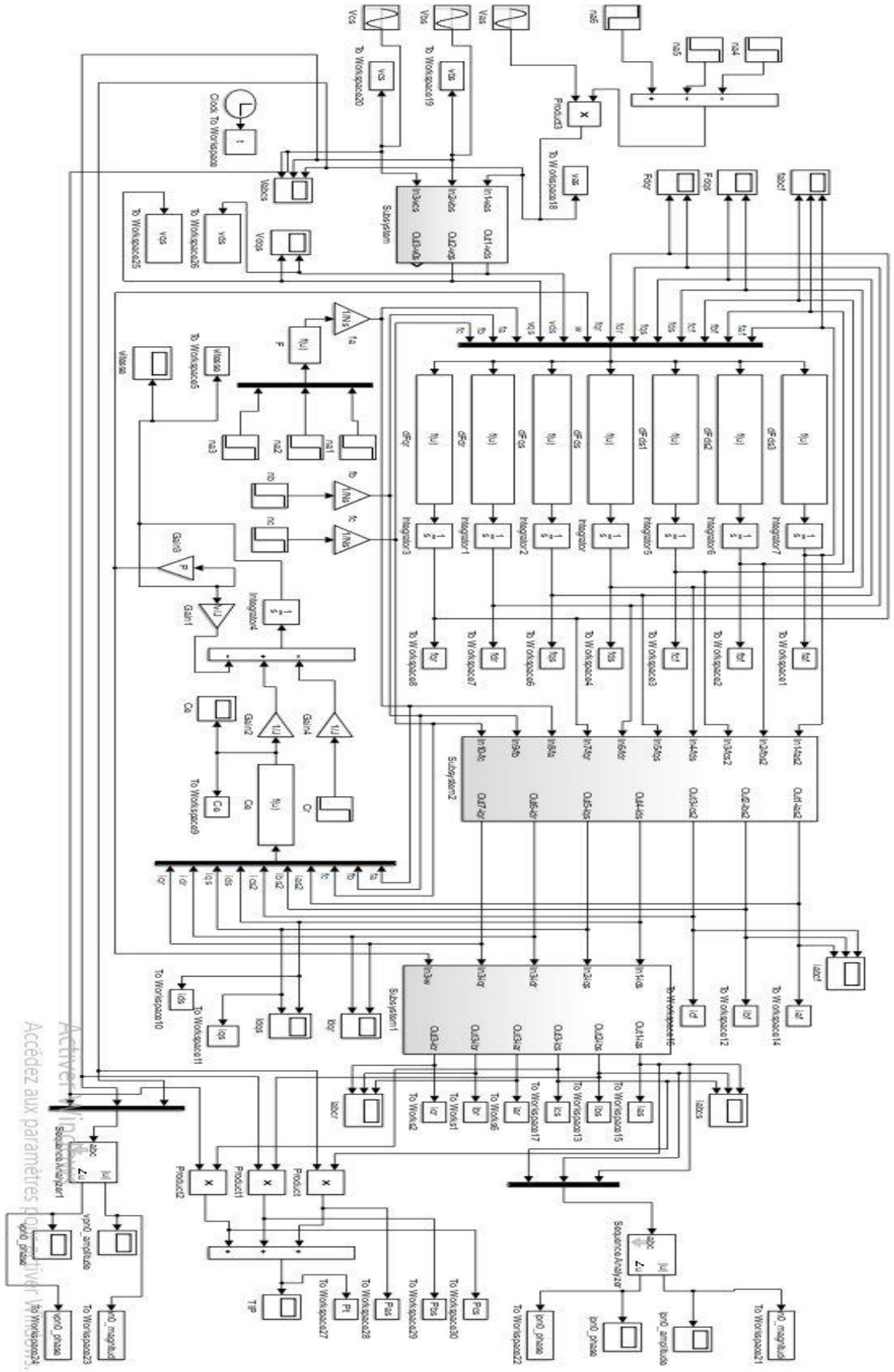

References

1. Philip Langdon Alger. ‘‘Induction Machines: Their Behavior and Uses ’’. Gordon and Breach; 1970. 518 p
2. Ion Boldea and Syed Nasar. “The induction machine handbook”. CRC Press, (2002), 946 p
3. O.V thorsen, M Dalva. “Failure identification and analysis for high-voltage induction motors in the petrochemical industry”. IEEE Transactions on Industry Applications; Volume: 35, Issue: 4, July-Aug (1999).
4. Raul Igmar Gregor Recalde. “Induction Motors: Applications, Control and Fault Diagnostics”. Published by AvE4EvA, 22 November, 2015. 383 p
5. Subrata Karmakar, Surajit Chattopadhyay, Madhuchhanda Mitra and Samarjit Sengupta. “ Induction motor fault diagnosis”. Springer series (4622); November 2015. 182 p.
6. Hamid A Toliyat, Subhasis Nandi, Seungdeog Choi and Homayoun Meshgin-kelk. “Electric Machines modeling, condition monitoring and fault diagnosis”. CRC press Taylor and Francis; (2013); 266 p.
7. R. Puche-Panadero, M. Pineda-Sanchez, M. Riera-Guasp, J. Roger-Folch, E. Hurtado-Perez, and J. Perez-Cruz. “Improved Resolution of the MCSA Method via Hilbert Transform, Enabling the Diagnosis of Rotor Asymmetries at Very Low Slip”. IEEE transactions on Energy Conversion, VOL. 24, NO. 1, MARCH 2009.
8. Jose de Jesus Rangel-Magdaleno, Hayde Peregrina-Barreto, Juan Manuel Ramirez-Cortes, Pilar Gomez-Gil, and Roberto Morales-Caporal. “FPGA-Based Broken Bars Detection on Induction Motors Under Different Load Using Motor Current Signature Analysis and Mathematical Morphology”. IEEE transactions on Instrumentation and Measurement, VOL. 63, NO. 5, May 2014.
9. Yihan Zhaoi, Yu Cheni, Lulu Wangi, Attiq Ur Rehmani, Yonghong Yini, Yonghong Chengi, Toshikatsu Tanaka. “Experiment Research and Analysis of Stator Winding Short Circuit Faults in DFIG”. IEEE 2016 International Conference on Condition Monitoring and Diagnosis - Xi'an – China. 978-1-5090-3396-6 (2016); 4 p.

10. G.G. Acosta_, C.J. Verucchi, E.R. Gelso. “A current monitoring system for diagnosing electrical failures in induction motors”. Mechanical Systems and Signal Processing 20 (2006), 953–965; 13 p.
11. S. M. A. Cruz and A. J. Marques Cardoso. ‘’Stator Winding Fault Diagnosis in Three-phase Synchronous and Asynchronous Motors, by the Extended Park’s Vector Approach ‘’. IEEE conference (2000); 7 p.
12. Tushar G. Vilhekar, Makarand S. Ballal and Hiralal M. Suryawanshi. “Application of Multiple Parks Vector Approach for Detection of Multiple Faults in Induction Motors”. Journal of Power Electronics, Vol. 17, No. 4, pp. 972-982, July 2017.
13. Pu Shi, Zheng Chen,Yuriy Vagapov and Zoubir Zouaoui. “A new diagnosis of broken rotor bar fault extent in three phase squirrel cage induction motor”. Mechanical Systems and Signal Processing 42 (2014); 388–403; 16 p.
14. P.C.M. Lamim Filho , R. Pederiva, J.N. Brito. “Detection of stator winding faults in induction machines using flux and vibration analysis”. Mechanical Systems and Signal Processing 42(2014)377–387; 11 p.
15. B. Liang, B.S. Payne, A.D. Ball and S.D. Iwnicki.“ Simulation and fault detection of three-phase induction motors”. Mathematics and Computers in Simulation 61 (2002) 1–15; 15 p.
16. David G. Dorrell, Andrew M. Knight, Lyndon Evans, and Mircea Popescu. “Analysis and Design Techniques Applied to HybridVehicle Drive Machines—Assessment of Alternative IPM and Induction Motor Topologies”. IEEE transactions on Industrial Electronics, VOL. 59, NO. 10, October 2012.
17. Giovanni Betta, Consolatina Liguori, Alfredo Paolillo, and Antonio Pietrosanto. “A DSP-Based FFT-Analyzer for the Fault Diagnosis of Rotating Machine Based on Vibration Analysis”. IEEE transactions on Instrumentation and Measurement, VOL. 51, NO. 6, December 2002; 7 p.
18. Jafar Zarei, Mohammad Amin Tajeddini, Hamid Reza Karimi. “Vibration analysis for bearing fault detection and classification using an intelligent filter”. Mechatronics 24 (2014) 151–157 ; 7 p.
19. Manés F. Cabanas, Francisco Pedrayes, Manuel G. Melero, Carlos H. Rojas García, José M. Cano, Gonzalo Alonso Orcajo, and Joaquín González Norniella. “Unambiguous Detection of Broken Bars in Asynchronous Motors by Means of a Flux Measurement-Based Procedure”. IEEE transactions on Instrumentation and Measurement, VOL. 60, NO. 3, March 2011; 9 p.

20. Humberto Henao, Cristian Demian, and Gérard-André Capolino. “A Frequency-Domain Detection of Stator Winding Faults in Induction Machines Using an External Flux Sensor”. IEEE transactions on Industry Applications, VOL. 39, NO. 5, September/October 2003; 8 p.
21. Mario Eltabach, Jerome Antoni, Micheline Najjar. “Quantitative analysis of noninvasive diagnostic procedures for induction motor drives”. Elsevier, Mechanical Systems and Signal Processing 21 (2007) 2838–2856.
22. Zhenxing Liu, Xianggen Yin, Zhe Zhang, Deshu Chen and Wei Chen. *“*Online Rotor Mixed Fault Diagnosis Way Based on Spectrum Analysis of Instantaneous Power in Squirrel Cage Induction Motors*”.* IEEE transactions on Energy Conversion, VOL. 19, NO. 3, September 2004; 6 p.
23. Arvind Singh, Bevon Grant, Ronald DeFour, Chandrabhan Sharma and Sanjay Bahadoorsingh. “A review of induction motor fault modeling”. Electric Power Systems Research 133 (2016) 191–197; 7 p.
24. Khelif Samia. “Modélisation Des Machines Asynchrones en Vue du Diagnostic Prise en Compte Adéquate du Circuit Magnétique”. Magister thesis 2012 ; 77 p.
25. B. Vaseghi, N. Takorabet, and F. Meibody-Tabar. “Transient Finite Element Analysis of induction machines with stator winding turn fault”. Progress In Electromagnetics Research, PIER 95, 1-18 p; 2009.
26. C. Delforge, B. Lemaire-Semail. “Induction machine modeling using finite element and permeance network methods”. IEEE transactions on Magnetics, VOL. 31, NO. 3, May 1995; 4 p.
27. M. Arkan, D. Kostic-Perovic and P. J. Unsworth, 'Modelling and simulation of induction motors with inter-turn faults for diagnostics', Electric Power Systems Research 75 (2005) 57–66.
28. G. Habetler, Rangarajan M. Tallam, 'Transient Model for Induction Machines With Stator Winding Turn Faults', page 632 - 637, IEEE Transaction on industry application, Vol.38, No.3, MAY/June, 2002.
29. LAZAR Amat Ellah Noussaiba, SAID Watik, LAMRI Chahinez, ELMERRAOUI Khadidja and FERDJOUNI Abdelaziz. “Modeling and Simulation of Induction Motor With Inter-turn short circuit Faults For Stator Detection and Isolation”. International Conference on Electrical, Computer, Communications and Mechatronics Engineering (ICECCME) 7-8 October 2021, Mauritius; 978-1-6654-1262-9/21/; 6 p.

30. A. J. Marques Cardoso and E. S. Saraiva. “Computer-Aided Detection of Airgap Eccentricity in Operating Three-phase Induction Motors by Park’s Vector Approach”. IEEE transactions on industry applications, Vol. 29, No. 5, September/ October 1993; 5 p.
31. Jian-Da Wua, Chin-Wei Huanga and Rongwen Huang. “An application of a recursive Kalman filtering algorithm in rotating machinery fault diagnosis” NDT&E International 37 (2004) 411–419; 9 p.
32. Khadidja El Merraoui, Abdellaziz Ferdjouni and M’hamed Bounekhla. “Real time observer-based stator fault diagnosis for IM”. International Journal of Electrical and Computer Engineering (IJECE) Vol. 10, No. 1, February 2020, pp. 210~222; 13 p.
33. Ruonan Liu, Boyuan Yang, Enrico Zio and Xuefeng Chen. “Artificial intelligence for fault diagnosis of rotating machinery: A review”. Mechanical Systems and Signal Processing 108 (2018) 33–47; 15 p.
34. Giuseppe Bonaccorso. “Machine learning algorithms”. Published by Pack-t Publishing Ltd. July 2017; 352 p.
35. Uk Jung · Bong-Hwan Koh. “Wavelet energy-based visualization and classification of high-dimensional signal for bearing fault detection”. Springer-Verlag London ; 13 June 2014, 19 p.
36. D.H. Pandya, S.H. Upadhyay, S.P. Harsha. “Fault diagnosis of rolling element bearing with intrinsic mode function of acoustic emission data using APF-KNN”. Expert Systems with Applications 40 (2013) 4137–4145 ; 9 p.
37. Jeevanand Seshadrinath, Bhim Singh, and B K Panigrahi. “Vibration Analysis Based Inter-turn Fault Diagnosis in Induction Machines “. IEEE 2013; 11 p.
38. Lixiang Duan, Mingchao Yao, Jinjiang Wang, Tangbo Bai and Laibin Zhang. “Segmented infrared image analysis for rotating machinery fault Diagnosis”. Infrared Physics & Technology 77 (2016) 267–276; 10 p.
39. Abdenour Soualhi, Kamal Medjaher, and Noureddine Zerhouni. “Bearing Health Monitoring Based on Hilbert–Huang Transform, Support Vector Machine, and Regression”. IEEE transactions on Instrumentation and Measurement june 2014; 11 p.
40. Xuejun Li, Ke Wang and Lingli Jiang. “The Application of AE Signal in Early Cracked Rotor Fault Diagnosis with PWVD and SVM”. Journal of Software, Vol. 6, No. 10, October 2011; 8 p.

41. Tribeni Prasad Banerjee a, Swagatam Das. “Multi-sensor data fusion using support vector machine for motor fault detection”. Information Sciences 217 (2012) 96–107; 12 p.
42. M. Saimurugan, K. Ramachandran, V. Sugumaran, N. Sakthivel, Multi component fault diagnosis of rotational mechanical system based on decision tree and support vector machine, Expert Syst. Appl. 38 (4) (2011) 3819–3826.
43. Ilhan Aydin, Mehmet Karakose and Erhan Akin .“An approach for automated fault diagnosis based on a fuzzy decision tree and boundary analysis of a reconstructed phase space”. ISA Transactions 53 (2014) 220–229; 10 p.
44. Abdelkader LAKROUT, Mokhtar BENDJEBBAR, Noureddine HENINI. “Electric Stator Faults Detection in Induction Motor based on Fuzzy Logic Technique”. 2018 International Conference on Applied Smart Systems (ICASS'2018) 24-25 November 2018, Médéa, ALGERIA.
45. Negin Lashkari, Hamid Fekri Azgomi, Javad Poshtan. “Asynchronous Motors Fault Detection Using ANN and Fuzzy Logic Methods”. IEEE Transactions on Industrial Electronics (2016), vol. 5.
46. Shai Shalev-Shwartz, Shai Ben-David. “Understanding Machine Learning”. Cambridge University Press (2014); 416 p.
47. Kara Mostfa Khelil Chrefa. “Diagnosis of photovoltaic systems”. Doctoral thesis, university of Blida1 (july 2021); 168 p.
48. AEN. Lazar, A.Bendali, A. Ferdjouni. “ANN-approach for ITSC Fault Diagnosis of Induction Motor”. 2021 IEEE Workshop on Electrical Machines Design, Control and Diagnosis (WEMDCD) February 2021; 6 p.
49. Negin Lashkari, Javad Poshtan, Hamid Fekri Azgomi. “Simulative and experimental investigation on stator winding turn and unbalanced supply voltage fault diagnosis in induction motors using Artificial Neural Networks”. ISA Transactions 59 (2015); p: 334–342.
50. Luqman Maraab, Zakariya Al-Hamouz, Mohammad Abido. “An Efficient Stator Inter-Turn Fault Diagnosis Tool for Induction Motors”. Energies (2018), 11, 653 p: 3–18.
51. Lazar Amat Ellah Noussaiba and Ferdjouni Abdelaziz. “ANN-based fault diagnosis of induction motor under stator inter-turn short circuits and unbalanced supply voltage “. *ISA Transactions (2023) 1–14.*

52. S.S. Moosavi, A. Djerdir, Y. Ait-Amirat, D.A. Khaburi. “ANN based fault diagnosis of permanent magnet synchronous motorunder stator winding shorted turn”. Elsevier, Electric Power Systems Research 125 (2015) 67–82.
53. Yaw D. Nyanteh, Sanjeev K. Srivastava, Chris S. Edrington, David A. Cartes. “ Application of artificial intelligence to stator winding fault diagnosis in Permanent Magnet Synchronous Machines “ . Electric Power Systems Research 103 (2013) 201– 213; 13 p.
54. D.A. Asfani, A.K. Muhammad, Syafaruddin, M.H. Purnomo, T. Hiyama. Temporary short circuit detection in induction motor winding using combination of wavelet transform and neural network. Elsevier, Expert Systems with Applications 39 (2012) 5367–5375; 9 p.
55. Nabanita Dutta, Palanisamy Kaliannan, Paramasivam Shanmugam. Application of machine learning for inter turn fault detection in pumping system. Nature portfolio, Scientific Reports | (2022).
56. Gayatridevi Rajamany , Sekar Srinivasan, Krishnan Rajamany, and Ramesh K. Natarajan. “ Induction Motor Stator Interturn Short Circuit Fault Detection in Accordance with Line Current Sequence Components Using Artificial Neural Network”. Hindawi, Journal of Electrical and Computer Engineering. Volume 2019, Article ID 4825787, 11 p.
57. Li Deng and Dong Yu. “Deep Learning Methods and Applications”. Foundations and Trends in Signal Processing (2014); 198 p.
58. Rui Zhao, Ruqiang Yan, Zhenghua Chen, Kezhi Mao, Peng Wang and Robert X. Gao. “Deep learning and its applications to machine health Monitoring”. Mechanical Systems and Signal Processing 115 (2019) 213–237; 25 p.
59. Olivier Janssens, Viktor Slavkovikj, Bram Vervisch, Kurt Stockman. “Convolutional Neural Network Based Fault Detection for Rotating Machinery”. Journal of Sound and Vibration; March 2016, 15 p.
60. Ruonan Liu, Guotao Meng, Boyuan Yang, Chuang Sun and Xuefeng Chen. “Dislocated Time Series Convolutional Neural Architecture: An Intelligent Fault Diagnosis Approach for Electric Machine”. 2009 IEEE conference; 11 p.
61. Rui Zhao, Dongzhe Wang, Ruqiang Yan, Kezhi Mao, Fei Shen, and Jinjiang Wang. “Machine Health Monitoring Using Local Feature-based Gated Recurrent Unit Networks”. IEEE Transactions on Industrial Electronics ; IEEE(2017), 11 p.

62. P. Malhotra, A. Ramakrishnan, G. Anand, L. Vig, P. Agarwal, G. Shroff, “Multi-sensor prognostics using an unsupervised health index based on LSTM Encoder-Decoder”. arXiv preprint arXiv:1608.06154.
63. Menshawy Mohamed, Essam Mohamed, Al-Attar Mohamed, Mohamed Moustafa Hassan. “Detection of Inter Turn Short Circuit Faults in Induction Motor using Artificial Neural Network”. Proceeding of the 26th conference of Fruct Association, IEEE (June 2020).